Photoinduced and Thermal Reactions of Functional Molecules at Surfaces

Im
Fachbereich Physik
der
Freien Universität Berlin
eingereichte

Dissertation

zur Erlangung des Grades eines
Doktors der Naturwissenschaften

vorgelegt von

Christopher Bronner

Berlin 2014

This work has been conducted in the group of Prof. Dr. Petra Tegeder between September 2010 and June 2013 at the Department of Physics of the Freie Universität Berlin and between July 2013 and March 2014 at the Institute of Physical Chemistry of the Ruprecht-Karls-Universität Heidelberg.

Erstgutachterin: Prof. Dr. Petra Tegeder
Ruprecht-Karls-Universität Heidelberg

Zweitgutachterin: Prof. Dr. Katharina J. Franke
Freie Universität Berlin

Drittgutachter: Prof. Dr. Wilfried Wurth
Universität Hamburg

Datum der Disputation: 20. Juni 2014

eMail: bronner@zedat.fu-berlin.de

Eidesstattliche Versicherung

Hiermit versichere ich, daß ich alle verwendeten Hilfsmittel und Hilfen angegeben und die vorliegende Arbeit auf dieser Grundlage selbstständig verfasst habe. Diese Arbeit ist nicht schon einmal in einem früheren Promotionsverfahren eingereicht worden.

Heidelberg, im März 2014
Christopher Bronner

Abstract

In order to introduce a band gap into graphene structures, charge carriers can be laterally confined in quasi-one-dimensional graphene nanoribbons (GNR) with nanometer scale widths. These GNR can be produced in an atomically precise fashion and with well-defined electronic structure by thermally induced on-surface synthesis from halogen-substituted molecular precursors. In this thesis, photoemission techniques are used to characterize the electronic structure of the different phases of such a bottom-up synthesis reaction: the Br-substituted monomers after adsorption on a Au(111) surface, an intermediate polymer and finally the fully conjugated GNR. Fundamental differences, especially concerning the band gap, are observed which are attributed to the different nature of the respective electronic systems. Using temperature-programmed desorption, the reaction pathway of the Br atoms after dehalogenation is followed, namely associative desorption of HBr during the cyclodehydrogenation reaction in the last step of the on-surface synthesis. As an alternative to the established, thermally induced fabrication method, photo-induced covalent coupling of the molecular precursors on the surface is investigated and dimerization is observed. The underlying process is found to be an electronic excitation within the substrate followed by charge transfer into the adsorbate, creating an anionic resonance. Additionally we find that N-doping of molecular precursors allows to align the band gap with respect to the Fermi level of the substrate without altering the size of the band gap.

Following a different approach for the development of functional nanostructures, a photochromic molecule, di-meta-cyano-azobenzene, is studied with photoelectron spectroscopies on the semi-metallic Bi(111) surface. Azobenzenes in solution undergo reversible, photo-induced *trans–cis* isomerization reactions and in this work, photoisomerization of the azobenzene derivative is observed also for molecules directly adsorbed on the surface. However, the process is not initiated by an intramolecular electronic excitation as in the free molecule but rather by photon absorption in the substrate followed by charge transfer into the unoccupied electronic states of the adsorbate and formation of an anionic resonance which leads to the conformational change. Photoisomerization can furthermore be initiated in the multilayer where the efficiency of the process depends on the molecular environment. In both coverage regimes, the *cis* isomers perform a thermally induced reaction which is interpreted as a phenyl ring rotation.

Kurzzusammenfassung in deutscher Sprache

Um eine Bandlücke in Graphenstrukturen einzubringen, können Ladungsträger in quasi-eindimensionalen Graphen-Nanobändern (engl. graphene nanoribbons, GNR) mit Breiten im Nanometer-Bereich lateral eingeschränkt werden. Durch thermisch induzierte, oberflächenassistierte Synthese ausgehend von halogensubstituierten molekularen Vorläufermolekülen können diese GNR auf atomar präzise Weise und mit wohldefinierter elektronischer Struktur hergestellt werden. In dieser Arbeit werden Photoemissionsmethoden verwendet, um die elektronische Struktur der verschiedenen Phasen einer solchen, aufbauenden Synthesereaktion zu charakterisieren: die Br-substituierten Monomere nach der Adsorption auf der Au(111)-Oberfläche, das intermediäre Polymer und letztlich das voll konjugierte GNR. Fundamentale Unterschiede, vor allem in Bezug auf die Bandlücke, werden beobachtet und dem unterschiedlichen Wesen der jeweiligen elektronischen Systeme zugeschrieben. Mittels Thermodesorptionsspektroskopie wird der Reaktionspfad der Br-Atome nach der Dehalogenierung verfolgt, nämlich eine assoziative Desorption von HBr während der Zyklodehydrogenierungsreaktion im letzten Schritt der oberflächengebundenen Synthese. Als Alternative zur etablierten, thermischen induzierten Herstellungsmethode wird eine lichtinduzierte kovalente Kopplung der Vorläufermoleküle untersucht und eine Dimerisierung beobachtet. Der zugrunde liegende Prozess wird als elektronische Anregung im Substrat erkannt, gefolgt von Ladungstransfer ins Adsorbat, der eine anionische Resonanz erzeugt. Desweiteren lernen wir, dass N-Dotierung der molekularen Vorläufer eine Ausrichtung der Bandlücke relativ zum Ferminiveau des Substrats erlaubt, ohne die Größe der Bandlücke zu ändern.

Einem anderen Ansatz für die Entwicklung funktionaler Nanostrukturen nachgehend wird ein photochromes Molekül, di-meta-cyano-Azobenzol, mittels Photoelektronenspektroskopien auf der halbmetallischen Bi(111)-Oberfläche untersucht. Azobenzol unterzieht sich in Lösung einer reversiblen, lichtinduzierten *trans–cis*-Isomerisierungsreaktion und in dieser Arbeit wird die Photoisomerisierung des Azobenzolderivats auch für direkt an der Oberfläche adsorbierte Moleküle beobachtet. Allerdings wird dieser Prozess nicht, wie im freien Molekül, durch intramolekulare elektronische Anregung ausgelöst, sondern vielmehr durch Photonenabsorption im Substrat gefolgt von Ladungstransfer in die unbesetzten elektronischen Zustände des Adsorbats und die Bildung einer anionischen Resonanz, die zur Konformationsänderung führt. Photoisomerisierung kann außerdem in der Multilage ausgelöst werden, wo die Effizienz des Prozesses von der molekularen Umgebung abhängt. In beiden Bedeckungsordnungen vollführt das *cis*-Isomer eine thermisch ausgelöste Reaktion, die als Phenylringrotation interpretiert wird.

Contents

List of Figures

Chapter 1

Introduction

Advances in nanotechnological materials research can generally be divided into two categories: on the one hand, there is the challenge of improving existing concepts and devices to meet more and more ambitious performance requirements. For example, miniaturization of field-effect transistors (FETs) [1, 2, 3, 4, 5, 6], radio-frequency transmitters [7, 8, 9], conducting paths [10, 11, 12, 13] and data storage devices [14, 15, 16, 17, 18] requires addressing fundamental physical limitations, as devices reach the nanoscale which is governed by the principles of quantum mechanics. Additionally, the reduced size leads to increased heat development and energy consumption. On the other hand, the same physical principles of the nanoscale can also provide opportunities for entirely new devices and concepts such as transparent electrodes [19], multiple exciton generation for photovoltaics [20, 21, 22], molecular machines and switches [23, 24, 25, 26, 27, 28], functional surfaces [29, 30, 31, 32] or molecular self-assembly [33, 34, 35].

Several different classes of materials are in the focus of current research in order to pursue the further development of nanotechnological devices. While graphene and other low-dimensional carbon materials have been particularly prominent in recent years, the idea of machines and electronic devices based on single functional molecules is equally intriguing. Additionally, there are many other fascinating materials, e.g. topological insulators [36, 37], the properties of which promise to foster the development of spintronic devices [38, 39]. The present thesis follows two of the above pathways, namely low-dimensional carbon materials on the one hand and single functional molecular units, namely molecular switches, on the other hand.

Since its experimental realization in 2004, graphene has been subject to many studies both in fundamental and applied research due to its unique structural and electronic properties [40, 41, 42, 43]. Besides its remarkably low, atomic thickness, electrons close to the Fermi level in graphene behave like a two-dimensional gas of massless Dirac fermions. By virtue of this property, graphene offers possibilities to study quantum electrodynamics with a table-top experiment and at the same time promises a manifold of possible applications due to its extraordinarily high charge carrier mobility. However, an infinitely extended graphene sheet ("bulk graphene") is a semi-metal with a vanishing band gap, which is a major drawback, e.g. for the use in graphene transistors which have been built but possess only insufficient on–off ratios [4, 5].

Nevertheless, by modifying the structure of graphene, a band gap of technologically relevant size can be introduced, at the cost of charge carrier mobility, by applying mechanical strain along the sheet [44, 45, 46], using a bilayer of graphene [47, 48, 6] or by charge carrier confinement in quasi-one-dimensional graphene nanoribbons (GNR). The latter concept has the additional advantage that it inherently addresses the need for lateral size constrictions of a graphene structure in a nanotechnological device.

Unlike carbon nanotubes (CNT), GNR are flat graphene structures with widths on the nanometer scale but, similar to CNT, the electronic structure of GNR is highly dependent on their geometry and chemical composition: the one-dimensional band structure of a GNR depends critically on its chirality (armchair, zigzag or intermediate edge shapes) [49, 50] and the size of the band gap depends inversely on the GNR width [51, 52, 53, 54, 55, 56, 57]. Along edges with zigzag character, a spin-polarized edge state is found which can be thought of as a one-dimensional surface state of the two-dimensional ribbon [58, 59, 60, 61, 62, 63]. By doping GNR, e.g. with N or B atoms, a shifting of the band structure with respect to the chemical potential of the environment can be observed [64, 65, 66], similar to bulk graphene [67, 68]. However, in past experimental studies, precise control over dopant concentration and location has been challenging, which is unfortunate because the effect of doping is significantly influenced by these parameters. Variation of GNR width, chirality and doping thus provide complementary approaches for tailoring their electronic structure. GNR FETs have already been made and show significantly higher on–off ratios compared with devices using bulk graphene [69, 56].

Despite these intriguing electronic properties, synthesis of structurally precise GNR remains challenging using lithography [70, 53], longitudinal unzipping of CNTs [71, 72, 73] or other top-down concepts [56]. While some top-down procedures allow design of arbitrary graphene nanostructures and devices on a length scale of tens of nanometers, they lack the necessary atomic precision on the sub-nanometer scale which is necessary to guarantee well-defined edge shapes, sufficiently low defect concentrations or GNR widths of a few nanometers. However, a high degree of geometrical precision is very important in order to employ GNR, e.g. in transistor devices, because of the critical dependence of the electronic properties of the GNR on their geometrical shape. Due to these shortcomings we will follow a fundamentally different bottom-up approach to GNR synthesis in this thesis, namely self-assembly of surface-bound molecular precursors [74, 34]. Specifically, the precursors are halogen-substituted and the halogen (in our case Br) can be thermally dissociated leading to radical species which subsequently couple covalently [35, 12, 75, 76]. This concept has been successfully applied for GNR fabrication on noble metal surfaces [77, 78].

The objective of the present thesis, with regard to GNR, is to investigate the electronic properties of the different stages of the thermally-induced on-surface synthesis reaction, i.e. the adsorbed precursor molecules, an intermediate, not fully conjugated polymer and finally the GNR. To that end we use two-photon photoemission (2PPE), which allows spectroscopy of occupied as well as unoccupied electronic states. We observe the formation of a one-dimensional band structure both for the intermediate polymer and the GNR. However, the electronic system of the fully aromatic GNR is fundamentally different from the polymer and as a consequence, the band gap is only half as large and the end of the finite GNR exhibit peculiar, localized electronic states. Furthermore we use temperature-programmed desorption to study the thermal synthesis reaction in detail, particularly the reaction pathway of the Br substituents after dissociation which desorb associatively as HBr during the final step of the reaction. Furthermore, in order to explore a possible photo-induced pathway for GNR synthesis, we investigate the effect of UV light and observe an on-surface covalent coupling reaction of the molecular precursors which is initiated by an electronic excitation in the substrate followed by charge transfer into unoccupied electronic states of the adsorbate. Additionally, the effect of nitrogen doping is studied by precursor substitution which results in n-doping of the GNR. While the size of the band gap remains unaffected, the alignment of the electronic structure of the GNR with respect to the Fermi level of the underlying substrate can be altered by the doping.

As outlined above, graphene structures, which we have discussed above, are only one approach to the development of novel nanomaterials. In contrast, other strategies are e.g. single molecules equipped with functional groups or complex supramolecular structures consisting of different molecular building blocks. In the research on such molecular materials, focus currently lies on prototypical systems which comprise distinct functions. One prominent example are molecular switches, molecules with two or more (meta-)stable states, all of which typically have different conformations. The different molecular states have distinct physical or chemical properties that allow to determine the state of the molecule and furthermore typically constitute the technological interest in the specific compound, e.g. conductivity, hydrophobicity, dipole moment or color (i.e. fluorescence wavelength). Additionally, interconversion channels exist between the molecular states which allow external manipulation and arbitrary changes of the above characteristics [79, 23, 24, 25].

There is a large variety of changes which molecular switches can undergo and by which they are categorized: the most studied are conformational switches which e.g. perform *trans*–*cis* isomerization reactions, like azobenzene [80, 81], or ring-opening/-closing reactions, like spiropyran [82, 83, 84]; diarylethenes mainly change their electronic structure and thereby also their conductivity [85, 86], and metal-phthalocyanines [87, 88] as well as metal-porphyrins [89, 90] can be converted between different spin states. The external stimuli can be equally diverse: light of different wavelengths [80, 82], heat [91, 92], electric fields [93], inelastically tunneling electrons [94, 95], or exposure to particular chemical environments [90] can be used for manipulation.

Motivation for the work with molecular switches arises both from technological interests as well as questions of fundamental research. Switching units have been used to give function to more complex molecules into which they have been incorporated [96, 27], they are thought of as elements of nanoelectric switches in molecular circuity [97, 98, 99] and have been used as a key unit in self-assembled monolayers (SAMs) which constitute functional surfaces [30, 32]. For example, surfaces functionalized with SAMs have been used to induce lateral motion of adsorbed macroscopic droplets [29] or to modulate the adhesion of biological cells [31]. Furthermore, the bistability of certain molecular switches makes them attractive for optical data storage applications [14, 17, 18, 100] and the changing molecular conformation upon external stimuli is interesting for sensor applications. The latter is also motivated by the human perception of light, which is triggered by a *cis*–*trans* isomerization of a chromophore in rhodopsin [101, 102, 103]. Molecular switches are also of considerable interest for the development of dispersion corrections to density functional theory which take into account van der Waals interactions [104, 105, 106].

Since external manipulation with light is the most suitable stimulus in many situations, the majority of the most-studied systems are photochromic molecular switches. Among them, azobenzene is a particularly prominent example and at the same time constitutes one of the most simple molecular switches. Azobenzene can be interconverted between the energetically favored *trans* isomer and the metastable *cis* form by light absorption. Following the corresponding intramolecular electronic excitation, azobenzene relaxes on the potential energy surface (PES) of an excited molecular state, transcending the energetic barrier between the two isomers in the electronic ground state. This barrier can also be overcome thermally in a *cis*–*trans* back-reaction along the PES of the ground state [80, 107, 81, 108, 109].

In most scenarios for a technical implementation of molecular switches, they will be required to maintain their functionality in a condensed state, i.e. in a three-dimensional matrix or confined to two-dimensional surfaces or interfaces. Molecular switches adsorbed directly on (especially metal) surfaces are often found to lose the functionality they possess in solution [110, 111, 112, 113, 114, 115]. In a few cases, the switching ability is conserved in the adsorbed state but the excitation mechanism that induces the conformational change usually differs from the one in the free molecule [116, 117, 118, 119]. Whether or not adsorption leads to a quenching of the molecular functionality depends on different aspects of the molecule–substrate interaction, i.e. steric hindrance due to the presence of the substrate, electronic coupling of the molecular orbitals and the substrate bands which may result in efficient de-excitation channels and thus reduced lifetimes of excited molecular states or a modified potential energy surface which can lead to a loss of bistability [120]. In higher adsorbate layers, i.e. in the multilayer regime, conservation of the switching ability is much more common due to the increased decoupling from the substrate [113, 121, 122, 123] and photoisomerization has even been observed in bulk materials [124, 125].

In order to conserve the switching properties at surfaces or to increase the efficiency of the processes, different approaches have been developed to decouple molecular switches from the substrate, namely separating the photochromic unit from the surface by long linker groups in self-assembled monolayers [126, 127, 128, 129], using thin isolating layers [130, 131, 132] or bulky side-groups attached to the functional molecules [133, 134, 135, 136, 137]. An alternative strategy to achieve functional adsorbed molecular switches with high efficiency is to explicitly take the adsorbate–substrate interaction into account which naturally requires substantial insight into the electronic and geometrical aspects of this interaction. However, since the substrate can offer excitation channels unavailable to the isolated molecule [138, 139, 140], these interactions can be beneficial. We will pursue this strategy in the present thesis by choosing a semi-metallic substrate and a specific azobenzene derivative, di-meta-cyano-azobenzene (DMC), the properties of which, respectively, interact to foster photoisomerization.

In the present thesis, we are interested in the photoisomerization ability of DMC on the Bi(111) surface. We use photoemission techniques to characterize photo-induced changes of DMC in the first and higher layers which are identified as photoisomerization reactions. Using direct photoemission and 2PPE, the electronic structure of the adsorbate–substrate system is studied and we find that the photoisomerization reactions in both coverage regimes are initiated by electronic excitations in the substrate bands and subsequent creation of an anionic resonance of DMC. In light of the reversibility of the isomerization reaction of azobenzene in solution, we then attempted to use light and thermal activation to bring the system back into its *trans*-state. While the *cis*-isomers prove too stable to perform such a back-reaction, we observe a different, thermally induced reaction which we ascribe to the rotation of a phenyl ring in the *cis*-isomer around a σ-bond.

The two concepts followed in the framework of this thesis, photoisomerization of adsorbed molecular switches as well as surface-bound covalent assembly of GNR are based on the external manipulation of π-conjugated organic molecules adsorbed directly on (semi-)metal surfaces. The corresponding adsorbate–substrate bond is governed by van der Waals interaction, i.e. physisorption, in both cases and the molecular arrangement is determined by (covalent or non-covalent) self-assembly in a bottom-up fashion. Both concepts also share common problems with regard to application in nanotechnological devices: unlike the semiconducting substrates typically found in current devices, we use metallic and semi-metallic substrates which would of course lead to short-circuits. On the mesoscopic scale, the self-assembly of the adsorbate molecules occurs uniformly on the entire surface and there are no means of writing arbitrary structures, as in lithography, which would however be desirable for the development of devices. The organic molecules are furthermore not as thermally stable as bulk semiconductor materials and more sensitive to photodegradation, particularly induced by UV light.

The layout of this thesis is as follows. We will introduce the main experimental technique, two-photon photoemission, along with the details of the used setup as well as sample preparation and characterization in chapter 2. Chapter 3 will first give an introduction to the electronic structure of GNR in general followed by an overview over previously conducted studies on the systems investigated here. In section 3.2, we will discuss a bottom-up fabricated armchair GNR (AGNR) with respect to (i) the structure of the corresponding monomers, (ii) its thermally induced two-step synthesis which we follow using temperature-programmed desorption (TPD), (iii) the electronic structure of the intermediate polyanthrylene in comparison to (iv) the final reaction product, the AGNR, and finally (v) a photo-induced reaction as an alternative pathway for covalent coupling of the molecular precursors. Section 3.3 will cover another, chevron-shaped bottom-up synthesized GNR (CGNR) and the effects of precursor nitrogen doping on (i) its band gap alignment with respect to the Fermi level and (ii) its image potential state (IPS). Chapter 4 will first give a short introduction to the isomerization of azobenzene, an overview over previous work on the azobenzene derivative used in the present thesis and the excitation mechanisms at substrate–adsorbate interfaces. Section 4.1 will cover photoisomerization reactions in (i) the first monolayer and (ii) higher layers, followed by (iii) the discussion of a thermally induced reaction of the *cis* isomers.

Chapter 2

Experimental Methods and Setup

2.1 Two-Photon Photoemission (2PPE)

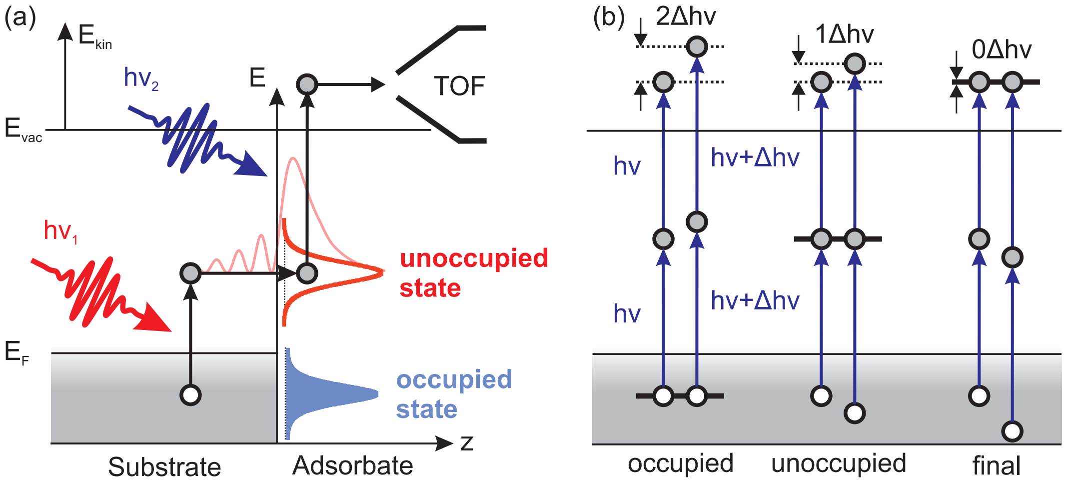

Figure 2.1: (a) Schematic depiction of 2C-2PPE from an adsorbate-covered metal. The pump pulse ($h\nu_1$) excites an electron to an unoccupied intermediate state. The probe pulse ($h\nu_2$) photoemits the electron which is detected in a time-of-flight spectrometer. Adapted from ref. [141]. (b) Assignment of 1C-2PPE spectral features to occupied, unoccupied or final electronic states by variation of the photon energy $h\nu$.

In order to study surface-bound molecules with respect to their electronic structure, we mainly employ two-photon photoemission (2PPE) which is a pump-probe technique able to probe the occupied and unoccupied electronic states of the adsorbate–substrate system. 2PPE has proven to be a valuable technique for the investigation of the electronic structure of surfaces and adsorbates [142, 143, 144, 145, 146]. Like conventional photoemission it is a surface-sensitive method due to the low mean free path of electrons at the respective energies. In 2PPE, electrons are photo-emitted from the sample in a two-step process by two laser pulses with equal (one-color 2PPE, 1C-2PPE) or different (two-color 2PPE, 2C-2PPE) photon energies $h\nu_1$ and $h\nu_2$. The photon energies are smaller than the work function Φ in order to avoid direct photoemission processes. A photon of the first pulse, the pump pulse, excites an electron from an occupied electronic state below the Fermi energy E_F to an unoccupied intermediate state which lies below the vacuum level $E_\mathrm{Vac} = E_\mathrm{F} + \Phi$ of the sample (see Fig. 2.1a). Both the occupied, initial state and the unoccupied, intermediate state may arise from electronic states of the substrate (e.g. bands, surface states and resonances), molecule-induced electronic states (e.g. molecular orbitals, possibly hybridized with substrate states) or electronic states associated with an interface (e.g. image potential states). The second pulse, the probe pulse, excites the electron above the vacuum level of the sample into a final state with energy E_Final which propagates toward the detector, in this case a time-of-flight (TOF) spectrometer (see sect. 2.2). Note, that this two-step process is generally one quantum mechanical excitation process, rather than two time-separated excitations (unless the pulses are delayed with respect to each other, see below). Consequently, it can also occur via a virtual intermediate state, i.e. even when there is a vanishing density of states (DOS) at the intermediate energetic position.

Due to the different origins that a peak in a 2PPE spectrum might have, the spectra are usually displayed versus the final state energy, referenced to the Fermi level, which is essentially the kinetic energy E_kin added to the work function of the sample, $E_\mathrm{Final} - E_\mathrm{F} = E_\mathrm{kin} + \Phi$. One advantage of this energy axis is that the work function can be read from the spectra's low energy cut-off (the secondary edge). Furthermore, the binding energies of the corresponding occupied (unoccupied) electronic states can be obtained by subtraction of both photon energies (the probe photon energy). Variation of the photon energies allows an assignment of a spectral feature to an occupied or an unoccupied electronic state. This is schematically depicted in Fig. 2.1b for the case of 1C-2PPE with a photon energy $h\nu$. Upon variation of the photon energy by $\Delta h\nu$, the final state energy of a feature which arises from an occupied state shifts by $2\Delta h\nu$ because the corresponding state is probed with two photons. This is different, when a peak in the spectrum originates from an unoccupied electronic state, where the peak shift amounts to $1\Delta h\nu$. Another possibility is that a spectral feature is due to a final state which lies above the vacuum level and which is characterized by a vanishing peak shift upon photon energy variation. It is straight forward to transfer this assignment scheme to 2C-2PPE if there is a fixed relation between the two photon energies, e.g. $h\nu_2 = 2h\nu_1$, as is usually the case in our setup. It is important to note that the aforementioned scheme is generally not applicable to electronic states which disperse perpendicular to the surface, most notably bulk bands, because the energy of these states (bands) itself varies with photon energy due to the dispersion as different points in the Brillouin zone are probed.

Another major advantage of 2PPE is the ability to investigate the charge carrier dynamics of a given system on the timescale of the laser pulses, thus typically on the femtosecond timescale, on which electronic relaxation processes take place as well. In such a time-resolved 2PPE (TR-2PPE) experiment, the probe pulse is delayed with respect to the pump pulse by increasing the length of its beam path accordingly. The transient population of an unoccupied electronic state $N(t)$ is implicitly contained in the time-resolved 2PPE intensity of a spectral feature, the cross-correlation (XC). However, the XC is a convolution of the population $N(t)$ with the temporal shapes of the two laser pulses $I_i(t)$, usually assumed to be of Gaussian or sech^2 shape. The convolution of the two laser pulses alone, i.e. in case of a virtual intermediate state, gives the auto-correlation function (AC).

$$\begin{aligned} \mathrm{XC}(t) &= (\mathrm{AC} * N)(t) = (I_1 * I_2 * N)(t) && (2.1)\\ &= \int_{-\infty}^{\infty}\int_{-\infty}^{\infty} I_1(x)\cdot N(y-x)\cdot I_2(t-y)\,dx\,dy && (2.2)\end{aligned}$$

Whereas $N(t)$ may be as simple as an exponential decay function in case of deexcitation of an unoccupied state via a single decay channel, the population dynamics may be more complicated when additional population and decay channels have to be taken into account. The convolution may be replaced by $N(t)$ alone when the duration of the laser pulses is negligible compared to the timescale of population dynamics.

In analogy to angle-resolved direct photoemission, angle-resolved 2PPE (AR-2PPE) experiments give information about the dispersion of electronic states parallel to the surface and hence about the degree of charge carrier delocalization. In our experiments, we rotate the sample in front of the electron spectrometer such that electrons emitted under a different angle ϑ with respect to the surface normal and thus a parallel momentum of

$$k_{\parallel} = \frac{\sqrt{2m_{\mathrm{e}}E_{\mathrm{kin}}}}{\hbar}\sin\vartheta \qquad (2.3)$$

are detected. Unlike the parallel momentum, the momentum component perpendicular to the surface is not conserved in the photoemission process due to the potential discontinuity at the surface. In many cases, such as surface states or image potential states, the dispersion can be approximated by the parabolic dispersion relation of a free charge carrier with an effective mass m^*,

$$E = E_0 + \frac{\hbar^2 k_\parallel^2}{2m^* m_\mathrm{e}}. \tag{2.4}$$

When the photon energy exceeds the work function of the sample, direct photoemission is observed which is much more efficient than 2PPE. Our laser system provides photon energies up to 6.2 eV (see sect. 2.2) and we can thus use it to conduct ultraviolet photoemission spectroscopy (UPS) on most samples. On the other hand, when the photon energy is lower than half the work function, $h\nu < \frac{1}{2}\Phi$, and 2PPE is not energetically possible, an analogous excitation process involving three photons, three-photon photoemission (3PPE), can be observed which usually gives a relatively weak signal but allows e.g. the determination of the work function which is important for the experiments conducted in this thesis.

2.2 Experimental Setup

Photoemission experiments were conducted in a setup which can roughly be divided into an ultrahigh vacuum (UHV) chamber and a laser system for generation of the ultrashort laser pulses. Both parts have not been modified significantly for the experiments conducted in this thesis and their present state has been described very well and in great details elsewhere [148, 116, 149, 150, 147, 114, 141].

The UHV chamber depicted in Fig. 2.2 contains two levels, subdividing the chamber into a preparation and an analysis part (within a single chamber). The single crystal sample is mounted on a flow cryostat with its axis perpendicular to the two levels and is equipped with resistive heating. Therefore, and in combination with a temperature controller (*LakeShore 340*), precise temperature control with an accuracy of less than 1 K can be achieved from around 40 K when cooled with liquid helium to more than 800 K. In order to facilitate exchange of the single crystals without having to break the vacuum, a part of the sample holder can be removed from the cryostat using an in-situ screwdriver and subsequently be transferred with a transfer rod to a sample storage unit or into a load-lock which allows quick removal (insertion) of samples from (into) the UHV system.

For preparation of the single crystal substrates, the upper level contains a sputter gun (*Specs IQE 11-A*) for ion bombardment of the sample with Ar^+ with a beam energy of 1.5 keV in case of Au(111) and 0.9 keV for Bi(111), respectively, under an incidence angle of 45°. After sputtering, the crystal was

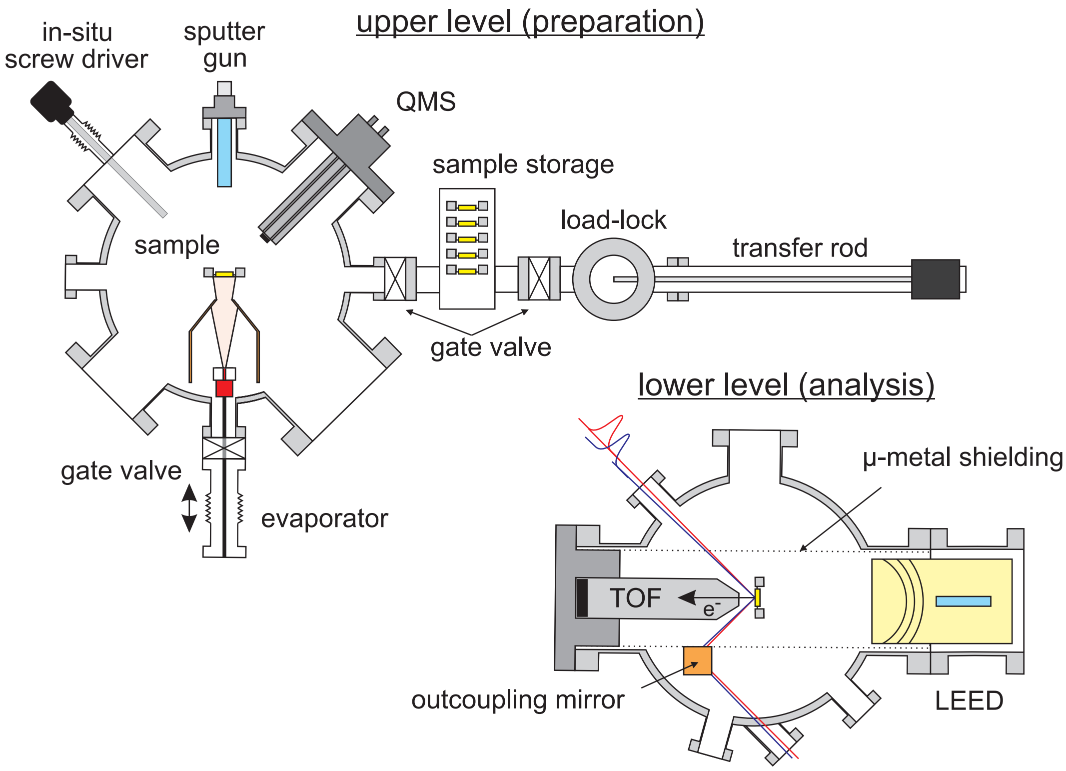

Figure 2.2: Ultrahigh vacuum chamber used in the photoemission experiments. The upper level is equipped with facilities for single crystal preparation (sputter gun), deposition of adsorbates (Knudsen cell evaporator) and characterization with a quadruple mass spectrometer (QMS). Sample transfer into a separable sample garage or a load-lock can be achieved with a transfer rod. The lower level contains the time-of-flight (TOF) spectrometer and facilities for LEED in an environment shielded from stray magnetic and electric fields. Adapted from ref. [147].

annealed at 800 K (Au) or 410 K (Bi), respectively. Thin adsorbate films were produced by evaporating solid materials from a Knudsen cell evaporator (*Kentax TCE-BSC*) at varying temperatures according to Tab. 2.1. The adsorbed films were characterized with a quadrupole mass spectrometer (QMS) with respect to adsorbate composition (fragmentation pattern) and layer thickness as described in the specific chapters. The mass range of our QMS (*Balzers QMG 112A*) allows measurement from 1 to 200 amu.

Photoelectron spectroscopy was performed using the time-of-flight (TOF) spectrometer in the analysis level. The length of the drift tube is 210 mm and the acceptance angle is 6°. The laser pulses were coupled into the UHV chamber through a MgF_2 viewport and are incident on the surface with an angle of 45°. The diameter of the laser beams is on the order of tens of μm, therefore spatial overlap of the beams has to be established with a CCD

Compound	Label	T_D [°C]
10,10'-dibromo-9,9'-bianthryl	DBBA/AGNR	197
6,11-dibromo-1,2,3,4-tetraphenyl-triphenylene	CGNR	137
CGNR (singly N-doped)	N-CGNR	197
CGNR (doubly N-doped)	2N-CGNR	177
di-meta-cyano-azobenzene	DMC	107

Table 2.1: Evaporation temperatures T_D of the compounds presented in this work. DBBA was obtained from *Synthon Chemicals GmbH & Co. KG*. The other compounds were obtained from collaborators as specified in the respective sections of this thesis.

camera positioned outside the chamber at a position equivalent to the sample. To that end, the beams are deflected with a mirror immediately before the viewport. Temporal overlap of the two beams is achieved by scanning the pump-probe delay with a reflector on a precision linear stage and observing a sharp increase in 2PPE signal intensity when both pulses overlap temporally. The signal increase is due to the correlated 2C-2PPE signal.

In order to conduct 2PPE experiments, ultrashort laser pulses with pulse durations of around 50 fs are necessary. Such short laser pulses can be produced in a Ti:Sapphire oscillator (*Coherent Mira 900B*) which is pumped with a Nd:YAG laser at 532 nm (*Coherent Verdi V18*). The emission wavelength can be tuned to a certain degree but was centered around 800 nm in the experiments presented in this work. Since the duration of the pulses is limited by their bandwidth due to the uncertainty principle, a high spectral width is desirable and lies around 30 nm in our setup. A schematic overview of the laser system is shown in Fig. 2.3.

The aforementioned pulses are amplified in a regenerative amplifier (*Coherent RegA 9050*) which is pumped from the same Nd:YAG laser and which converts the output of the Ti:Sapphire oscillator with a repetition rate of 80 MHz and pulse energies on the order of nJ into more intense pulses with energies in the μJ range. Essentially, this is realized by integrating several less intense pulses which reduces the repetition rate to 300 kHz. In order to avoid damaging certain components within the regenerative amplifier, the pulses are temporally stretched before entering the device. In order to regain the necessary temporal resolution, they are compressed again after amplification.

The resulting infrared (IR) pulses ($\lambda = 800$ nm, $h\nu = 1.55$ eV) can directly be used for experiments, or frequency-doubled using β-barium-borate (BBO) crystals. Frequency-doubling the fundamental IR beam twice yields UV light of a photon energy of 6.2 eV which we use for direct photoemission experiments. Since a broader spectral range is desirable and since the ability to vary the

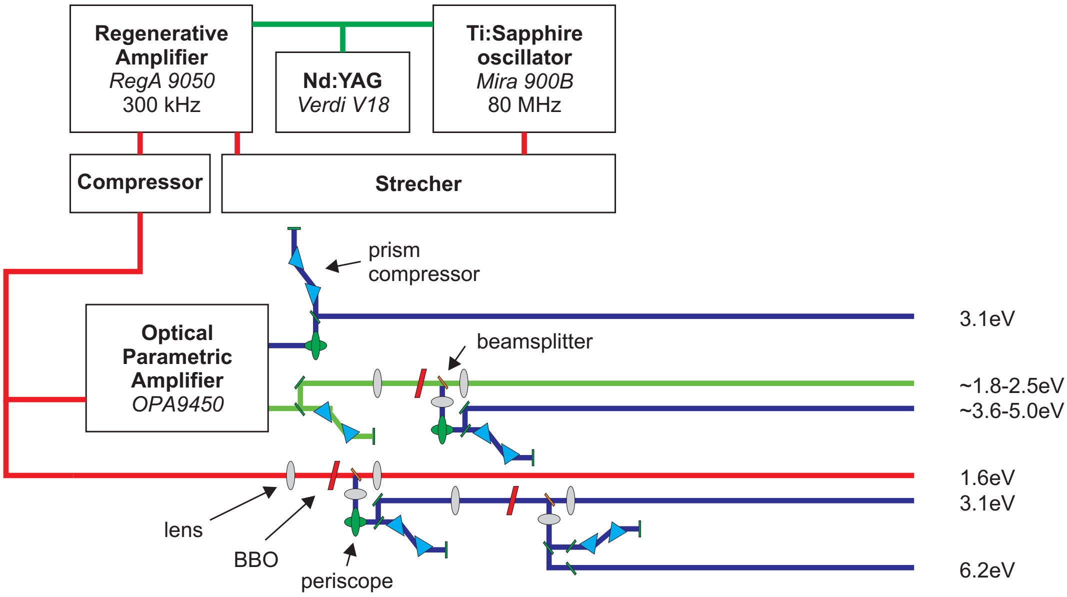

Figure 2.3: Laser setup used for direct photoemission and 2PPE experiments. Infrared pulses are generated in a Ti:Sapphire oscillator and amplified in a regenerative amplifier. Both devices are pumped with a Nd:YAG laser. The resulting intense pulses are used to drive an OPA or immediately for measurements. The OPA converts the pulses into the visible spectrum and provides another source for the second harmonic. All these beams can be frequency-doubled using BBO crystals. Doubling the fundamental infrared beam twice provides 6.2 eV beams for direct photoemission experiments.

photon energy is often necessary to assign features to occupied or unoccupied electronic states, respectively, the intense IR pulses are also used to pump an optical parametric amplifier (OPA, *Coherent OPA9450*) which converts them into pulses of tunable wavelength in the visible regime. Additionally, the OPA provides another source for the second harmonic of the IR fundamental. The visible pulses can be converted into the UV range by another BBO. Most 1C-2PPE experiments are conducted using these UV pulses, while 2C-2PPE usually involves a combination of UV and visible or UV and second harmonic pulses, respectively. With the different beams described above, most of the spectral range from 1.5 to 6.2 eV is covered by our laser system.

As the temporal width of the laser pulses increases in many optical components such as lenses, prisms, etc., they have to be compressed again in order to maintain the necessary intensity and time-resolution. This is achieved using prism compressors [151] which consist of two prisms and exhibit a negative dispersion due to a combination of their geometric alignment and the dispersion within the prism material.

Depending on the requirements by the particular measurement, the laser pulses used for photoemission or 2PPE experiments are characterized with respect to their wavelength, spot profile, duration and intensity. Unless otherwise noted, they are p-polarized when incident on the substrate in front of the TOF analyzer. In order to quantify light-induced reactions by a cross section, work function changes have been analyzed as a function of the photon dose d.

$$d[\mathrm{cm}^{-2}] = 47.686 \times 10^{24} \frac{P[\mathrm{mW}] \times t[\mathrm{min}]}{h\nu[\mathrm{eV}] \times D^2[\mu\mathrm{m}^2]} \tag{2.5}$$

P denotes the time-averaged power of the laser beam, t is the illumination time and D is the laser spot diameter. The spatial profile of the laser spot was fitted with a two-dimensional Gaussian fit function yielding an averaged spot diameter. In the illumination experiments, fluence and pulse energy varied from measurement to measurement but were always on the order of $10^{19\pm1}$ $\mathrm{cm}^{-2}\mathrm{s}^{-1}$ (fluence) and $10^{-2\pm1}$ mJcm^{-2} (pulse energy), respectively. Depending on the efficiency of the light-induced processes, some illumination measurements were carried out by applying a constant photon flux and continuous acquisition of photoemission spectra while in other experiments, cycles of measuring (at lower fluence) and illumination (at higher fluence) were repeated multiple times.

Chapter 3

Thermally Synthesized Graphene Nanoribbons and Light-Induced Coupling of the Precursors on Au(111)

In this first part of the present thesis we will discuss the electronic structure of the species that occur in the individual reaction steps of thermal two-step reactions leading to the synthesis of GNR. Additionally, we will investigate a photochemical coupling of the precursor molecules, and the effect of precursor doping with nitrogen. Before discussing the results of our experiments, we will review the band structure of GNR in general as well as the preceding studies on the systems investigated here. We then turn to the results of this work. Sect. 3.2 covers the synthesis and properties of straight armchair GNR with a width of seven carbon atoms while the effect of doping on the band gap and on the position of the image potential state of a chevron-type GNR is discussed in sect. 3.3.

3.1 Background: Band Structure and On-Surface Synthesis of Graphene Nanoribbons

As already mentioned in the introduction, GNR are one of the possible strategies to introduce a band gap to graphene structures. Additionally, the fact that this is achieved by confinement of the charge carriers by drastically reducing the size of a graphene sheet in one dimension inherently addresses the fact that nanotechnological devices only allow for a limited spatial extent of their components—a requirement which can not be met by bulk graphene. Furthermore, the electronic properties of GNR can be influenced by choosing their geometrical shape, i.e. width and chirality, as well as the incorporation of dopant atoms. The perspective of being able to tailor the electronic structure of GNR in the fabrication process makes them very attractive for the use in nanotechnology.

The synthesis of GNR so far has been relying greatly on top-down methods in which GNR have been derived either from graphene or carbon nanotubes. While these methods allow for the fabrication of a great variety of GNR structures and lithography provides the ability to compose arbitrary mesoscopic structures, which is an important prerequisite for applications, they lack the necessary precision on the sub-nanometer scale, i.e. atomic precision. Consequently, the resulting GNR suffer from a relatively high defect concentration, large widths reflected in small band gaps and limited quality of the edges which however is crucial for the electronic structure. As we will see in sect. 3.1.2, a change of perspective offers an alternative: instead of isolating GNR from superordinate structures, bottom-up synthesis from smaller units, i.e. molecules, provides a solution for all of the above issues.

3.1.1 Band Structure of Graphene Nanoribbons

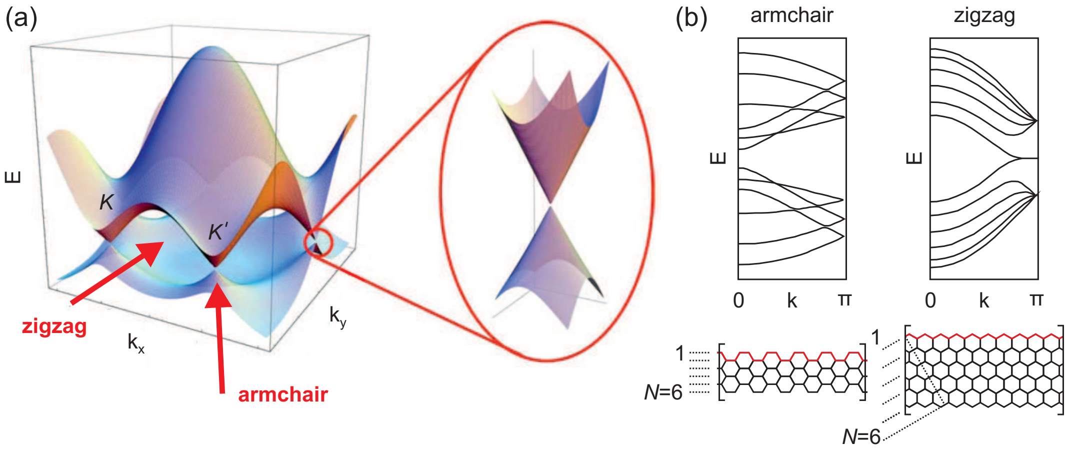

Figure 3.1: (a) Calculated valence and conduction band of graphene. Both bands overlap only at the K- and K'-points of the hexagonal Brillouin zone, forming Dirac cones with linear dispersion. Red arrows indicate the crystallographic directions of armchair and zigzag nanoribbons, respectively. Adapted from ref. [43]. (b) Calculated one-dimensional band structures for an $N = 6$ armchair and an $N = 6$ zigzag nanoribbon, respectively. The wave number k is normalized to the lattice vector. The nomenclature for the width is illustrated using the depictions of the two GNR. Adapted from ref. [49].

The most interesting properties of graphene are related to its electronic structure, specifically its valence (VB) and conduction bands (CB). Fig. 3.1a depicts the dispersion of both bands in the hexagonal Brillouin zone. The bands are energetically separated most at the central Γ-point and overlap only in six points, the K- and K'-points at the corners of the Brillouin zone. In the vicinity of these points the VB and CB form a Dirac cone which is characterized by a linear dispersion relation $E = \hbar v_{\mathrm{F}} k$, where v_{F} is the Fermi velocity which in graphene amounts to a relatively large value of 1×10^6 ms^{-1} [43]. In this regime and in the limit of a vanishing charge carrier concentration, the electrons and holes behave like massless Dirac particles [41].

A GNR can be thought of as a long strip cut out of a graphene sheet. Considering that there are different crystallographic directions, along which the GNR can be cut out, there are different types of GNR which are most intuitively characterized by their edges. The orientation of the GNR axis within the fictitious graphene sheet is referred to as 'chirality'. Fig. 3.1b depicts two prominent types of GNR: armchair and zigzag GNR. The nomenclature is analogous to the one for carbon nanotubes. Together with the width w and the length, these categories fully characterize the system. The width is often denoted in terms of the number of carbon atom rows N counted perpendicular to the ribbon axis, as indicated in Fig. 3.1b.

The behavior of the charge carriers in quasi-one-dimensional GNR are usually described by a one-dimensional band structure. In most theoretical studies, the GNR are assumed to be infinitely long. Under this condition, calculations can be performed quite efficiently due to the periodic boundary conditions and the small unit cell. The opening of a band gap, in contrast to bulk graphene, is one of the main reasons for the technological interest in GNR. While modern calculations give quantitatively more accurate results, the basic properties of the band structure of GNR can be understood if we approximate it as a projection of the valence and conduction bands of graphene along the direction which is associated with the chirality of the GNR [49]. The red arrows in Fig. 3.1a indicate these two directions for armchair and zigzag GNR. For armchair GNR, the mere projection gives a one-dimensional band structure with a Dirac cone at the Γ-point whereas the one-dimensional band structure for the zigzag GNR results in a large gap at the Γ-point and a Dirac cone in the outer region of the Brillouin zone.

Fig. 3.1b depicts calculated band structures for an armchair and a zigzag GNR, respectively, each with a width of $N = 6$ [49]. While these tight-binding calculations from 1996 are outdated, they nicely illustrate the band structure qualitatively. In contrast to a simple projection of the graphene band structure, we find a direct band gap at the Γ-point of the armchair GNR. The opening of this gap is due to the lateral quantum confinement of the charge carriers perpendicular to the GNR axis. Along with the opening of the band gap comes a non-vanishing mass of the charge carriers, which, thinking of technological applications, is the 'cost' of the band gap. In the zigzag GNR, a pair of metallic states is found instead of a Dirac cone. Note, that these states are not a 'washed-out' Dirac cone but that they are exclusively found in GNR and are localized at the edges of the zigzag ribbon which is why they are referred to as *edge states* [49, 58, 59].

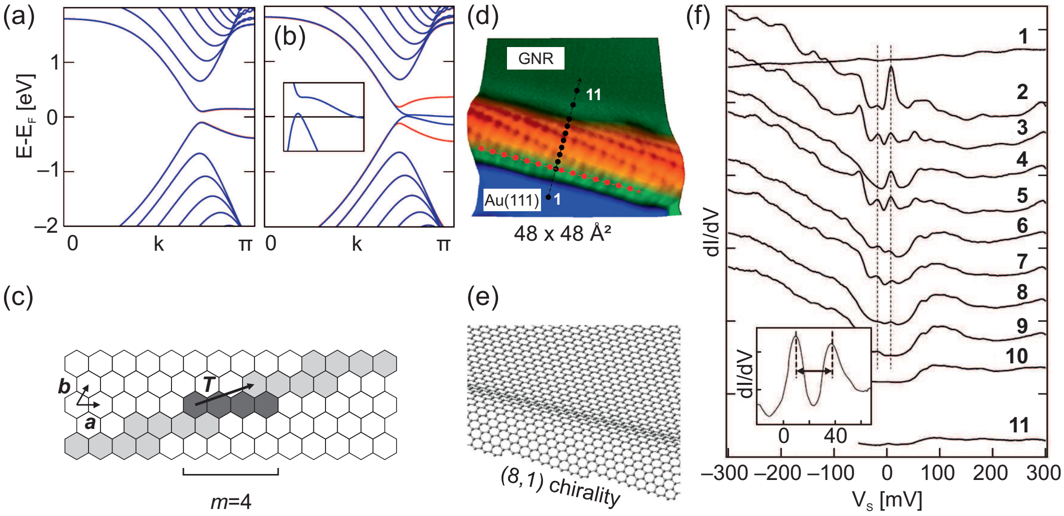

Figure 3.2: Edge states associated with zigzag edges. (a) Spin-resolved calculated band structure of a zigzag GNR (N=17) without external electric field. The wave number is normalized by the lattice vector. The calculations were performed with DFT using LSDA. (b) Analogous calculation with an external electric field of 0.1 VÅ^{-1} applied perpendicular to and in the plane of the GNR. The red and blue line represent states with different spin configuration. The inset shows a magnification in the range of 50 meV around E_F (horizontal line) and $0.7 \leq ka \leq \pi$. Both (a) and (b) were adapted from ref. [59]. (c) Characterization of chiral GNR using the chiral vector **T**. Adapted from ref. [50]. (d) STM image of a chiral (8,1) edge with a width of 19.5 nm (V_S = 0.3 V, I_t = 60 pA). (e) Structural model for the GNR shown in (d). (f) dI/dV spectra measured at locations represented by black dots in (d). The inset shows a measurement with higher resolution on the edge of a (5,2) GNR with 15.6 nm width. Figures (d-f) were adapted from ref. [62].

As revealed by more recent calculations [59] using DFT and the local spin density approximation (LSDA) which allows spin-resolved calculations, edge states are not metallic but there is a small gap between the two edge states, which is shown in Fig. 3.2a. Nevertheless, the bands are degenerate with respect to the two spin states. This degeneracy is lifted in the presence of external electric fields which are applied perpendicular to the axis and in the plane of the GNR (see Fig. 3.2b). In this case, both edge states of one spin configuration become metallic while the two counterparts with opposite spin

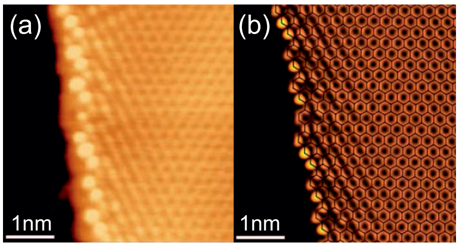

Figure 3.3: (a) Atomically resolved STM image of the edge of a (2,1) chiral edge ($V_S = -0.97$ V, $I_t = 50$ pA). Adopted from ref. [63]. (b) Simulated STM image for the same edge as in (a) from first principles using the Tersoff–Hamann approximation and the same bias as in the experiment. Adopted from ref. [63].

become more insulating. The same degeneracy lifting is predicted for zigzag GNR in contact with a ferroelectric polymer [61].

Besides the two GNR types described above, armchair and zigzag, there are others with a continuous variation of the chirality which are consequently referred to as *chiral GNR*. The edges of chiral GNR posses a mixed, partly armchair, partly zigzag character which is also reflected in their electronic structure. For characterization of such systems, the chiral vector $\mathbf{T} = \pm q\mathbf{a} + \mathbf{b}$ is used following the classification by Ezawa [50], which is illustrated in Fig. 3.2c. $\mathbf{a}$ and $\mathbf{b}$ denote the lattice vectors of graphene and q is one of the two scalar parameters used to label the chiral GNR. While the chiral vector describes the orientation of the GNR axis within a fictitious graphene sheet, a second parameter describing the width of the GNR is necessary in order to fully characterize the system. The second parameter $p = m - q$ is related to the width via m, which is the number of adjacent phenyl rings along the zigzag direction (see Fig. 3.2c). The chirality is denoted as (p,q).

The above described edge states have also been observed experimentally. Fig. 3.2d shows a topographic STM image of a chiral (8,1) GNR's edge with atomic resolution. The edge is dominated by a curvature of the ribbon with an extension of 3 Å above the mid-GNR plateau [62]. Fig. 3.2e shows the corresponding structure model. Scanning tunneling spectroscopy (STS) reveals two electronic states close to the Fermi level which are observed only near the chiral GNR edge (see Fig. 3.2f). Despite the fact that this particular GNR is not a perfect zigzag GNR, its zigzag character is quite pronounced. In contrast, the (2,1) GNR shown in Fig. 3.3 possesses an edge with a more balanced armchair/zigzag characteristic. As revealed in STM and first-principles calculations, an edge state is observed even in this case but it is located only at the zigzag intervals of the edge. As we will see later on in this thesis in line with other experiments as well as calculations, edge states are also observed at the short edges of finite armchair GNR, i.e. at their zigzag-shaped ends [13, 152, 153, 60].

We have already observed that unlike graphene, both armchair and zigzag GNR possess a band gap but so far haven't addressed its magnitude. Numer-

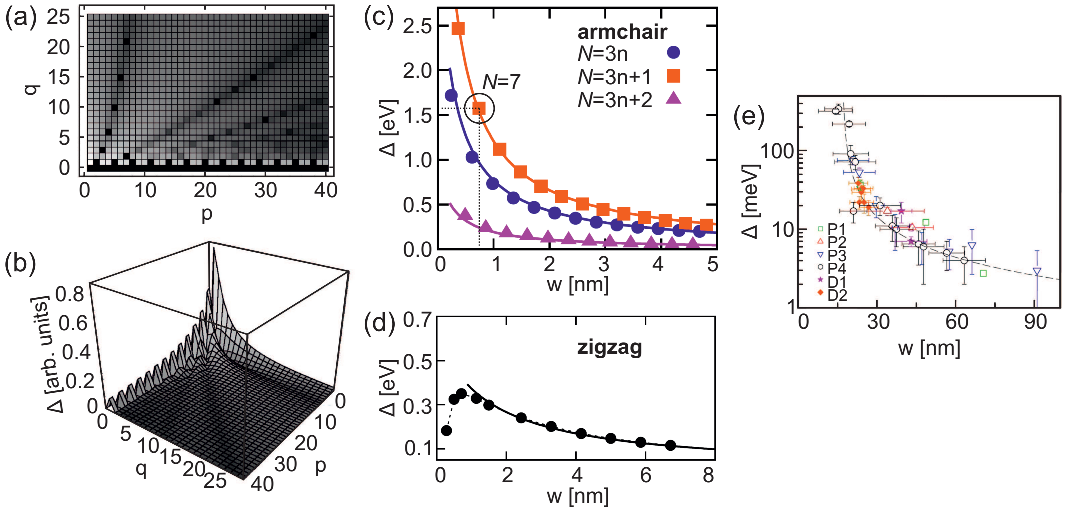

Figure 3.4: (a,b) Tight-binding calculations of the band gap for chiral GNR. The chiral GNR are characterized by two parameters p and q which are explained in the text. Adopted from ref. [50]. (c) Calculated width dependence of the band gap Δ for armchair GNR using DFT with LSDA. Each trace corresponds to one width category. The $N = 7$ armchair GNR which will be studied in this thesis is highlighted. Adopted from ref. [52]. (d) Calculated band gaps for zigzag GNR with varying width using DFT and LSDA. Adopted from ref. [52]. (e) Measurement of the width-dependent band gap of six different sets of lithographically fabricated GNR categorized into device types P1 through P4, D1 and D2. Adopted from ref. [53].

ous studies have dealt with the size of GNR band gaps, both experimentally and theoretically [51, 52, 53, 54, 55, 56, 57]. Generally, the band gap Δ is reduced with increasing GNR width w, independent of chirality, as shown in Fig. 3.4a,b. Tight-binding calculations show the behavior of the gap nicely for a large variety of chiral GNRs but they suffer from a shortcoming of the tight-binding approach, namely that some armchair GNR (for every $N = 3p + 2$, with p a natural number) are predicted to be metallic, contrary to more recent results and experiments [52]. The band gap of zigzag GNRs is generally smaller than that of armchair GNR. As shown in Fig. 3.4c, the band gap of armchair GNR varies periodically with varying width, additionally to the general inverse width-dependence [52] and armchair GNR can thus be classified into three categories where each category is comprised of the GNR with widths N that differ by an integer multiple of three. The band gap of the armchair GNR shown here is generally on the order of electronvolts which characterizes them as semiconducting. An analogous calculation performed for zigzag GNR shows qualitatively the same trend, except for very small GNR widths where the gap is reduced with decreasing width (see Fig. 3.4d) [52]. Experimentally, the inverse relation between band gap and width has been confirmed by

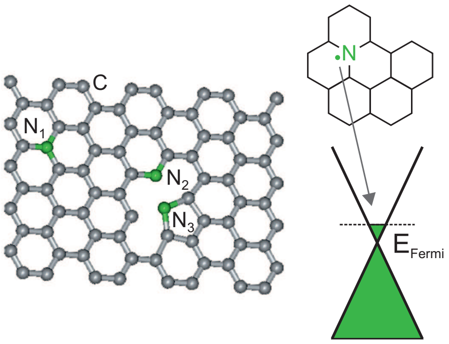

Figure 3.5: Nitrogen doping. Incorporation of nitrogen in graphene structures can occur at three different sites N_1, N_2 and N_3. The principle effect on the electronic structure of graphene is the release of the additional electron into the conduction band. Adapted from ref. [66].

conductance measurements [53] and STS [62]. Fig. 3.4e shows the result of conductance measurements on lithographically fabricated GNR with varying width and chirality. In agreement with theory, an inverse relation between band gap and width is found. This behavior seems to be independent of the chirality which the authors ascribe to imperfect edges which are due to the fabrication process employed [53].

Thinking of the implementation of GNR in nanotechnological devices, the observed influence of the GNR geometry on the band structure allows, in principle, to deliberately design a GNR with regard to its electronic properties. We have seen that the size of the gap can be influenced by varying the GNR width. In a device, the electronic structure of the environment has to be taken into account as well and a way to arbitrarily align the bands of materials with a common interface would be beneficial. Such an alignment requires a shift of the band structure with respect to the Fermi level. Doping graphene or GNR with nitrogen has such an effect, as sketched in Fig. 3.5. The additional electron of the dopant leads to an n-doping as it integrates into the conduction band of graphene [64, 65, 67, 68]. The opposite effect occurs upon doping with boron which leads to p-doping [154, 155]. Fortunately, doping does not lead to a significant loss of conductivity [156]. The effect of doping furthermore depends on the site which is substituted with the dopant atom. This is particularly important when doping GNR via modification of the precursors, as will be demonstrated in this thesis. Since it is desirable to control the size of the band gap and its alignment with the chemical potential of the surrounding independently, pyridinic nitrogen substitutions at the edges (N_2 in Fig. 3.5) are of particular interest, since they result in n-doping but leave the size of the gap largely unaffected. This is in contrast to bulk substitutions, which lead to a reduction of the gap size [64, 66].

3.1.2 Thermal On-Surface Synthesis of GNR from Molecular Precursors

Halogen-substituted molecules have been known to self-assemble into different nanostructures on surfaces. Upon deposition on the substrate, the molecules remain intact but thermal dissociation of the Br or I atoms activates the molecules by creating a radical or multi-radical molecular state. The elevated temperature allows diffusion of the molecules which leads to directional covalent coupling. The resulting nanostructure, e.g. a chain or network, is determined by the geometry of the precursor molecules [35, 12, 75]. Using different halogens in the same molecule, a "hierarchical" two-step reaction can be induced which offers an extension of the concept toward increasingly complex patterns [76].

In contrast to conventional GNR fabrication techniques such as lithography [70, 53] and unzipping carbon nanotubes [71, 72, 73], bottom-up synthesis offers the ability to produce atomically precise GNR with a well-defined electronic structure [77, 78, 157]. However, this strategy comes with different challenges, most notably the inability to write arbitrary patterns (which we will address in the framework of this thesis, see sect. 3.2.5).

Fig. 3.6a,b shows the two-step on-surface synthesis of an $N = 7$ armchair GNR on Au(111) from molecular precursors which is thermally activated. This work by Cai *et al.* from 2010 marks the first successful on-surface synthesis of a GNR [77] and we will investigate the resulting GNR as well as the reaction process extensively in this thesis. Henceforth, we will use the acronym *AGNR* representative of this specific system. A Br-substituted bianthryl precursor molecule (10,10'-dibromo-9,9'-bianthryl, DBBA) is deposited on a Au(111) surface through thermal evaporation into UHV. Cai *et al.* state that the "thermal sublimation of the monomers onto a solid surface removes their halogen substituents" [77], which however is a (reasonable) assumption based on a comparable system [35]. Another possibility is that dehalogenation occurs later, during the annealing step leading to polymerization. We will address this issue using STM and temperature-programmed desorption in this thesis (see sect. 3.2.1 and 3.2.2).

Either way, the first heating step at 200 °C induces molecular diffusion of the dehalogenated, biradical precursor molecules on the surface which leads to directional covalent coupling of the DBBA units, forming a linear polyanthrylene polymer. In this structure, the anthrylene units are inclined with respect to the surface plane in an alternating sequence due to steric repulsion, which is reflected in a double row of protrusions in STM (see Fig. 3.6c). The further reaction path of the dissociated Br atoms has been given relatively little attention in the above study. While the Br atoms are not observed in

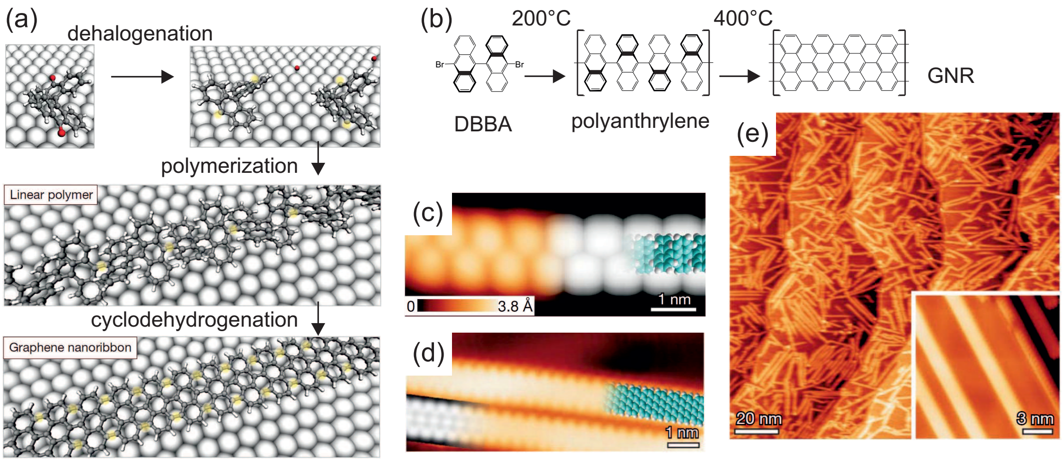

Figure 3.6: Synthesis of AGNR on the Au(111) surface. (a) Structure models of the reaction steps. In the first step, the adsorbed DBBA is dehalogenated, leaving radical species and Br atoms on the surface. In the subsequent polymerization step, covalent coupling of the DBBA radicals leads to the formation of a polyanthrylene chain. Upon heating this polymer, a cyclodehydrogenation reaction yields the fully aromatic AGNR. (b) Depiction of the reaction scheme with Lewis structures. (c,d) STM images of (c) the polyanthrylene chain ($V_S = 1.9$ V, $I_t = 80$ pA) and (d) the AGNR ($V_S = -0.1$ V, $I_t = 0.2$ nA) together with partially overlaid DFT-based simulations of these STM images. (e) Overview STM image showing multiple AGNR which are isotropically oriented. The inset shows an image taken with higher resolution. ($V_S = -3$ V, $I_t = 0.03$ nA, inset: $V_S = -1.5$ V, $I_t = 0.5$ nA). Figures (a), (c), (d) and (e) were adapted from ref. [77].

STM after polymerization, they might well be adsorbed on the surface in this stage of the reaction and possibly influence the synthesis of the GNR. STM might not be able to observe Br atoms if they diffuse on the surface at the respective temperatures, are incorporated into the polyanthrylene structure (e.g. beneath the upstanding anthrylene parts) or diffuse to step edges. In fact, a recent computational study suggests that the desorption temperature of atomic halogens on noble metal surfaces is significantly higher than the temperatures necessary for self-assembly processes [158]. Furthermore, it was found that the metallic substrates lower the barrier for dissociation of halogenated organic compounds. In sect. 3.2.2 we will see that indeed the Br atoms are still present on the surface after the polymerization reaction.

In a second step, the polyanthrylene undergoes a cyclodehydrogenation reaction upon further thermal activation at 400 °C. Such a reaction has also been observed for other nanographenes [159]. The resulting flat, fully aromatic AGNR do not show defects or irregularities and have a width of 0.74 nm (see Fig. 3.6d). They are isotropically oriented on the surface, as seen in Fig. 3.6e with no preferential alignment along the herringbone reconstruction of

Method	Environment	VB [eV]	CB [eV]	Δ [eV]	Ref.
DFT (LDA)	in vacuum	–	–	1.6	[52]
DFT (PBE)	in vacuum	–	–	1.5	[51]
DFT (HSE)	in vacuum	–	–	2.1	[51]
GW	in vacuum	–	–	3.7	[55]
GW-IC	on Au(111)	–	–	2.3–2.7	[163]
DFT-D2 (PBE)	on Au(111)	–	–	1.5	[164]
STS / ARUPS	on Au(111)	−0.7	+1.6	2.3	[163]
ARUPS / IPES	on Au(788)	−0.9	+1.9	2.8	[160]
STS	on Au(111)	−1.1	+1.6	2.7	[13]
This work	on Au(111)	−1.2	+1.4	2.6	

Table 3.1: Electronic structure of the AGNR. Energetic positions of the valence and conduction bands, respectively, as well as the band gap, determined by theoretical and experimental methods. PBE: Perdew-Burke-Enzerhof realization of the general gradient approximation. HSE: Hybrid density functional suited to reproduce experimentally observed band gaps [51]. GW: Green's function approach (G) based on the screen Coulomb interaction (W). GW-IC: GW with image charge corrections to account for the interaction with the Au(111) substrate. DFT-D2: DFT calculation using PBE and dispersion correction which is included with the DFT-D2 approach by Grimme. STS data reported in ref. [163] are derived from the onsets of the bands. For the values derived in this work, see sect. 3.2.4.

Au(111). The same fabrication procedure has also been applied on the stepped Au(788) surface where AGNR can be successfully produced with a mean length of 23 nm and align along the steps [160]. The on-surface cyclodehydrogenation reaction has been studied in detail using dispersion-corrected DFT [161] and the study suggests that the dehydrogenation is catalyzed by the metallic substrate. In the initial step, two H atoms are dissociated from the polyanthrylene and adsorbed on the Au(111) surface, followed by C–C coupling. This reaction then lowers the barrier for dehydrogenation in the adjacent anthrylene units resulting in a chain reaction along the polymer [161]. Experimentally, the same thermally induced on-surface synthesis yielding AGNR can be observed on the Ag(111) surface which demonstrates a certain degree of versatility of this method [77]. Non-thermal cyclodehydrogenation of single anthrylene units in the polymer can furthermore be achieved by hole attachment in an STM junction (bias below approx. −2 V) which allows the production of an intra-ribbon heterojunction [162].

The on-surface synthesis described here constitutes an important step in the research on GNR because it allows fabrication of GNR with a well-defined edge structure but also because, unlike top-down approaches, it is capable of producing sufficiently narrow GNR to obtain a band gap on the order of electronvolts. For the $N = 7$ armchair GNR observed here, which has a width of 0.74 nm, different calculations using DFT and various functionals have been conducted (see Tab. 3.1). While earlier calculations using simple DFT functionals such as LDA and GGA (PBE) give a band gap of less than 2 eV [52, 51], the value obtained from Green's function calculations (GW approach) yields a higher value of 3.7 eV [55]. Taking into account the electron–electron interaction with the metallic substrate by image charge corrections, the GW value is reduced to 2.3 to 2.7 eV [163]. Another study of the AGNR on Au(111) has found a band gap of 1.5 eV by employing DFT with DFT-D2 dispersion corrections. Using surface-sensitive electron spectroscopies, we will obtain an experimental band gap of 2.6 eV (as described in sect. 3.2.4), in relatively good agreement with other experimental studies carried out since. These experimental results will be discussed in the context of our own measurements, but the corresponding values are shown in Tab. 3.1.

Despite the numerous studies of the AGNR system which have been carried out over the past years, some questions remain. The structure of the monomer phase which occurs after deposition of DBBA onto a substrate at room temperature has so far not been studied, particularly with respect to the question whether the precursor adsorbs intact or in a dehalogenated form and with respect to the reaction pathway of Br after dissociation. The electronic structure of the intermediate polyanthrylene has also not been investigated up to now. All these issues will be addressed in the work presented here.

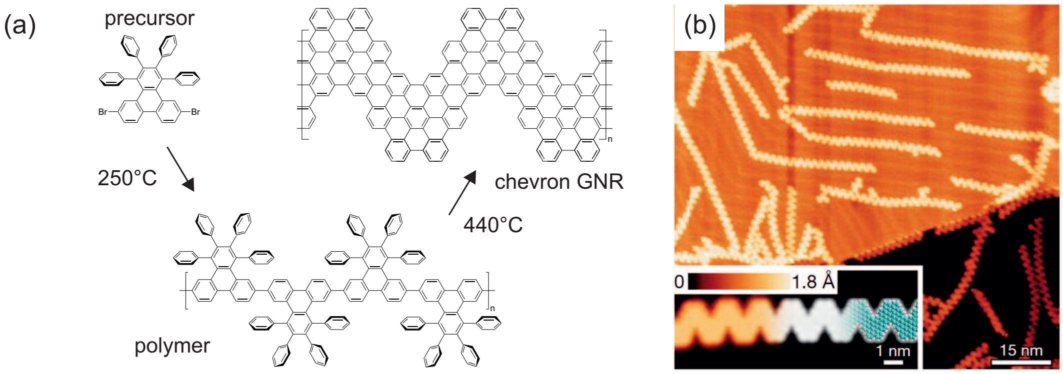

Figure 3.7: Synthesis of the CGNR on the Au(111) surface. (a) Reaction scheme for the two-step thermal process. The adsorbed molecular precursor undergoes a polymerization. The polymer is three-dimensional and after the second heating step, a fully aromatic chevron GNR is obtained. (b) Overview STM image over the adsorbed CGNR on the Au(111) surface. The nanoribbons align with the herringbone reconstruction of the substrate. The inset shows a high-resolution image of one CGNR together with a partially overlaid DFT-based simulation of the STM image ($V_S = -2$ V, $I_t = 20$ pA, inset: $V_S = -2$ V, $I_t = 0.5$ nA). Adapted from ref. [77].

Besides the AGNR system, the paper by Cai *et al.* reports on a second GNR which can be produced by on-surface synthesis. Fig. 3.7a shows the synthetic route toward this chevron-type GNR, henceforth referred to as CGNR. A different precursor molecule (6,11-dibromo-1,2,3,4-tetraphenyl-triphenylene) adsorbed on Au(111) performs a thermally induced polymerization at 250 °C and the resulting twisted polyphenylene reacts toward a fully aromatic, flat GNR upon heating to 440 °C. This CGNR can be seen as composed of two alternating armchair-edge sub-ribbons, namely an $N = 9$ and an $N = 6$ GNR and thus it has partly larger and smaller width compared to the AGNR, respectively. It is conceivable that the chevron-type shape of the overall ribbons has an effect of the electronic band structure in general and, specifically, electron transport properties. Just as the AGNR, the CGNR does not show any defects, as seen in the inset of Fig. 3.7b. Unlike the AGNR, the CGNR align preferentially with the herringbone reconstruction (see Fig. 3.7b) and have a typical length of 20 to 30 nm with longer ribbons being particularly rare which is ascribed to the length-limiting interaction with the soliton lines which have typical lengths on this order [77]. The CGNR, too, can be grown in parallel orientation with respect to each other on the stepped Au(788) surface [160]. Calculations using DFT (GGA) and a “tight binding $+U$” (TBU) approach consistently predict a band gap of 1.5 eV for the CGNR in vacuum [165].

3.2 Synthesis of Straight Armchair GNR and Light-Induced Precursor Dimerization

This section comprises the results of experiments conducted on the $N = 7$ armchair GNR (AGNR) which is synthesized on a Au(111) surface from molecular precursors. In sect. 3.2.1, the geometric and electronic structure of the adsorbed monomers is investigated. In sect. 3.2.2, we follow the thermal on-surface reaction by detection of different molecular fragments during thermal desorption. The electronic structure of the intermediate polymer and the final AGNR are investigated and compared in sects. 3.2.3 and 3.2.4. Finally, we discuss a photo-induced covalent coupling of the adsorbed monomers in sect. 3.2.5.

3.2.1 Characterization of the Monomer Phase with 2PPE and STM

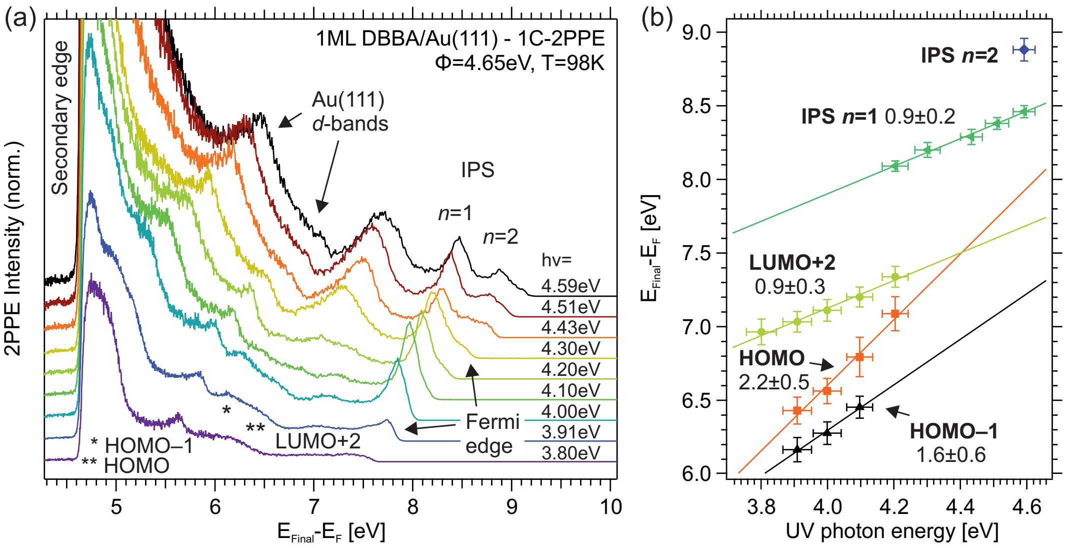

Figure 3.8: (a) 1C-2PPE spectra of the DBBA-covered Au(111) surface for different photon energies $h\nu$ between 3.80 eV and 4.59 eV. The sample temperature during measurement was 98 K. A total of seven features are observed: two originating from the Au d-bands, two associated with the first and second IPS as well as three molecule-induced features. The spectra have been normalized with respect to one of the d-band peaks. (b) Energetic shift of the non-bulk states observed in (a) displayed over the photon energy. The corresponding slopes are shown in the figure.

Before investigating the AGNR and the intermediate polymer, we turn to the DBBA precursor monomers directly after adsorption on the Au(111) substrate at room temperature (sample held at 300 K). A coverage of one monolayer (ML) was achieved by adjusting the evaporation time and the resulting adsorbate layer was characterized by temperature-programmed desorption (TPD) of the anthracene units as described in the following section 3.2.2. The subsequent measurements presented here were conducted with the sample cooled to cryogenic temperatures.

We used 1C-2PPE to study occupied and unoccupied electronic states of the DBBA monolayer. As we will see in sect. 3.2.5, a light-induced reaction can be observed for this phase but the measurements shown here were obtained using photon doses on the order of 10^{21} cm^{-2} which are negligible compared to those used to drive the reaction (on the order of 10^{23} cm^{-2}). In the photon energy dependent 2PPE experiment shown in Fig. 3.8a, several features can be observed. Their final state energies shift with varying photon energy, as can be observed in Fig. 3.8b. Two prominent peaks are common to 2PPE spectra recorded on the Au(111) surface and are assigned to the occupied bulk d-bands, the onset of which lies at around -2 eV [166, 114]. Close to the Fermi edge, we observe two features, one more intense than the other, in the spectrum with $h\nu = 4.59$ eV. In some spectra with lower $h\nu$, the two peaks can not or only partly be observed which indicates that they shift less with the photon energy than the Fermi edge and consequently, that the corresponding electronic states are not occupied. The peak with higher intensity shifts with a slope of 0.9 ± 0.2 which demonstrates that the corresponding electronic state is unoccupied while the smaller feature can only be clearly observed in one spectrum and thus no slope can be determined. Nevertheless, since the Fermi edge, which cuts off the less prominent peak at lower photon energies, shifts with twice the photon energy, the slope of this peak's shift must be smaller than two. By subtracting the photon energy from the final state energies we obtain binding energies of 3.88 ± 0.06 eV and 4.29 ± 0.08 eV, respectively, relative to the Fermi level. The work function (which can be directly read as the position of the secondary edge from the final energy scale) amounts to 4.65 ± 0.01 eV and thus, the two states lie 770 meV and 360 meV below the vacuum level, respectively. Angle-resolved 1C-2PPE reveals that the intense peak disperses with an effective mass of 1.2 ± 0.4 while the dispersion of the less intense feature can not clearly be determined as the corresponding spectral region is dominated by the intense, dispersing feature at higher $k_{\|}$. Due to the energetic position and the dispersion, we identify the two corresponding electronic states as image potential states (IPS) with the first quantum numbers $n = 1, 2$. These states localized at the adsorbate–vacuum interface, which are caused by the attractive interaction of a charge carrier on the vacuum side with its own image charge within the metal are a common feature in 2PPE spectra on adsorbate-covered metallic surfaces [167, 168, 146, 169, 170, 171, 172]. Since we cannot determine the slope of the peak assigned to the $n = 2$ IPS directly but we only observe that it shifts with a slope smaller than one, it might also arise from a final state with an energetic position above the vacuum level of the sample. Such a state would exhibit no peak shift at all. In 2C-2PPE spectra recorded along with the 1C spectra shown here, we find two features with identical width, intensity ratio and dispersion as the two peaks assigned to IPS here. Since the peaks occur at different final state energies due to the different probe photon energy in 2C-2PPE, we can rule out that they arise from electronic final states.

Between the d-band features and the two IPS, three additional features can be observed with relatively low intensity for $h\nu < 4.20$ eV and with an increased intensity at higher photon energies. Based on the peak shift with a slope of two (shown in Fig. 3.8b), two of them can be assigned to occupied electronic states, namely the highest occupied molecular orbital (HOMO) at -1.39 ± 0.11 eV and the HOMO-1 at -1.70 ± 0.09 eV, respectively. These states are also observed in STS (see Fig. 3.9e,f) and do not show a dispersion in angle-resolved 2PPE. The third feature is characterized by a slope of 0.9 ± 0.3 and can thus be assigned to an unoccupied state. Since it does not disperse parallel to the surface, like the occupied molecular orbitals, we can assign it to an unoccupied molecular orbital of the adsorbed DBBA. In light of the two unoccupied states observed in STS (see below) the feature is labeled LUMO+2 (LUMO: lowest unoccupied molecular orbital). Its binding energy, as determined from this measurement, is 3.12 ± 0.08 eV with respect to the Fermi level. The intensity increase observed in the spectra recorded with higher photon energies is due to a resonant excitation of the occupied molecular orbitals via this state.

Besides the electronic structure, the geometrical assembly of the DBBA monomers on the Au(111) surface is of interest because it may give insight in the strength of molecule–substrate and molecule–molecule interaction. Additionally, the structural arrangement of the molecules is important for the photo-induced process discussed in sect. 3.2.5 and the question of whether or not dehalogenation occurs during or after adsorption, which has not been answered in preceding studies. The STM and STS experiments presented here have been conducted by Bo Chen in the group of Prof. Franke (Freie Universität Berlin) [173] in the framework of a collaboration in which the author of the present thesis has contributed to the design of the experiment as well as the discussion and publication of the results [174].

In the sub-monolayer regime on Au(111), DBBA molecules adsorb in islands which consist of rows aligned along the herringbone reconstruction of the substrate. Additionally, the rows consisting of alternating protrusions preferably terminate at the kinks of the herringbone reconstruction which implies

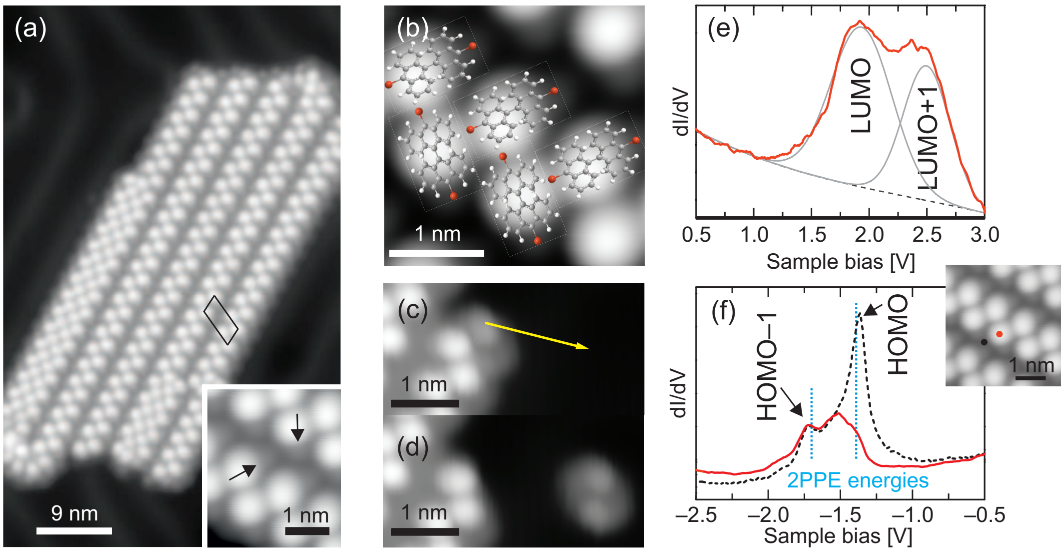

Figure 3.9: STM and STS experiments on the DBBA precursors on Au(111) performed in collaboration with the group of Prof. Franke (Freie Universität Berlin). (a) Overview STM image of a DBBA island with the unit cell. The inset shows a high-resolution STM image with highlighted side-protrusions. The temperature during the measurement was 4.5 K (both: $V_S = 2.0$ V, $I_t = 0.1$ nA). (b) Row of DBBA dimers within the same island together with an overlaid structure model (grey: C, red: Br, white: H, $V_S = 2.0$ V, $I_t = 0.1$ nA). (c,d) Lateral manipulation of a single DBBA molecule away from the edge of an island, as indicated by the arrow ($V_S = 0.56$ V, $I_t = 28$ pA). (e,f) ST spectra acquired in constant current mode ($I = 40$ pA) in the regime of (e) unoccupied and (f) occupied electronic states. The ST spectra depicted in red were recorded in the center of a DBBA protrusion. The spectrum in the unoccupied regime was fitted with two Gaussian fit functions (grey). (f) shows an additional spectrum (dashed, black line) recorded between two dimer rows (position of the black marker in the inset). The energies for HOMO and HOMO$-$1, as determined from 2PPE, are shown as blue, dashed lines.

molecule–substrate interaction. In most cases, the rows consist of two lines of protrusions whereas occasionally, more lines are observed within one row. As seen in the inset of Fig. 3.9a, each protrusion is accompanied by a less intense feature. The orientation of the side feature with respect to the main protrusion is always the same within a line but different for the two lines within one row (i.e. the rows are not symmetric with respect to inversion). Nevertheless, the orientation of the side protrusion is always the same on a given side of every row. The high degree of ordering which is evident from the orientation of the side protrusions is indicative of molecule–molecule interaction. However, this intermolecular forces do not have a covalent character: Fig. 3.9c,d shows a tip-induced manipulation where a single (intense) protrusion is removed from the edge of a DBBA island. This furthermore demonstrates that one protrusion corresponds to one entire molecule. When the molecule is removed from the island, the overall apparent height is reduced and the structure changes toward a two-lobe shape. This is most likely due to a relaxation of the molecule toward the surface once it is isolated from the island, in which the monomers are intertwined to a certain degree. The unit cell of the well-ordered DBBA islands (see Fig. 3.9a) has a size of 2.2 nm^2.

Fig. 3.9b shows a high-resolution STM image of a row of DBBA dimers overlaid with a structure model. The side protrusions are due to the Br substituents and the intense feature arises from the twisted, three-dimensional bianthryl backbone of the molecule. Note, that the DBBA monomers shown in the model have a dihedral angle (angle between the planes of the individual anthracene units) of 90°, as in the free molecule. Due to attractive interactions with the substrate, one can expect this angle to be lowered when the molecules are adsorbed on the surface, in the sense that the molecule is pulled toward the surface. Br atoms of one DBBA molecule and the upstanding part of an anthracene unit of a neighboring molecule can therefore be expected to be partially stacked in order to avoid steric hindrance. The formation of double rows containing (usually) two dimer lines can not be understood from the presented structure model because the two sides of a dimer line are equivalent. The formation of uniform islands or the occurrence of single lines would be equally conceivable. Considering the strong tendency of the DBBA adsorbate structure to align with the underlying herringbone reconstruction, preferential adsorption on certain sites (e.g. the hexagonally close-packed or face-centered cubic sites) might explain the observed rows. Due to an incommensurability of the inter-row distance of the adsorbate structure and the width of the soliton lines, it is conceivable that occasionally one row is comprised of more than two lines of protrusions.

Scanning tunneling spectroscopy (STS) allows to locally probe occupied and unoccupied electronic states of an adsorbate molecule. Fig. 3.9e shows constant-current STS recorded in the energetic regime above the Fermi level and in the center of the intense DBBA protrusion. Fitting the data with two Gaussian peaks profiles, we find two adsorbate-induced peaks at 1.93 eV and 2.50 eV which we assign to the LUMO and the LUMO+1. Features associated with these two unoccupied molecular orbitals are not observed in the 2PPE spectra discussed above, most likely due to their energetic position within the projected d-band gap of the substrate along the [111] direction. STS data of the occupied electronic states (see Fig. 3.9f) are consistent with the HOMO and HOMO$-$1 as observed in 2PPE at the respective energies. From the peak intensities at the different spots, it becomes clear that the HOMO is more localized at the Br substituents than the HOMO$-$1.

The electronic structure of DBBA adsorbed on Au(111) is summarized in Fig. 3.10. Besides two IPS, we find a total of five electronic states assigned to

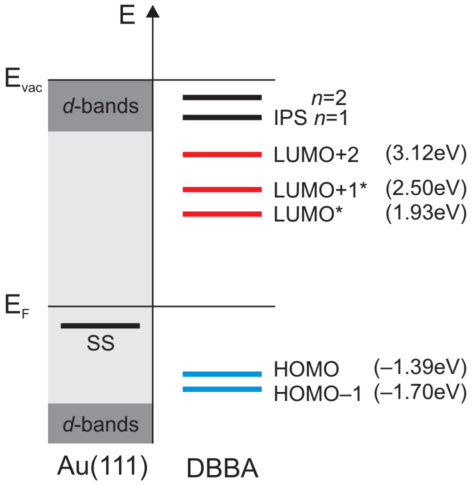

Figure 3.10: Overview over the electronic states observed in the first monolayer of DBBA/Au(111). We find five molecule-induced states as well as two IPS. *The two lowest unoccupied molecular orbitals could only be observed in STS (measurement by Bo Chen in the group of Prof. Franke, Freie Universität Berlin).

molecular orbitals, three unoccupied and two occupied. The findings in this section furthermore suggest that Br is still attached to the DBBA molecule upon adsorption on the Au(111) surface at 300 K, which suggests that dehalogenation occurs at higher temperatures.

3.2.2 Following the Thermal On-Surface Synthesis with TPD

Based on the knowledge of the monomer phase in the preceding section, we will now examine the thermally induced on-surface reaction using temperature-programmed desorption (TPD). Observing the desorbing species in a QMS while increasing the sample temperature in a controlled way, i.e. with a linear ramp of rate β, we have the opportunity to follow the thermal reaction in its various stages.

Before investigating different masses, let us first consider the desorption behavior of the molecular backbone, represented by the anthracene biradical $C_{28}H_{16}^{2+}$ which is detected at a mass of 176 amu. Fig. 3.11a shows TPD of DBBA layers of varying thickness adsorbed on Au(111). The initial coverage was controlled via the evaporation time. The sample temperature during deposition was 300 K. The most intense feature is a zero-order desorption peak α_1 with an onset at around 340 K. This peak does not saturate with increasing initial coverage and is hence assigned to the multilayer. The remaining two features α_2 and α_3 both saturate. While α_2 has a peak shape typical for zero-order desorption as well, the intensity of α_3 is quite low so that we can not identify the desorption order from the peak shape. As we have seen in sect. 3.1.2, the DBBA molecules start diffusing on the surface at elevated temperatures and subsequently couple, forming the polyanthrylene polymer at

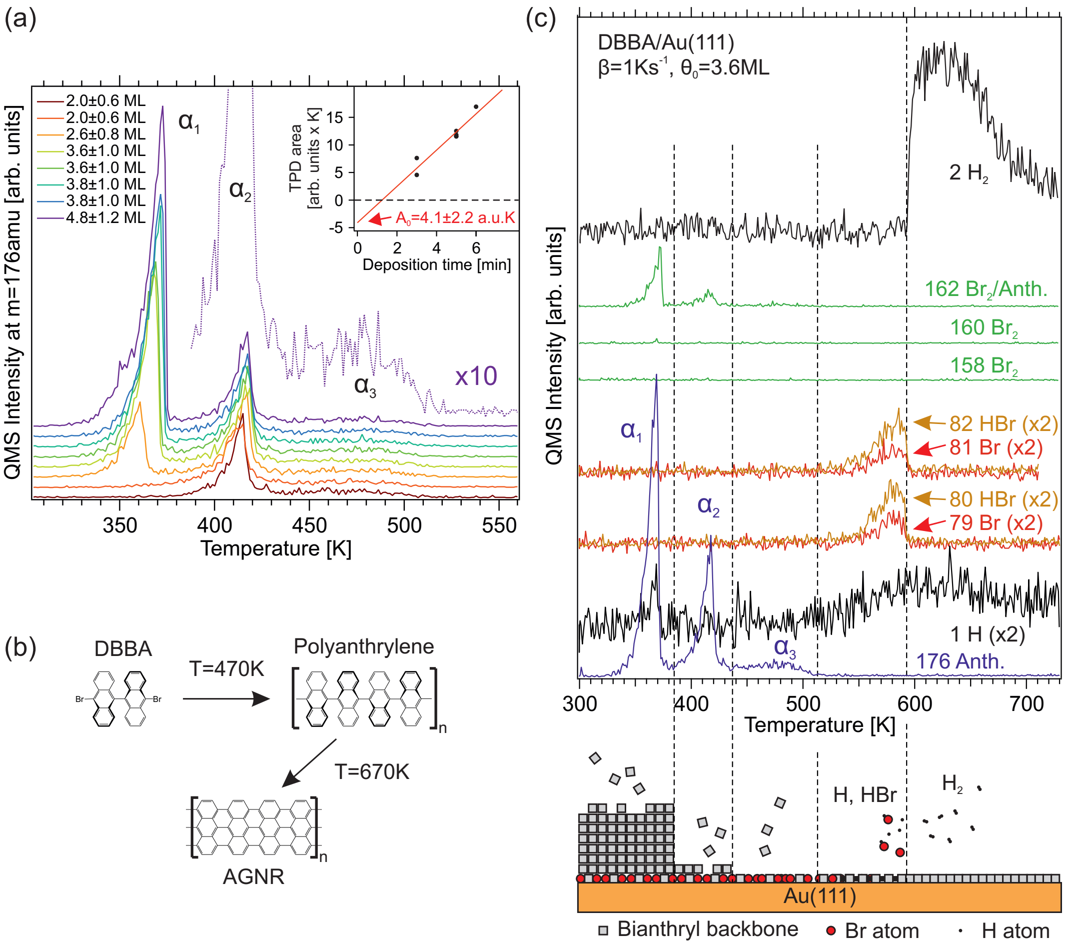

Figure 3.11: (a) TPD curves for various initial coverages of DBBA on Au(111) recorded at a fragment mass of 176 amu ($C_{28}H_{16}^{2+}$) and with a heating rate of $\beta = 1$ Ks^{-1}. Three desorption peaks are observed: α_3 and α_2 saturate and are assigned to the first and second layer, respectively, while α_1 arises from the multilayer. The TPD at highest initial coverage of 4.8 ML is magnified by a factor of 10. The inset shows an extrapolation of the integrated TPD area to a vanishing deposition time, yielding an estimate for the coverage which is not desorbed, A_0. (b) Schematic depiction of the thermal synthesis reaction of the AGNR, starting from DBBA. See sect. 3.1.2 for details. (c) TPD curves of DBBA with an initial coverage of 3.6 ML for different fragment masses. Besides the desorption features α_{1-3} of anthracene (Anth.) at 176 amu, we also follow the desorption of Br, HBr, H, H_2 and Br_2. The corresponding masses are noted in the figure and some traces have been magnified as indicated at the respective labels. Below the figure, a schematic depiction of the processes at different temperatures is shown. A linear background was subtracted from all TPD.

a temperature of around 470 K (see Fig. 3.11b) [77]. Therefore, not all DBBA molecules desorb thermally and hence, not all the adsorbed DBBA molecules contribute to the TPD signal. The low intensity of α_3 and its abrupt cut-off show that at around 500 K, diffusion and covalent coupling becomes dominant over desorption. Beyond this temperature, no signal of anthracene desorption is observed anymore.

The TPD area is proportional to the amount of desorbing molecules. The initial coverage, in units of monolayers, can be determined by referencing it to the area of a TPD of a single adsorbate layer. In the present case, the features α_2 and α_3 both saturate which might have different reasons: (i) either both features arise from the same layer; an occurrence of multiple desorption features within the first adsorbate layer may be due to a compressed layer [116, 175, 106] or desorption from defects [176]. (ii) On the other hand, the formation of a bilayer can also lead to a distinct, saturating desorption peak of the second layer [177, 176, 178]. Depending on the scenario, the TPD areas have to be normalized (i) by the area of both, A_2+A_3, or (ii) by the area of only one, $A_2 \approx A_3$, features, respectively. In order to gauge the coverage, it is necessary to estimate the amount of polymerizing precursors which is done here by extrapolation of the TPD area to the limit of a vanishing evaporation time (see inset of Fig. 3.11a), A_0. The amount of molecules adsorbed in the phase corresponding to α_3 can then be estimated by adding $A_0 = 4.1 \pm 2.2$ arb. units $\times$ K to the peak area of α_3, which yields $A_3 = 5.4 \pm 2.5$ arb. units $\times$ K. For comparison, the peak area of α_2 amounts to $A_2 = 3.4 \pm 0.5$ arb. units $\times$ K. Although the areas of both saturating phases are thus of comparable size, the large error which results from the above extrapolation makes it difficult to distinguish bilayer formation or a monolayer composed from two phases. Nevertheless, because the two values A_2 and A_3 are similar, we will henceforth assume bilayer growth and reference the TPD areas (corrected by A_0) to the average of the two peak areas, $\frac{1}{2}(A_2 + A_3)$. α_2 is thus interpreted as originating from the second layer.

Let us now turn to the desorption of species other than the one at 176 amu, the TPD for which are shown in Fig. 3.11c. Br occurs in two almost equally common isotopes, ^{79}Br and ^{81}Br. When we consider the respective desorption traces which have been recorded after preparation of 3.6 ML, we find that no Br signal can be observed in the temperature window where desorption from the second and higher layers is observed. Furthermore, Br does also not desorb in its molecular form, Br_2, as evident by the traces of 158 amu and 160 amu. Note, that the signal at 162 amu is due to an anthracene fragment with the same mass ($C_{13}H_6^+$). At higher temperatures, desorption of Br-containing species is observed which demonstrates that Br is transferred to the sample (from the evaporator) during sample preparation. The fact that the traces at 79 amu and 81 amu exhibit identical behavior and have equal intensity, clearly links these fragments to Br. The area of these Br desorption peaks is independent of the initially deposited DBBA coverage (of more than one monolayer), which excludes a possible dehalogenation in the multilayer that is followed by diffusion of the halogen atoms to the surface. In summary, we observe that there is no Br present in the multilayer in any form. This surprising result may be explained by (i) dehalogenation of DBBA during evaporation. However, Br is attached to the precursors upon adsorption in the first monolayer (see sect. 3.2.1) which in this case would suggest a recombination of the bianthryl and the Br radicals on the surface. The second possibility is (ii) a dehalogenation of DBBA after adsorption in the multilayer phase. The necessary dissociation energy (3.85 eV in the free molecule [158]) would have to be compensated by another, exothermic reaction in the multilayer phase. Associative desorption of Br_2 can be ruled out based on the TPD presented here. Another possible explanation is polymerization in the multilayer. In the monolayer, this process is highly exothermic [158] and might be able to provide enough energy for dehalogenation. However, the present data are not suited to prove this hypothesis and we would like to point out that polymerization in the multilayer is merely a possibility.

At around 550 K, desorption of both Br isotopes demonstrate clearly, that Br is present on the surface even after the polymerization reaction. Therefore, an involvement of Br in the cyclodehydrogenation reaction can not be completely ruled out. Simultaneously, we can observe desorption of HBr (again, for both Br isotopes). The intensity of the HBr signal is higher than that of Br and both species show exactly the same desorption behavior which indicates that the observed Br is merely a fragment of HBr in the QMS measurement process. The observation of a slight increase of the H signal (despite its high noise level) is also consistent with an associative desorption reaction.

$$\mathrm{H}\cdot + \mathrm{Br}\cdot \rightarrow \mathrm{HBr}\uparrow \tag{3.1}$$

Such hydrogen-driven halogen desorption processes have been known to occur at semiconductor surfaces [179, 180, 181]. Several other possible reaction pathways exist which lead to removal of the halogen from the surface. While the formation of Br_2 is energetically not favored at the surface [158], desorption of halogen atoms [182] or metal–halogen dimers [183] have been observed for similar systems. Nevertheless, associative desorption of HBr is the only process which we observe in this temperature range. While isolated Br is available on the surface after the polymerization step, the only source of H which is necessary for the formation of the desorbing HBr, are the polyanthrylene chains. During the cyclodehydrogenation reaction, atomic hydrogen is released which is known to be stable in this atomic form on Au surfaces [184, 185, 140]. At the respective temperature of more than 500 K, both Br (diffusion barrier of Br on Au(111): 90 meV [158]) and H are likely to diffuse easily on the surface or be absorbed in one of the first sub-surface layers [186]. Both species are therefore available for potential on-surface chemical reactions. Since the cyclodehydrogenation is thus the bottleneck for desorption of HBr, we can directly observe that this process is initiated between 550 K and 600 K. We note, that Br is at least closely related to the cyclodehydrogenation process and possibly catalyzes this process by lowering the barrier for H dissociation from the anthrylene units.

At 600 K, the desorption of Br and HBr suddenly ceases and a sharp increase of the H_2 signal is observed. It is most likely that this species is formed by an associative desorption reaction as well, in line with similar reactions on other surfaces [185, 187].

$$\mathrm{H} \cdot + \mathrm{H} \cdot \rightarrow \mathrm{H}_2 \uparrow \tag{3.2}$$

If both reaction channels 3.1 and 3.2 occurred independently, two desorption peaks would be expected, generally at different desorption temperatures due to the different desorption barriers for HBr and H_2 on Au(111). The sharp transition between the HBr and H_2 signals, respectively, on the other hand suggests that the desorption of the latter species is inhibited at lower temperatures. Since eight times more H atoms than Br atoms are released in the on-surface synthesis reaction of DBBA, we ascribe this inhibition to the presence of Br which ends abruptly upon consumption of all available Br atoms. For example, the HBr formation on the surface could be more efficient than the production of H_2 or in the presence of Br, another reaction,

$$\mathrm{H}_2 + 2\mathrm{Br} \cdot \rightarrow 2\mathrm{HBr} \uparrow, \tag{3.3}$$

could cause the inhibition of H_2 desorption, if it is more efficient than the desorption of H_2 itself. In order to discriminate between these two possibilities, further experiments will be conducted in which we will co-adsorb molecular hydrogen in the polymer phase. If reaction 3.3 does indeed occur, Br should be completely removed from the surface and should not occur in a subsequent TPD experiment. Furthermore, if Br can be removed in this way, conclusions on a possible catalytic effect on the cyclodehydrogenation process could be drawn.

Using TPD, we are able to follow the on-surface synthesis reaction as it happens, in contrast to *a posteriori* measurements which have been conducted previously, e.g. with STM. In summary, we find that Br is not present in the multilayer of DBBA on Au(111) which could be due to a polymerization reaction in this phase. In the monolayer on the other hand, Br can still be found after the polymerization reaction and is removed by associative desorption with the H released in the cyclodehydrogenation reaction. This desorption process furthermore competes with the desorption of molecular hydrogen.

3.2.3 Electronic Structure of the Intermediate Polyanthrylene: Valence and Conduction Band

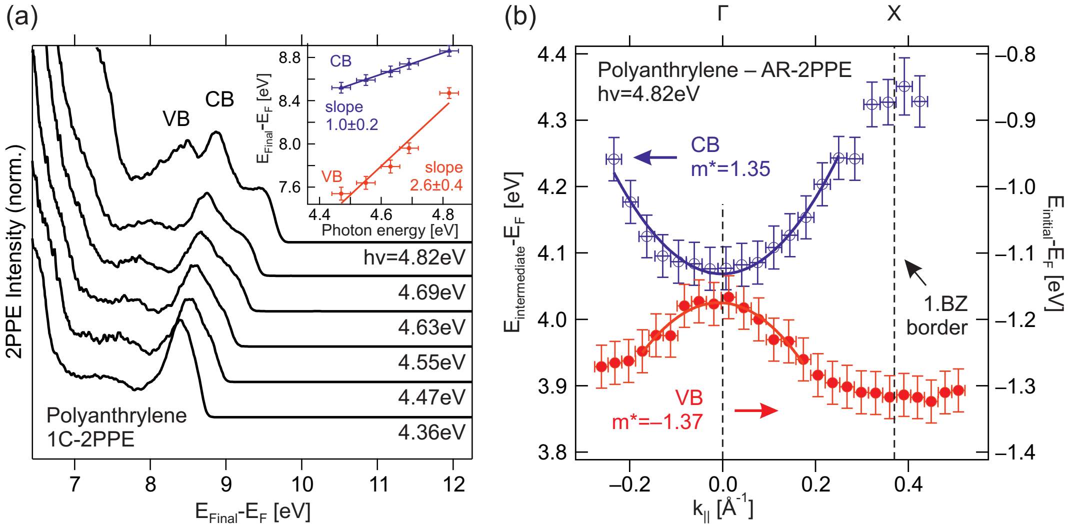

Figure 3.12: (a) 1C-2PPE spectra of the polyanthrylene on Au(111) recorded with varying photon energy $h\nu$. The spectra have been normalized to one of the d-band features (not visible in the figure). The peak shift of the VB and the CB with $h\nu$ are shown in the inset. (b) Dispersion of VB and CB as observed in AR-2PPE and shown as initial and intermediate state energy, respectively. Around the Γ-point, a parabolic fit yields the effective charge carrier masses. The border of the first Brillouin zone is marked. Both figures are published in ref. [188].

Having investigated the occupied and unoccupied molecular orbitals of the monomers in sect. 3.2.1, we will now discuss the electronic structure of the polyanthrylene chains which are an intermediate reaction product in the thermal on-surface synthesis of the AGNR and are obtained after heating a multilayer film of DBBA to 470 K for 10 min. The polyanthrylene was characterized using high-resolution electron-energy loss spectroscopy (HREELS) in our group (conducted by F. Leyssner, S. Stremlau) [189, 190, 191], confirming the three-dimensional structure found in STM by Cai *et al.* [77]. The results presented in this section have been published in *J. Chem. Phys.* **140**, 024701 (2014) [188].

Fig. 3.12a shows a series of 1C-2PPE spectra recorded with different photon energies. Besides the two prominent peaks associated with the d-bands of Au (see sect. 3.2.1) we find two peaks induced by the polyanthrylene which we assign to the valence band (VB) and the conduction band (CB), respectively, due to their dispersion which is discussed below. The final state energy shift of both features is shown in the inset of Fig. 3.12a. The CB peak exhibits a shift with a slope of 1.0 ± 0.2 and is therefore assigned to an unoccupied state at 4.07 ± 0.04 eV above the Fermi level. The VB peak on the other hand shifts with a slope of 2.6 ± 0.4 which allows identification of the corresponding state as being occupied, with a binding energy of -1.18 ± 0.04 eV relative to the Fermi level. The fact that the slope is larger than two is due to a partly resonant excitation via the CB in the spectrum recorded with a photon energy of 4.82 eV. From the energies of both bands we calculate a band gap of 5.25 ± 0.06 eV. The low energy cutoff of the 2PPE spectra yields a work function of the polyanthrylene-covered surface of 4.81 ± 0.01 eV.

The dispersion of the observed electronic states which is a measure for the degree of charge carrier localization or delocalization, has been investigated in angle-resolved 2PPE experiments, the results of which are shown in Fig. 3.12b. Around the Γ-point of the one-dimensional Brillouin zone, the CB disperses in the same fashion as a quasi-free electron, i.e. the band energy rises parabolically with increasing momentum $k_{\|}$ which is reflected in a positive effective mass m^*. A fit according to eq. 2.4 yields $m^* = 1.35 \pm 0.07$. Similarly, the VB shows a hole-like dispersion with an effective mass of $m^* = -1.37 \pm 0.15$. Note, that both bands have the same absolute value of the effective mass. At a momentum parallel to the surface which approaches the X-point, i.e. the border of the first Brillouin zone, the dispersion of both bands deviates from the parabolic behavior and in the region of the X-point, the bands become flat. It is noteworthy that the present polyanthrylene polymer exhibits dispersing bands at all since the single anthrylene units are only connected by a σ bond.

In order to be able to put these experimental results into the context of the entire band structure and in order to understand the very formation of electronic bands in this system which is not fully aromatic, DFT calculations of the electronic structure for both finite and infinite polyanthrylene polymers in vacuum were performed by M. Utecht in the group of Prof. Saalfrank (Universität Potsdam) [192]. These calculation were done using both the PBE0 [193] functional which implements the general gradient approximation (GGA) and the CAM-B3LYP functional [194] which is particularly suited for long-chain molecular systems (see ref. [188] for more details) and it was found that for the polyanthrylene, CAM-B3LYP delivers results which are in much better agreement with experiments than those obtained using PBE0.

Without the presence of the substrate, i.e. for a free polyanthrylene in vacuum, the angle between two adjacent anthracene units would be 90°. Due to the attractive van der Waals interaction between the metal substrate with its high polarizability and the aromatic system of the anthracene units, this

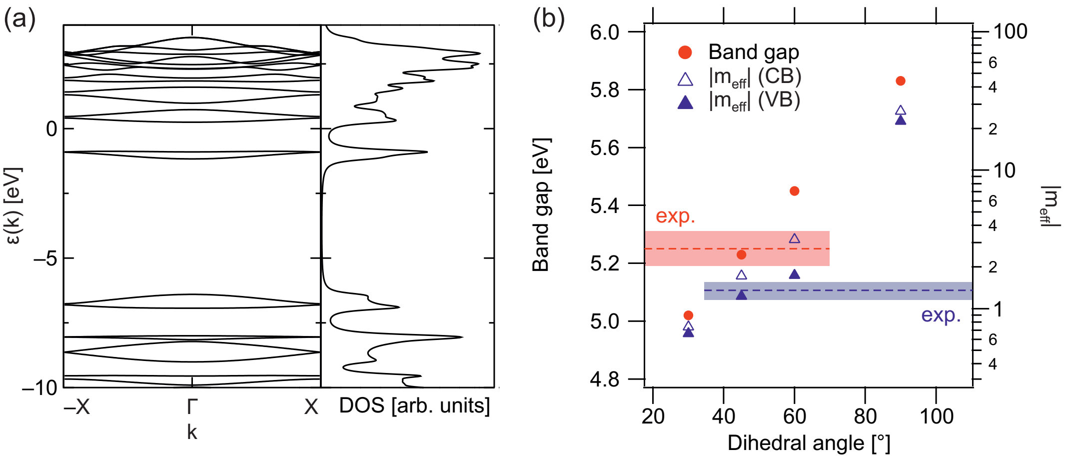

Figure 3.13: Calculations on the electronic properties of the polyanthrylene performed in the group of Prof. Saalfrank (Universität Potsdam). (a) Calculated dispersion and density of states of an infinite polyanthrylene with a dihedral angle of 45° using the CAM-B3LYP functional. The X-point corresponds to 0.36 $Å^{-1}$. (b) Calculated band gap and effective mass of the VB and CB for varying dihedral angles and periodic boundary conditions using CAM-B3LYP. The experimentally determined values are shown as dashed lines and the shaded area marks the respective error. Both figures published in ref. [188].

dihedral angle can be expected to be reduced on the Au(111) surface in the sense that the entire structure is closer to the surface than it would be the case for the polyanthrylene in its gas phase geometry. Unfortunately, to the author's knowledge, a value for this dihedral angle has not been published so far in the literature. DFT calculations in this section were therefore performed for different dihedral angles. Besides affecting the geometry of the adsorbed polyanthrylene, the metallic surface can also be expected to have an influence on the electronic structure, e.g. due to substrate polarization, which has been found to substantially decrease the band gap for the AGNR [163].

Fig. 3.13a shows the calculated band structure of an infinite polyanthrylene using CAM-B3LYP and, exemplarily, a dihedral angle of 45°. In agreement with the experiment shown above, a direct band gap of 5.23 eV is found at the Γ-point and the effective mass of the CB is calculated as 1.72, whereas the VB disperses with an effective mass of −1.23. The sign of the effective masses are the same as in the above experiments for both the VB and the CB. Other calculations which have been conducted for finite polyanthrylene oligomers with two, four and six anthrylene units do not differ qualitatively and even the size of the band gap remains around 5 eV, independent of oligomer length.

A variation of the dihedral angle in the DFT calculations has a substantial influence on the electronic structure (see Fig. 3.13b). The band gap increases linearly with increasing dihedral angle and simultaneously, the absolute value of the effective masses of both the VB and the CB rise exponentially. At a dihedral angle of 45°, the calculated parameters of the band structure fit quite well to the experimental values. However, one should be careful when comparing the measurements with calculations performed for the free polyanthrylene in vacuum due to the considerable influence of the substrate on the electronic structure. Particularly, it is not possible to determine the dihedral angle of the adsorbed polyanthrylene from these band gap calculations.

In this section we made the noteworthy observation that the polyanthrylene, the intermediate of the thermal AGNR synthesis, exhibits dispersing bands with a direct band gap of 5.25 eV, which is rather large. The observed effective masses around the Γ-point are relatively large which we attribute to the fact that the electronic system is not fully conjugated over the entire polymer structure. Instead, the aromatic electronic system of the individual anthracene units is restricted to these units. It is interesting to note that the effective mass decreases as the dihedral angle decreases, i.e. when the polyanthrylene assumes a more planar configuration and the π-systems of adjacent anthracene units can be expected to overlap partially, leading to increased charge carrier mobility along the polymer chain.

3.2.4 Electronic Structure of the AGNR: Band Gap, IPS and Edge State

Starting from the polyanthrylene discussed in the previous section, the AGNR can be produced by annealing the sample at 670 K for 10 min. This preparation procedure is identical to the one described by Cai *et al.* [77] and it is thus reasonable to assume that we have obtained the same AGNR structure on the Au(111) surface. Furthermore, the AGNR phase was characterized using HREELS in our group (conducted by F. Leyssner, S. Stremlau) [189, 190, 191]. Xe co-adsorption and desorption experiments allow a rough estimate of the AGNR coverage on the surface which is determined to be around 2/3 of a monolayer (see appendix A). The results presented in this section have partly been published in *Phys. Rev. B* **86**, 085444 (2012) [191].

After thermal fabrication of the AGNR we used 1C-2PPE to investigate the electronic structure. Fig. 3.14a shows a photon energy dependent series. The work function of the sample was 4.88 eV. Besides the prominent peaks arising from the d-bands, three additional features can be found in the spectra. Based on its peak shift with the photon energy (slope 0.9 ± 0.1, see inset of Fig. 3.14a), the peak labeled CB is assigned to an unoccupied electronic state with an energy of 1.44 ± 0.06 eV relative to the Fermi level. We identify this lowest unoccupied electronic state as the conduction band of the AGNR. In

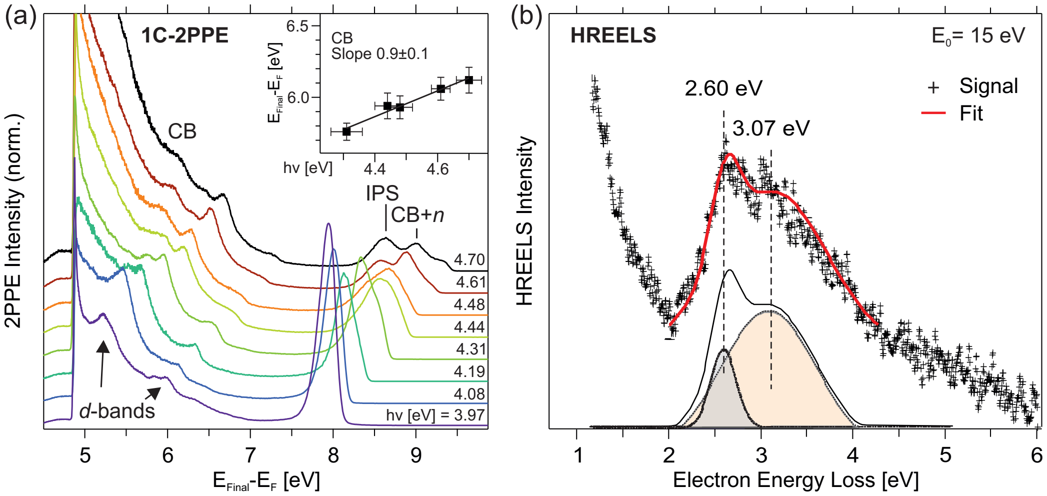

Figure 3.14: (a) 1C-2PPE spectra of the AGNR/Au(111) for varying photon energies $h\nu$. The spectra have been normalized to one of the d-band features. Besides the Au features, three peaks are observable. The inset shows the peak shift of the CB with varying $h\nu$. (b) HREELS measurement conducted by F. Leyssner and S. Stremlau in our work group. The spectrum has been fitted with two Gaussian peak profiles. E_0 is the energy of the primary electrons. Adapted from ref. [191].

more recent experimental studies conducted after those presented here, values of 1.6 eV (STS) [163, 13] or 1.9 eV (inverse photoemission) [160] have been found for the position of the CB (see Tab. 3.1).

The peaks labeled IPS and CB+n can be clearly separated only in the spectra with the highest photon energies. Nevertheless we can rule out that these states arise from an occupied electronic state because in this case, the peak position relative to the Fermi edge should be independent of the photon energy. Furthermore, we can find both peaks with the same relative intensity and width in 2C-2PPE spectra and can thus rule them out to be final states with an energetic position above the vacuum level (see appendix B). Therefore both peaks can be assigned to unoccupied electronic states lying at 3.92 ± 0.06 eV (IPS) and 4.30 ± 0.06 eV (CB+n), respectively, relative to the Fermi level. The energetic difference of the peak labeled IPS to the vacuum level is 960 meV but since 2PPE is an averaging technique and since the local work function in the vicinity of the AGNR is lower (as will be discussed below), the binding energy of this state with respect to the local vacuum level has a smaller value. Furthermore, this peak shows a dispersion with an effective mass of $m^* = 1.2 \pm 0.2$ as shown in Fig. 3.15c and as we will see below, it is pinned to the vacuum level. We can thus assign the corresponding state to the image potential state (IPS) of the AGNR-covered surface. As we have already discussed in sect. 3.2.1, IPS are quite common in 2PPE spectra of adsorbate-covered metal surfaces. Unlike the IPS, the state labeled CB+n does not show a dispersion and it behaves differently compared to the IPS upon co-adsorption of Xe. We therefore assign it to a higher lying unoccupied band of the GNR with a high effective mass.

Complementary to the 2PPE experiments, HREELS experiments with a primary electron energy of $E_0 = 15$ eV have been performed in our group (F. Leyssner, S. Stremlau) [189, 190]. The primary electrons can induce electronic transitions in the sample which can be detected as an energy loss of the scattered electrons. Fig. 3.14b shows that for the AGNR on Au(111), two transitions can be observed at 2.60 ± 0.06 eV and 3.07 ± 0.06 eV, respectively. We can directly read the band gap of the AGNR from the first transition energy. This value is comparable to those obtained in the above mentioned, more recent studies, namely 2.3 to 2.8 eV [163, 13, 160]. Based on these transition energies, we can calculate the energy of the valence band maximum, which lies at -1.16 ± 0.08 eV and the position of the band below the valence band (VB$-$1) which is -1.63 ± 0.08 eV. The VB maximum determined here compares to positions determined in other studies, which lie between -0.7 eV and -1.1 eV which are generally slightly closer to the Fermi level (see Tab. 3.1) [163, 13, 160]. Based on the experimentally determined band gap we can evaluate the gaps predicted by theory (see Tab. 3.1). The fact that DFT gives a relatively good result can be interpreted as the compensation of an underestimated band gap and the missing corrections necessary to account for the presence of the substrate. In contrast, the GW approach does not show such an underestimation of the gap and by taking the substrate into account though image-charge corrections, the experimental value can be reproduced very well.

More information on the observed electronic states (bands) can be obtained in angle-resolved 1C-2PPE. Fig. 3.15a shows a series of spectra recorded for the AGNR on the Au(111) surface, where the AGNR are oriented isotropically (as shown in the inset). As mentioned before, the IPS shows a dispersion typical for such states with an effective mass of $m^* = 1.2 \pm 0.2$ whereas both the CB and CB+n are localized or have a high effective mass (see Fig. 3.15b,c). For the isotropically oriented AGNR on Au(111), one must consider that the measured momentum parallel to the surface, $k_\parallel$, of a photo-emitted electron has two components, namely a component along the AGNR axis, $k_\parallel^\parallel$, and one perpendicular to it (and parallel to the surface), $k_\parallel^\perp$. The momentum measured in the experiment is therefore larger than the momentum along the ribbon axis,

$$k_\parallel = \sqrt{k_\parallel^{\perp 2} + k_\parallel^{\parallel 2}} > k_\parallel^\parallel. \tag{3.4}$$

The isotropy therefore leads to a smearing of the dispersion behavior toward

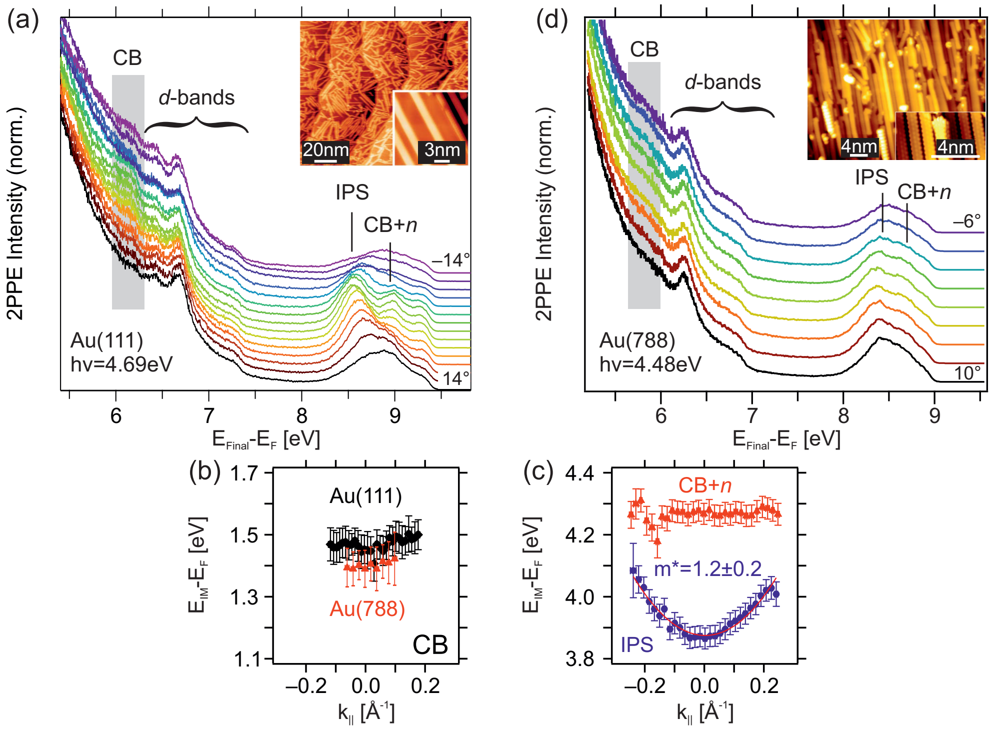

Figure 3.15: (a) Angle-resolved 1C-2PPE experiment of the AGNR on Au(111). The spectra have been normalized to one of the d-band peaks. Adapted from ref. [191]. The inset shows an STM image of the isotropically oriented AGNR, see Fig. 3.6e (adopted from ref. [77]). (b) Dispersion of the CB on Au(111) (black diamonds) and Au(788) (red triangles). (c) Dispersion of IPS and CB+n on Au(111), based on the series shown in (a). A parabolic fit yielding m^* is shown. (b) and (c) are adapted from ref. [191]. (d) Angle-resolved 1C-2PPE measurement of the AGNR on Au(788), measured along the step edges. The spectra have been normalized to one of the d-band features. The inset shows AGNR aligned with the Au(788) step edges (adopted from ref. [160]).

higher $k_{||}$ and thus an overestimation of the effective mass, but the measured energy of the band bottom is correct. See ref. [191] for further details. The intensity of the CB peak is asymmetric with respect to the sign of the emission angle, i.e. the peak intensity is higher at negative angles which corresponds to a situation in which the sample is rotated toward the p-polarized laser beam and thus the electric field vector component of the laser field in the surface plane is increased while its component perpendicular to the surface is reduced. Therefore the transition dipole moment for an electronic transition from the occupied d-bands into the CB of the AGNR lies parallel to the surface.

The isotropic alignment of the AGNR on the surface has been suspected frequently as the source of an experimental artifact which dissembles a high degree of electron localization. It has been shown that the AGNR can be produced on a stepped Au(788) surface and that the AGNR are aligned along the direction of the steps [160]. We therefore repeated the angle-resolved 2PPE experiment on the Au(788) surface. The TPDs recorded for characterization show only small quantitative differences from the very peculiar behavior of the Br, HBr, H_2 and anthracene-related traces shown in sect. 3.2.2. Fig. 3.15d shows a corresponding experiment where a relatively weak signal is observed from the CB at slightly lower energies. Both the enhanced intensity at negative polar angles and the missing dispersion behavior (see analysis in Fig. 3.15b) are consistent with the measurement on the Au(111) surface and we can thus rule out the isotropic orientation of AGNR on this crystal face to cause a false dispersion measurement. Instead we find that the CB of the AGNR on both Au faces is indeed localized.

The fact that the CB does not show a dispersion is rather surprising since electron masses on the order of $m^* = 0.01$ are usually calculated for graphene nanoribbons [55, 195]. It is conceivable that the charge carrier mobility is reduced due to the interaction with the substrate or that effective masses of GNR are generally not as low as expected from theory (the author is not aware of any other measurement that demonstrates a strong dispersion of GNR bands).

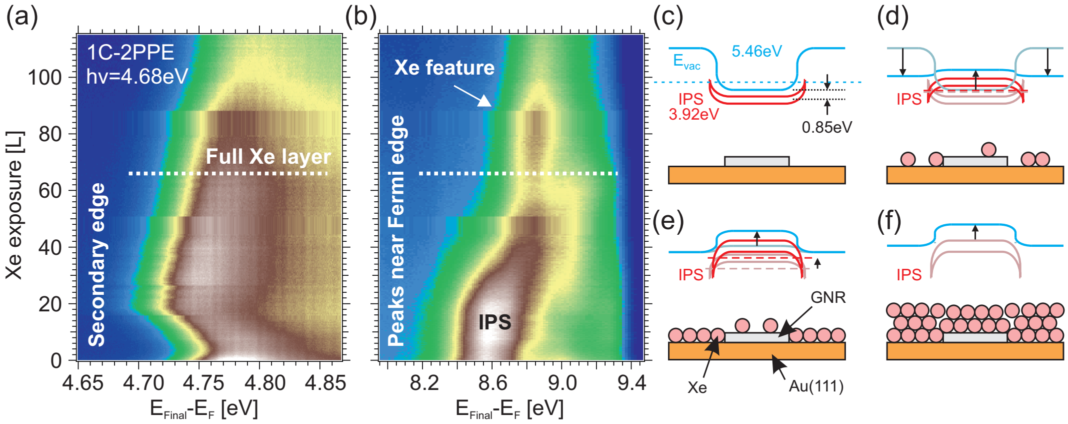

Figure 3.16: (a,b) 1C-2PPE spectra recorded continuously during exposure of the sample to Xe (T = 41 K). The color code indicates signal intensity (blue: low, white: high). (a) shows the spectral region around the secondary edge while (b) shows the region around the Fermi edge which contains the IPS and the CB+n peaks. The two plots are based on the same data. (c-f) Model explaining the changes of the work function and the IPS with increasing Xe exposure. (c) Before Xe dosage. (d) In the region between 0 and 20 L. (e) Between 20 and 65 L. (f) For more than 65 L.

Having discussed the dispersion of the three observed unoccupied electronic states, we now turn to a detailed discussion of the IPS. Generally, IPS are eigenstates of the stationary Schrödinger equation which describes a two-dimensional electron gas in the surface–vacuum potential $V(z)$ which depends inversely on the electron–surface distance z (see e.g. ref. [196]).

$$V(z) = E_{\mathrm{Vac}} - \frac{e^2}{4\pi\epsilon_0}\frac{1}{4z} \tag{3.5}$$

It becomes clear from eq. 3.5 that these eigenstates are bound with respect to the vacuum level E_{Vac} [197], unlike substrate bands, interface states [198, 199, 200, 166] or molecular orbitals which are bound with respect to the Fermi level. Adsorption of Xe has been known to alter the work function of metal substrates [201, 202, 203] and at the same time, the electronic structure can be expected to be relatively unaffected by the rare gas. We thus exposed the AGNR on Au(111) to Xe which was let into the UHV chamber by a dosing valve. The IPS is then expected to shift in energy along with the work function of the sample. In a control experiment on the clean Au(111) surface (see appendix A) we noticed a Xe-induced work function decrease of 0.5 eV. The Xe overlayer thickness was characterized using TPD (mass: 132 amu) both for the clean surface and the AGNR. A characteristic desorption peak of Xe adsorbed in the first layer on Au(111) is observed and in the presence of AGNR, a second peak arises at lower temperatures (indicating lower binding energy of Xe on the graphene structure) in the regime of the first Xe layer (see appendix A). From the ratio of these two peaks we can estimate the AGNR coverage of the sample to be around 2/3 of a monolayer. Since 2PPE is an averaging technique, the measured work function is an averaged value over the whole surface but the local work function in the vicinity of the GNR is different than at bare surface areas without AGNR. The IPS which arises due to the presence of the AGNR is pinned to the local work function, not the averaged one measured in 2PPE. Nevertheless, as the vacuum level changes continuously from the value in the center of the AGNR to the value at the bare surface areas, one can expect an energetic smearing of the AGNR IPS following the change of the vacuum level (see Fig. 3.16c).

Fig. 3.16a,b shows 1C-2PPE experiments of the AGNR on Au(111) acquired continuously during dosage of Xe. The white, dashed line marks the dose at which one layer of Xe is adsorbed on the surface (on the bare areas as well as on the GNR), as determined by TPD (see appendix A). Fig 3.16a shows the work function change while Fig. 3.16b shows the region around the Fermi edge of the spectrum in which both the IPS and the less intense CB+n feature can be observed. Fig. 3.16c schematically shows the energetic position of the IPS in the vicinity of the AGNR before Xe adsorption. Three different phases of Xe adsorption and corresponding change in the electronic structure can be distinguished: (i) In the first phase, up to an exposure of around 20 L, the work function decreases by approximately 40 meV and the IPS shifts to slightly higher energies. At first sight, this behavior contradicts the expected pinning of the IPS to the vacuum level. However, as depicted in Fig. 3.16d, one has to take into account the different local work functions: while the work function of the clean areas decreases quite strongly (see appendix A), the work function change at the center of the AGNR must be toward higher values which results in only a rather small overall change of the measured work function. While the IPS generally shifts toward higher energies in the process because it is pinned to the vacuum level in the center of the AGNR, the distortion at the AGNR edges changes, which reduces the observed energetic shift. (ii) In the second phase, approximately between 20 and 65 L, the work function increases again and the IPS, too, shifts to higher energies. In TPD, the desorption peak associated with Xe adsorption on the AGNR only develops when the desorption peak of Xe/Au(111) has already reached most of its saturation intensity. This shows that the sticking coefficient of Xe on Au(111) is considerably higher than that for Xe adsorption on the AGNR, probably due to the high polarizability of Au which fosters van der Waals interaction. As a consequence, in this phase of adsorption the clean areas are now almost completely covered with Xe whereas the coverage of the AGNR still rises. Therefore, the vacuum level (and the IPS) in the center of the AGNR rises (see Fig. 3.16e). During this phase, the intensity of the IPS decreases continuously. (iii) After formation of the first Xe layer, i.e. in the multilayer regime, the work function continues to rise and so does the IPS, the intensity of which however does not dominate the 2PPE spectrum anymore. Instead, a features associated with Xe can be observed which does not shift in energy as the layer thickness increases (see Fig. 3.16f).

As for the intermediate polyanthrylene (sect. 3.2.3), DFT calculations have been performed by M. Utecht in the group of Prof. Saalfrank (Universität Potsdam) [192] for the AGNR in vacuum using the CAM-B3LYP functional. Fig. 3.17a shows the calculated density of states for an infinitely long AGNR (with periodic boundary conditions) as well as for two finite systems, namely the heptamer and the hexamer. In all three cases, an overestimated band gap of approximately 4 eV is obtained. The calculations for finite systems furthermore yield two states which are energetically close to the center of the band gap, with a small gap between them. This small gap between the two mid-gap states decreases with increasing AGNR width. The Kohn-Sham orbitals of these two states are shown in Fig. 3.17b: both states are localized predominantly at the short ends of the AGNR which has zigzag edge character. Indeed, the depicted heptamer can be seen as a very short $N = 14$ zigzag GNR which would exhibit a spin-polarized edge state localized at the zigzag edge. Thus, we name the two states unoccupied edge state (UES) and occupied edge state (OES), respectively. Consequently, these states are not observed for the

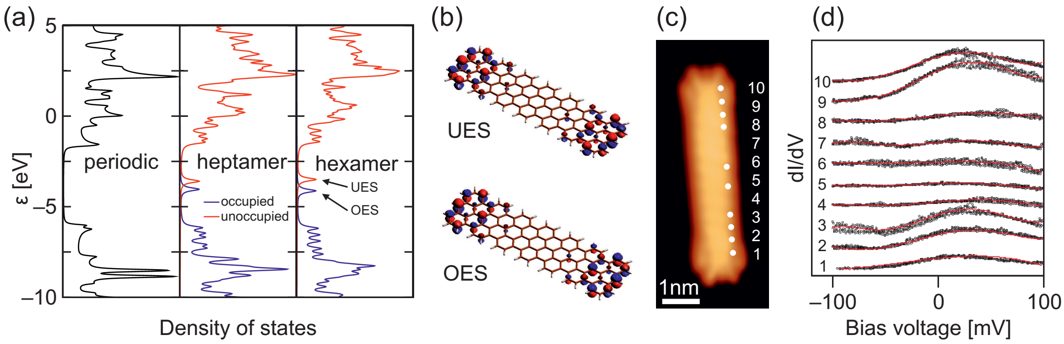

Figure 3.17: (a) Density of states calculations for the infinite AGNR with periodic boundary conditions, the heptamer and the hexamer, performed in the group of Prof. Saalfrank (Universität Potsdam) using the CAM-B3LYP functional. (b) Kohn-Sham orbitals of the OES and UES, from the same calculation as in (a). (a) and (b) published in ref. [191]. (c) STM image of an AGNR on Au(111) with characteristic finger-like lobes at both zigzag edges (ends). (d) dI/dV curves recorded at the points indicated in (c). (c) and (d) adopted from ref. [13].

infinite AGNR. Another way of describing these localized states is to interpret them as quasi-zero-dimensional surface states (Tamm states) to the bands of the quasi-one-dimensional GNR [204].

Initially, when the above experiments and calculations were interpreted, other experimental investigations of the electronic structure of the AGNR had not yet been published and based on the localization of the CB peak in angle-resolved 2PPE measurements we assigned this peak to the UES and OES which were thought to overlap due to the extended length of the GNR. This interpretation was supported by the fact that the CB lies very central between the VB and the IPS, which in turn was interpreted as the conduction band then [191]. With publication of other experimental studies [163, 13, 160, 152] it became clear that our interpretation was incorrect and that the localized state in our measurement was actually the CB whereas the edge state evidently can not be observed in 2PPE. Investigations of the AGNR with STM and STS on the other hand found a peculiar finger-like lobe structure at the zigzag edges of the AGNR [13, 152, 153], as shown in Fig. 3.17c. In the vicinity of this structure, STS shows an electronic state lying at approximately 30 meV above the Fermi level (see Fig. 3.17d) which is assigned to an edge state that is most likely due to an overlap of UES and OES. The fact that both UES and OES are observed above the Fermi level indicates a p-doping of the AGNR on the Au(111) surface. The density of states of the UES/OES feature is probably too small to be observable with our averaging 2PPE method. Furthermore, it is difficult to resolve a feature with such a low intensity directly above the Fermi level.

Figure 3.18: Comparison of the electronic structure of the intermediate polyanthrylene and the final reaction product of the thermal on-surface synthesis, the AGNR. Results labeled with (*) are based on work conducted by others, as indicated in the respective parts of this section [13, 191, 189, 190].

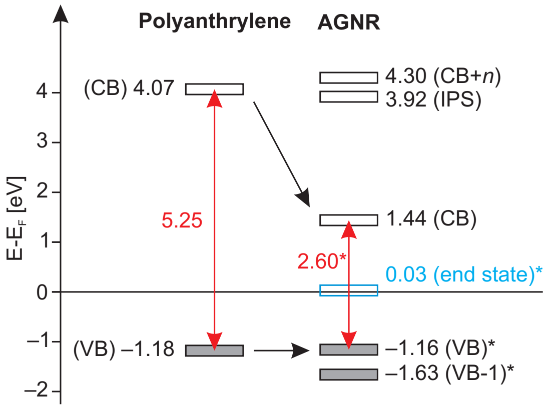

In summary, complementary surface-sensitive electron spectroscopies were used to determine the band gap and the position of the VB and CB with respect to the Fermi level, as well as an IPS and a higher lying CB+n. The band gap of 2.60 eV is comparable to other experiments conducted since and described better by GW calculations than DFT calculations which were found in the literature. The observed CB does not show a dispersion in angle-resolved experiments (not even on the stepped Au(788) surface) which is quite unexpected and most likely due to the interaction with the metallic substrate. We used Xe co-adsorption experiments to observe how the IPS of the AGNR follows the local work function. Other experiments identify an edge state predicted by calculations close to the Fermi level, which however is not found in 2PPE.

In comparison to the polyanthrylene (see Fig. 3.18), the band gap of the AGNR is reduced by about half the value of the polyanthrylene band gap. This reduction can not simply be explained by the tendency of the polyanthrylene's band gap to decrease with decreasing dihedral angle between neighboring anthracene parts (as shown in Fig. 3.13b). Instead, it is due to the fundamentally different nature of the electronic system of the AGNR which has a fully conjugated π-system. Furthermore, no edge (end) states are found in the polyanthrylene calculations at any dihedral angle which is not surprising as they, too, are a consequence of the extended aromatic system. In comparison with the polyanthrylene, the center of the band gap is shifted to lower energies by 1.4 eV, possibly due to increased hybridization of the GNR with the underlying substrate.

3.2.5 Photo-Induced Covalent Coupling of the Molecular Precursors

Bottom-up fabrication in a thermal on-surface synthesis yields atomically precise GNR with well-defined edges, chiralities and widths on the scale of nanometers, which makes it a powerful alternative to previously employed top-down fabrication techniques. Nevertheless, this approach suffers from the missing ability to limit the synthesis to a specific region of the surface, as in lithography. In order to combine the advantages of on-surface covalent self-assembly and the ability to write mesoscopic structures, a light-induced pathway toward molecular self-assembly and cyclodehydrogenation would be desirable. In this section we will thus investigate the effect of illumination on the adsorbed DBBA precursor molecules on the Au(111) surface.

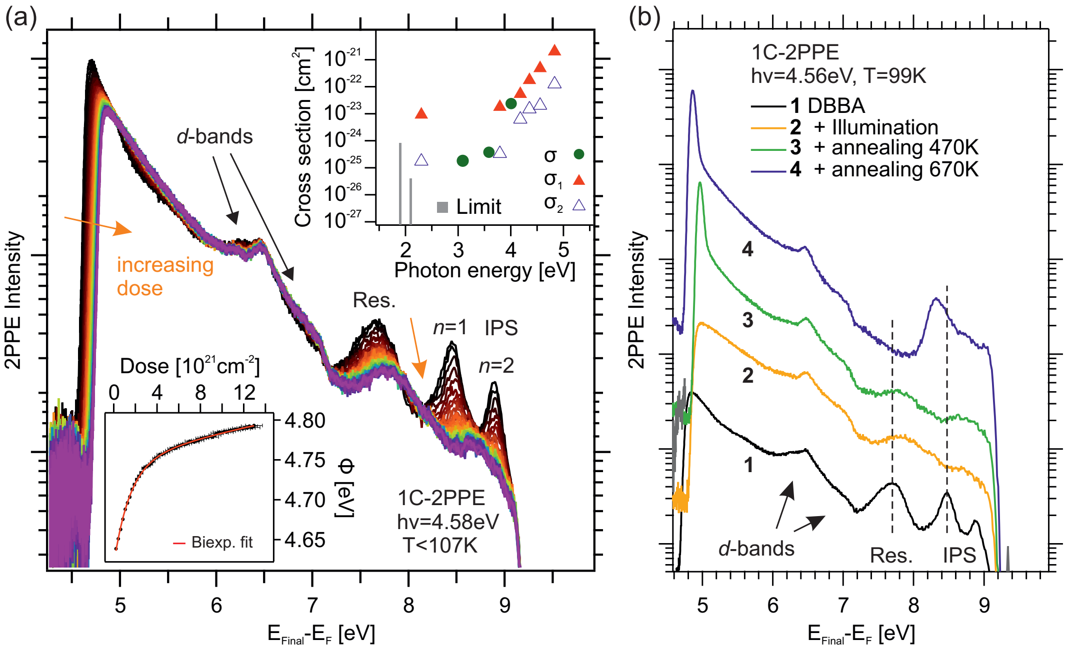

Figure 3.19: (a) Photo-induced changes in 1C-2PPE spectra of 1 ML DBBA/Au(111). The color gradient indicates increasing photon dose from black to magenta. Changes are observed for the work function, the molecular resonance (Res., see text) and the IPS. The work function Φ is depicted as a function of photon dose in the lower left inset. The upper right inset shows the cross sections or upper cross section limits for different photon energies. (b) Annealing of the photo-product. 1C-2PPE spectra are shown (1) for DBBA before illumination, (2) after illumination with a photon dose of 4.5×10^{23} cm^{-2}, (3) after subsequent annealing at 470 K and (4) further annealing at 670 K. All spectra were recorded at a sample temperature of 99 K and offset in this figure for clarity.

For the experiments described here we prepared a DBBA coverage of 1 ML as described in sect. 3.2.1. There, the DBBA phase has been studied with respect to its electronic and geometric structure. We found five molecular orbitals (three of them are unoccupied) along with two IPS. In the sub-monolayer regime, the DBBA monomers assemble in islands which consist of dimer rows in which the molecules are intertwined.

Upon illumination of this phase, we now find photo-induced changes in the 1C-2PPE spectra. Fig. 3.19a shows a series of spectra which have been acquired continuously during illumination with light in the UV regime ($h\nu = 4.58$ eV, $\lambda = 269$ nm). With increasing photon dose, drastic changes can be observed in the spectra. The work function increases by more than 100 meV, both IPS lose most of their intensity and a feature arising from a resonant excitation within the molecule, namely from the HOMO−1 and the HOMO into the LUMO+2 (labeled "Res.", see Fig. 3.10) loses intensity and is shifted to higher energies. These three molecular orbitals, which are separated in 2PPE spectra with lower photon energy, all lose intensity, as shown in appendix D.

Unlike molecular resonances or IPS, the work function of the sample is a quantity which is accessible over a wide range of photon energies in photoemission spectra. Therefore, we used it as the benchmark for the progress of the reaction in order to quantify it. The work function as a function of photon dose d is depicted exemplarily for one photon energy in the inset of Fig. 3.19a. The increase of the work function does not follow a simple exponential relation but can be well described with a bi-exponential fit function,

$$\Phi(d) = \Phi(0) + \frac{\Delta\Phi}{\gamma} \times \left[1 - e^{-\sigma_1 d} - \gamma e^{-\sigma_2 d}\right]. \tag{3.6}$$

Here, $\Delta\Phi$ is the work function change in saturation of the process, $\sigma_{1,2}$ are two cross sections and γ describes the ratio of the two components with respect to their influence on the change of the work function. This function has been fitted to the data, varying all parameters freely, and the resulting cross sections are $\sigma_1 = 6.8 \pm 0.3 \times 10^{-22}$ cm^2 and $\sigma_2 = 3.4 \pm 2.4 \times 10^{-23}$ cm^2.

We performed similar experiments for different photon energies and in most cases we observed changes in the spectra consistent with those observed in Fig. 3.19a. The resulting cross section values are shown in a logarithmic plot in the upper right inset of Fig. 3.19a. For photon energies between 3.8 eV and 4.8 eV both cross section components increase exponentially. The observed process is relatively ineffective and due to the limited photon dose that can be applied under the given conditions, only a limited cross section can be observed, which depends on the photon energy but is usually around $10^{-25\pm1}$ cm^2. In case of two photon energies in the visible regime around $h\nu = 2$ eV, no spectral changes were observed but based on the applied photon dose we can give upper limits for the cross section. In the range of 3 eV to 4 eV, three illumination experiments revealed a photon dose dependence of the work function change which could be described by a single-exponential function yielding a single cross section σ. Considering that the exponentially decreasing cross sections $\sigma_{1,2}$ are approaching the detection limit in this region, it is conceivable that the more inefficient process (described by σ_2) can not be observed anymore and that in fact $\sigma = \sigma_1$.

In light of the thermal reaction of DBBA monomers toward the AGNR, we performed annealing experiments on the photo-product of the light-induced reaction. Fig. 3.19b shows 2PPE spectra before and after illumination of DBBA as well as after two subsequent annealing steps. The effect of illumination is the same as we have observed above and the photo-product is characterized by two features between 7.5 and 9.0 eV. Upon heating this phase to 470 K for 10 min, these two features remain unchanged and at the secondary edge, a sharp and intense peak arises. The unchanged features characteristic for the photo-product indicate that it is thermally stable up to this temperature. However, the intense new feature at the secondary edge shows that some change is in fact induced by annealing, possibly an ordering effect. After a second annealing step at 670 K (10 min), drastic changes are observed both at the secondary edge and in the region close to the Fermi level. However, the spectrum differs from a comparable spectrum of the AGNR (see Fig. 3.14). Most importantly, the CB peak can not be observed in this phase. We can thus assume that the photo-product undergoes fundamental changes upon annealing at 670 K.

As for the DBBA monomers in sect. 3.2.1, the product of the photo-induced reaction has been studied with STM in order to determine its structure. The illumination in the STM setup was achieved with a portable ArF excimer laser ($\lambda = 193$ nm). The equivalence of the photo-products which are observed upon illumination with this excimer laser and with the Ti:Sapphire laser setup, respectively, was verified beforehand as shown in appendix E. The STM and STS experiments presented here have been conducted together with Bo Chen in the group of Prof. Franke (Freie Universität Berlin) [173] in the framework of a collaboration in which the author of the present thesis has contributed to the design of the experiment, the performance of the laser illuminations as well as the discussion and publication of the results [174].

An overview over the adsorbate after illumination with a photon dose of 2.0×10^{22} cm^{-2} is given in Fig. 3.20a. As in the case of DBBA, islands can be observed, which in this case however consist of ordered, lower parts and a disordered overlayer. Fig. 3.20b shows an image of a larger area without overlayer where the lower-lying structure can be analyzed. It consists of lamellar features which are aligned parallel to each other and the angle between these features and the soliton lines of the herringbone reconstruction is around 85°.

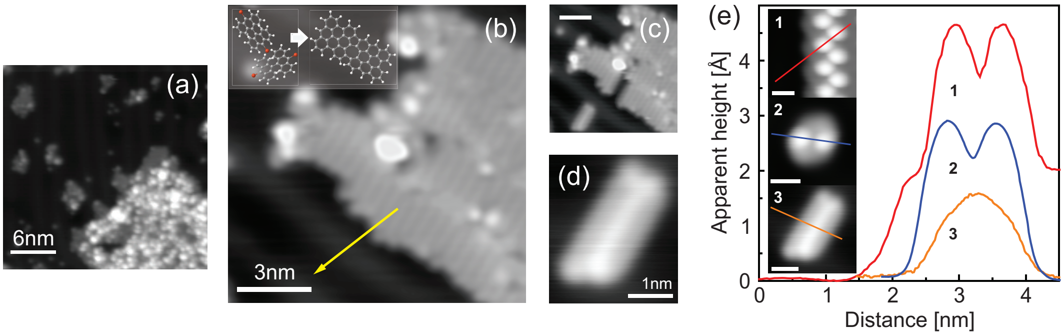

Figure 3.20: STM experiments on the photo-product of DBBA performed in collaboration with the group of Prof. Franke (Freie Universität Berlin). (a) STM overview image recorded after illumination of DBBA/Au(111) (V_S = 0.76 V, I_t = 18 pA). (b) Ordered (lower) structure observed after illumination. The arrow indicates tip-induced manipulation (V_S = 1.9 V, I_t = 19 pA). The inset shows a structure model of a DBBA dimer (before illumination) and a covalently coupled structure (after illumination). (c) Same area as in (b) after tip-induced manipulation. Scale bar: 3 nm. (d) High-resolution STM image of the photo-produced structure which was isolated from the island (V_S = 1.0 V, I_t = 0.1 nA). (e) Line profiles of (1) the edge of a DBBA island, (2) an isolated DBBA monomer and (3) the isolated photo-product. Scale bars: 1 nm.

The lamellar features are aligned in four rows perpendicular to their axes. Note, that the DBBA dimer rows before illumination are aligned along the soliton lines (see Fig. 3.9a).

Using lateral tip-induced manipulation, single units which always have the same shape and apparent height can be removed from the island (see Fig. 3.20b,c). Fig. 3.20d shows a high-resolution STM image of one of the units. Their intensity distribution is relatively homogeneous, with an elongated intensity maximum along the central axis, and they are not rectangular but rather one corner seems chipped off (in this case, the lower right one). Comparing the apparent height with that of DBBA within an (unilluminated) island and an isolated (unilluminated) DBBA molecule, we find that the photo-produced structure is considerable more flat than the twisted DBBA molecule. The area which is occupied by one photo-produced unit in the island amounts to 2.3 nm^2, which is almost identical to the unit cell of the DBBA phase. Since this unit cell contains two DBBA molecules we conclude that the photo-produced structure is composed of two DBBA molecules. To summarize the above results, we find flat, relatively homogeneous, covalently bound (as shown by the manipulation) DBBA dimer structures which have been produced by the laser.

Concerning the structure of the photo-product, different covalently bound DBBA dimers are conceivable but as we will see below, the mechanism behind this coupling reaction is non-thermal. We can thus assume that the bond formation occurs with a minimum of preceding diffusion. Considering the

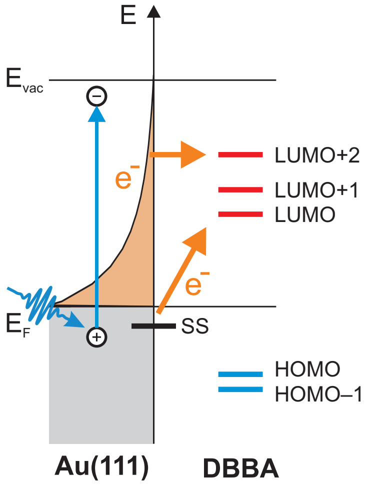

Figure 3.21: Proposed excitation mechanism for the photo-coupling reaction of DBBA. Absorption of a photon in the substrate leads to the creation of a hot electron distribution above the Fermi level (yellow area). These hot electrons can tunnel into the LUMO+2 of DBBA and cause a dehalogenation reaction. Another possible excitation pathway is a direct electronic transition from the SS to the LUMO.

relative orientation of the DBBA monomers before illumination, a threefold covalent link, probably initiated by dehalogenation, seems likely (see inset of Fig. 3.20b). The proposed dimer structure can hardly be characterized as a GNR, due to the different chiralities in the two parts of the structure and due to the resulting defect in the center. However, we can not definitely rule out other possible dimer structures. An edge state close to the Fermi level could not be observed in STS on any of the four edges.

Since the photo-produced structure is flat and covalently bound, it is very likely that it is dehalogenated and therefore does not possess the ability to form directionally coupled polymers at temperatures around 200 °C. Furthermore, we can assume that a cyclodehydrogenation has taken place in the photo-induced reaction. It is therefore clear that an AGNR can not be produced even at temperatures of around 400 °C.

Having characterized the photo-produced structure to a certain extent, let us now discuss the possible mechanisms behind the light-induced coupling reaction. Except for $h\nu = 2.3$ eV, both cross sections σ_1 and σ_2 rise exponentially with increasing photon energy (see inset in Fig. 3.19a).

The exponential cross section increase extends over a photon energy range of at least 1 eV. Such a broad excitation spectrum without sharp resonances is characteristic for a substrate-mediated process [205, 206]. Photo-induced excitation mechanisms at substrate–adsorbate interfaces are discussed in detail in sect. 4.1.3. We can rule out that the reaction is induced thermally by local heating caused by the laser because in this case a linear increase of the cross section with the deposited energy would be expected. Generally, the absorption of a photon in a metallic substrate creates hot electrons above the Fermi level and, simultaneously, hot holes in the occupied electronic bands. A reaction in the adsorbate can then be induced by charge transfer, i.e. electron transfer into an unoccupied molecular orbital or hole transfer into an occupied molecular orbital of the adsorbate. Among other effects, this can lead to bond dissociation when an electron populates an antibonding orbital or a hole populates a bonding orbital of the molecule.

Charge transfer of hot carriers into an electronic adsorbate state can only occur when the photon energy exceeds the absolute value of the binding energy of an electronic state with respect to the Fermi level. In the present system, the exponential increase of the cross sections is observed for photon energies beyond 3.08 eV. Based on the energetic positions of the observed molecular orbitals it is therefore reasonable to assume a hot electron transfer into the LUMO+2 orbital of DBBA (which lies at 3.12 eV above the Fermi level) to initiate the covalent coupling reaction, as depicted in Fig. 3.21. In this case, an increase of the excitation photon energy leads to a non-linearly increased phase space for photon absorption processes in which hot electrons are generated at energies exceeding that of the respective orbital. The resulting increase of hot electron concentration with increasing photon energy is reflected in the exponential behavior of the cross sections.

For gas-phase halo-hydrocarbons such as chlorobenzene, dissociative electron attachment (DEA) of low-energy electrons has been known to lead to a dehalogenation reaction [207]. This process occurs via DEA to the LUMO delocalized over the aromatic system (which has an antibonding π^* character) followed by coupling to a repulsive σ^* state which leads to cleavage of the C–X bond (X: halogen). On a Cu(111) surface, a dehalogenation reaction of iodobenzene has been induced by electron attachment using an STM [208]. In case of DBBA on Au(111), an anionic resonance by hot electron transfer to the LUMO (binding energy 1.93 eV) could in principle be achieved at lower excitation energies as well. However, the vibrational redistribution of the excitation energy within the molecule requires a sufficiently long lifetime of the anionic resonance. When the molecule is adsorbed on a metal, a fast de-excitation of the resonance is to be expected which might explain why the light-induced reaction can not be observed at lower photon energies.

Instead we propose that the LUMO+2 has an antibonding σ^* character with respect to the C–Br bond and that electron attachment to this orbital directly leads to a cleavage of this bond. The two different cross sections that are observed in the experiment might be due to a competing but probably less effective C–H bond dissociation which occurs analogously to the C–Br bond cleavage. Similarly, charge transfer to the polyanthrylene polymer in an STM junction has been shown to induce a dehydrogenation reaction [162]. Alternatively, the different cross sections might reflect two excitation mechanisms which both lead to a dehalogenation. Based on our experiments we can not discriminate these two possibilities.

The photo-coupling reaction can furthermore be observed at a photon energy of 2.3 eV (see inset in Fig. 3.19a). This energy corresponds exactly to the energetic difference between the surface state (SS) and the LUMO. While the SS is quenched considerably due to the presence of the adsorbate, some residual SS intensity may be sufficient for a direct excitation into the LUMO, creating an anionic resonance which can be expected to have antibonding π^* character (as discussed above). C–Br bond dissociation requires coupling of this resonance to the σ^*-type LUMO+2. In contrast to hot electron transfer into the LUMO, a resonant excitation may yield a more efficient population of this unoccupied molecular orbital and consequently a detectable cross section. This could even compensate for de-excitation of the anionic resonance by charge transfer back into the substrate.

In this section we used light to couple two DBBA molecules on the Au(111) surface, which then form a flat, covalently bound structure. This reaction is induced by light only rather than by thermal activation. A substrate-mediated excitation mechanism is found to initiate the reaction, in which electrons are transferred into unoccupied molecular orbitals of DBBA, creating anionic resonances.

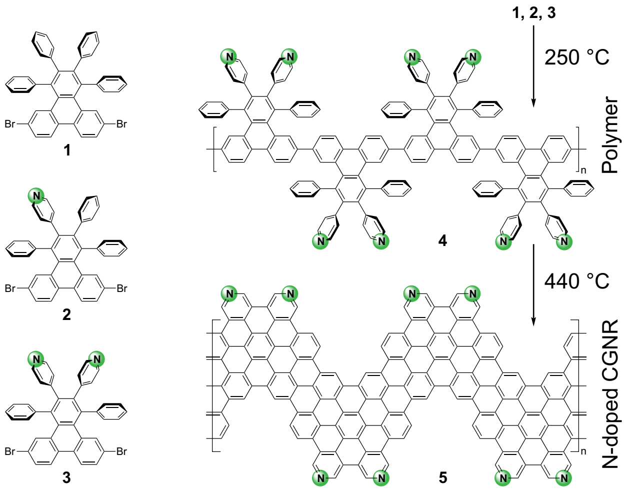

Figure 3.22: Thermal on-surface synthesis of pristine and N-doped CGNR starting from precursor molecules **1** (pristine), **2** (+N) or **3** (+2N) which were synthesized in the group of Prof. Hecht (Humboldt-Universität zu Berlin). The synthesis of a doubly doped CGNR is shown exemplarily. Annealing at 250°C yields twisted polyphenylene polymers (**4**). The final reaction product **5** is obtained after annealing at 440°C. Published in ref. [209].

3.3 Effect of Nitrogen-Doping on the Electronic Structure of Chevron-Shaped GNR

Besides the AGNR with its straight armchair edges studied in sect. 3.2, a second, chevron-shaped GNR (CGNR) has been investigated which is fabricated in a similar, thermally induced on-surface synthesis reaction as the AGNR, as described in sect. 3.1.2. In the following section we will first determine the band gap of this CGNR and explore the effect of nitrogen doping on the band gap alignment with respect to the Fermi level (sect. 3.3.1). In the subsequent section 3.3.2, the properties of the image potential state of this CGNR and the doped derivatives will be discussed.

3.3.1 n-Doping via Nitrogen-Substituted Precursor Molecules: Down-Shift of the Band Structure

In order to tailor the electronic structure of GNR with regard to applications, means to control the alignment of the electronic structure with respect to that of the surrounding materials are desirable. To that end, graphene and top-down fabricated GNR have been doped, e.g. with N atoms, which leads to an n-doping effect [64, 65, 67, 68]. Besides other shortcomings of top-down fabrication, the site of a dopant atom within the graphene lattice can not be controlled with a sufficient degree of precision although the doping site significantly influences the band gap [64, 66]. On the other hand we will see that fabrication of GNR from covalent self-assembly on surfaces not only offers the opportunity to create atomically precise structures, but also to precisely control the dopant site and concentration by substitution of the molecular precursors.

Fig. 3.22 shows the precursor 6,11-dibromo-1,2,3,4-tetraphenyl-triphenylene (**1**) as well as derivatives with one (**2**) and two (**3**) nitrogen atoms. The dopant atoms are assumed not to disturb the thermal process which yields a doped polyphenylene (**4**) at 250 °C and ultimately, after annealing at 440 °C, a doped CGNR with N atoms in pyridine-like positions (**5**). The N dopants are incorporated into the lattice being sp^2 hybridized which allows an electron to be transferred to the delocalized aromatic π-system of the GNR. This n-doping results in a down-shift of the GNR bands with respect to the electronic structure of materials with which the CGNR shares an interface.

The molecular precursors $\mathbf{1}-\mathbf{3}$ were synthesized by M. Gille *et al.* in the group of Prof. Hecht (Humboldt-Universität zu Berlin) [210]. Characterization of the adsorbed precursors, the polyanthrylene and the final CGNR as well as measurements of electronic transitions in the CGNR was performed using HREELS in our group (conducted by S. Stremlau) [190]. The results presented in this section were published in *Angew. Chem. Int. Ed.* **52**, 4422 (2013) [209].

Thermal evaporation of a sufficient amount of precursor monomers onto the Au(111) surface results in a multilayer coverage (see Tab. 2.1 for the respective evaporation temperatures). The GNR was then produced in two annealing steps at the above stated temperatures for 10 min each. TPD was used to follow the on-surface reaction via the desorption behavior of the molecular backbone as well as Br and HBr in analogy to the AGNR (see appendix F). Characterization of the different species of the reaction with vibrational HREELS confirms the reaction pathway shown in Fig. 3.22 and thereby confirms that the dopant atoms do not interfere with the thermal synthesis. Furthermore, Xe co-adsorption experiments yield a rough estimate of the coverage, namely 2/3 ML, which is the same as for the AGNR [209].

Electronic HREEL spectra after the thermal on-surface reaction of the three precursor monomers are shown in Fig. 3.23a. A single electronic transition is observed for all systems which we ascribe to a transition from the valence band (VB) to the conduction band (CB) of the respective CGNR. The energy of this transition peak corresponds directly to the band gap, namely 2.80 ± 0.03 eV in case of the pristine and the singly doped CGNR. The band gap of the doubly doped CGNR amounts to 2.71 ± 0.01 eV and is thus 3% lower. Note, that the size of the band gap is not significantly altered by doping of the precursors. Both DFT calculations and a “tight binding $+U$” (TBU) approach give a band gap of 1.5 eV for the free-standing CGNR [165]. Considering the value of 2.80 eV for the pristine CGNR in light of the fact that interaction of the AGNR with the substrate leads to a reduction of the band gap due to electronic screening effects [163], shows that this calculation for the free-standing CGNR underestimates the band gap significantly.

Figure 3.23: (a) Electronic HREELS measurements performed by S. Stremlau in our work group for the CGNR and the two doped counterparts. In all spectra, a VB–CB transition was observed and fitted with a Gaussian peak. The primary electron energy was $E_0 = 15.5$ eV and the spectra were normalized to the VB–CB transition peak. (b) Photoemission spectra of the same three systems in which the VB can be observed. The spectra were normalized to the VB peak. Both published in ref. [209].

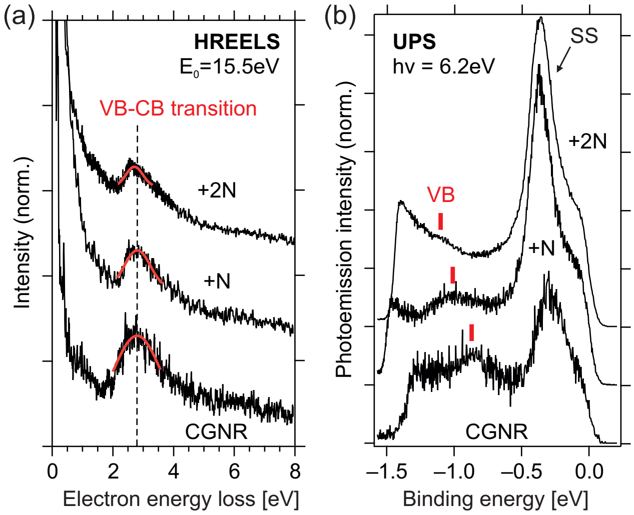

While HREELS allows direct measurement of the band gap, it does not give information about the absolute energetic positions of the bands with respect to the Fermi level. Since this alignment is of particular interest in the context of doping, we employ ultraviolet photoelectron spectroscopy (UPS) using the quadrupled fundamental beam of our Ti:Sapphire laser setup which provides laser pulses with a photon energy of 6.2 eV (see sect. 2.2). Photoemission spectra are shown for the pristine and the two doped CGNR in Fig. 3.23b. The most prominent feature in all three spectra is the surface state (SS) of Au(111) which is not completely quenched due to the CGNR coverage of less than one monolayer. Its intensity increases as the dopant concentration in the CGNR is increased. Considering that the thermal on-surface synthesis reaction was performed in an identical manner for all three systems, the increasing intensity of the surface state points toward a decreasing coverage, possibly due to repulsive interaction of the electronegative N atoms, making precursor desorption more likely and covalent coupling less likely during annealing of the sample. At lower energy (higher binding energy), a second peak can be observed for all three systems which shifts to lower energies with increasing dopant concentration. The energetic shift demonstrates that this peak is due to the adsorbed CGNR and does not arise from the substrate. We assign the corresponding electronic state to the valence band (VB) of the CGNR, which has a binding energy of -0.87 ± 0.03 eV for the pristine CGNR. The binding energy decreases by around 0.1 eV per N atom and amounts to -1.01 ± 0.03 eV for the singly doped CGNR and -1.10 ± 0.05 eV for the doubly doped ribbon.

The results presented here demonstrate that a controlled, linear down-shift of the band structure of a bottom-up fabricated GNR can be achieved by precise doping of the precursor monomers. At the same time, the size of the band

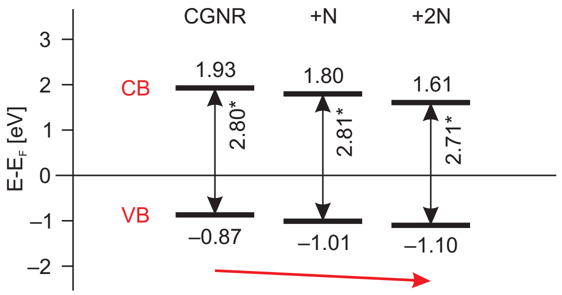

Figure 3.24: Overview of the band gap for the pristine and the two doped CGNR. Values marked with a (*) were obtained from HREELS measurements by S. Stremlau. Published in ref. [209].

gap remains unaffected, as expected for a pyridine-like N substitution (see Fig. 3.24). This result points toward the possibility of an independent manipulation of band gap size on the one hand and alignment of the electronic structure with the environment on the other hand. The band gap of around 2.8 eV is slightly higher than in case of the AGNR (2.6 eV) which is surprising because the CGNR has armchair-type segments with a width of $N = 9$. However, the inverse relation between the band gap and the ribbon width can not be expected to be applicable for quantitative comparison of chevron-shaped and straight GNR. The absolute energetic position of the VB with respect to the Fermi level for the pristine CGNR agrees with UPS data from ref. [160].

3.3.2 Image-Potential State of CGNR: Dispersion and Dynamics

In the previous section we used UPS to investigate the occupied electronic states while the conduction band energies of the three different CGNR could be inferred from HREELS measurements of the band gap. A systematic study of the unoccupied electronic states with 2PPE will be given in this section. Here, we will only discuss the undoped CGNR because the results for the two doped CGNR systems are very similar. The respective data are shown in appendix G. For the following experiments, CGNR were prepared on the Au(111) surface as described in the previous section 3.3.1.

Fig. 3.25a shows a series of 1C-2PPE spectra recorded with different photon energies. The work function amounts to 4.66 ± 0.02 eV. At final state energies up to 7 eV, one can observe the typical d-band features of Au(111). In the energetic region between 7.5 eV and 9.5 eV, two features can be observed for $h\nu > 4.33$ eV whereas there is only one peak for lower photon energies which in addition is partially cut off by the Fermi edge. We can immediately conclude that these two features do not arise from occupied electronic states because otherwise their energetic position relative to the Fermi edge should be independent of the photon energy. The shift of these two peak with increasing photon energy does not behave as expected, i.e. shift with a constant, integer

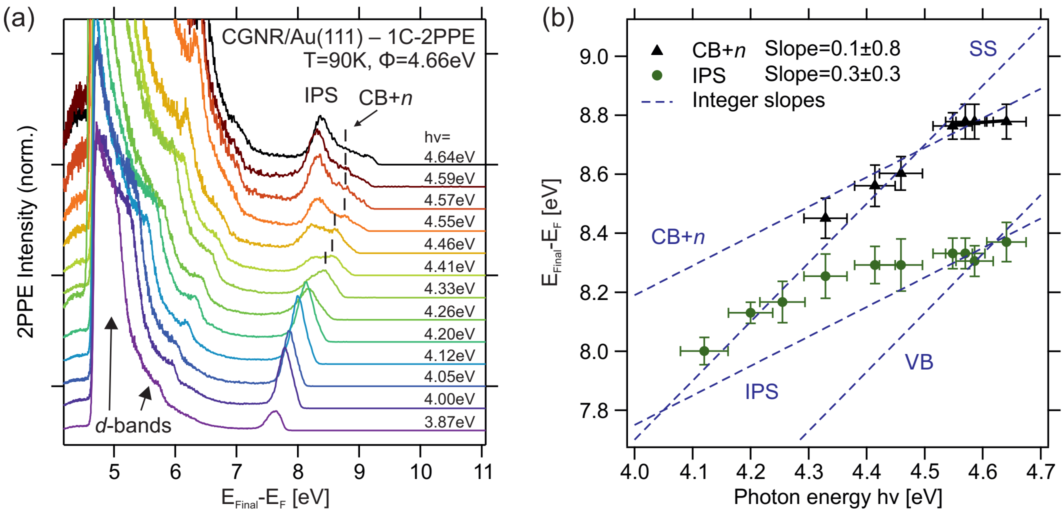

Figure 3.25: (a) 1C-2PPE spectra of the undoped CGNR on Au(111) for varying photon energies $h\nu$. The spectra have been normalized to one of the d-band features. (b) Shift of the IPS and CB+n peak positions with $h\nu$. The blue dashed lines represent the calculated final state energy for an integer slope which is based on the UPS values for the two occupied states (slope: 2) and the four data points with highest $h\nu$ for the two unoccupied states (slope: 1).

slope (see Fig. 3.25b). Instead, there are different photon energy ranges in which the features exhibit a different peak shift. Since the energetic positions of these two features are not independent of the photon energy, we can rule out that they arise from final states above the vacuum level. We can thus identify the two electronic states corresponding to these peaks as being unoccupied. The state represented by the peak labeled IPS is located at 3.75 ± 0.07 eV with respect to the Fermi level whereas CB+n has a binding energy of 4.19 ± 0.08 eV (for these values, only the four spectra with highest $h\nu$ were taken into account). The peak labeled IPS has a binding energy of 910 meV with respect to the vacuum level. However, due to the coverage of 2/3 ML the measured, average work function of the sample can be expected to be higher than the local work function (see sect. 3.2.4).

From the UPS experiment in sect. 3.3.1 we know that the energetic position of the valence band is -0.87 eV and we have observed that the surface state is not quenched. We can calculate the final state energies at which peaks would be expected to arise due to these two occupied states as well as due to the two unoccupied states found above (blue lines in Fig. 3.25b). The actual data points of both observed peaks deviate from the expected behavior (toward the surface state). Furthermore, the intensity of the peak labeled IPS is enhanced when the corresponding state is pumped from one of the occupied states. We attribute the peculiar behavior of the two peaks associated with unoccupied states to resonances with the occupied states. Besides an increase in peak intensity, this also causes an apparent shift of the observed peaks since the resonant intensity enhancement generally does not occur in the center of the peak.

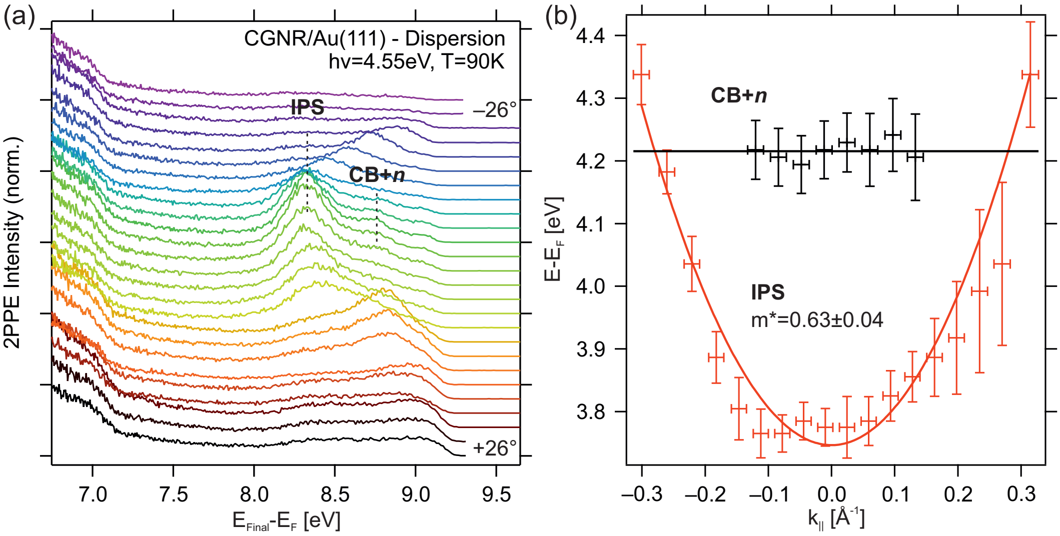

Figure 3.26: (a) Angle-resolved 1C-2PPE experiments for the CGNR. The spectra were normalized to one of the d-band features. (b) Shifting binding energy of the two unoccupied electronic states in the experiment shown in (a). A parabolic fit to the IPS binding energies yields the effective mass of $m^* = 0.63 \pm 0.04$ whereas the CB+n is localized.

In order to gain more insight into the nature of the two unoccupied states found in 2PPE, we performed angle-resolved 2PPE, the results of which are shown in Fig. 3.26. The IPS disperses around the Γ-point and its binding energy can be fitted well with an effective mass of $m^* = 0.63 \pm 0.04$. In contrast, the higher-lying electronic state is localized.

Based on its energetic position and dispersion we assign the IPS peak to the image potential state of the CGNR on Au(111). The state at higher energy can be attributed to a higher lying band, CB+n, which was also observed for the AGNR and there, too, does not exhibit a significant dispersion.

The ultrafast dynamics of the unoccupied electronic states was furthermore investigated with time-resolved 2PPE (TR-2PPE). Fig. 3.27 shows a two-color TR-2PPE experiment performed on the CGNR which employs a UV and a visible pulse as pump and probe, respectively (for positive delay values). The photon energy has been chosen such that both the IPS and the CB+n can be observed. Note, that the final state energy of the two peaks is lower than in the spectra shown in Fig. 3.25a because in this 2C-2PPE experiment, the

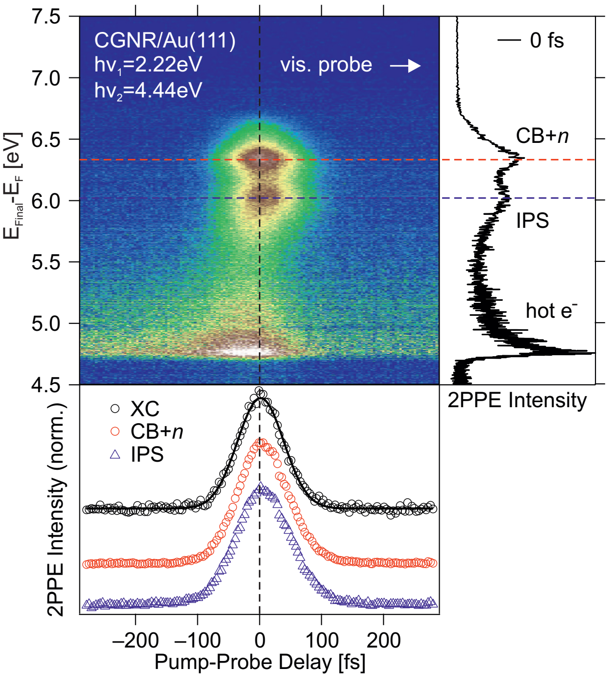

Figure 3.27: Time-resolved 2C-2PPE experiment of the CGNR on Au(111). The false color plot displays the 2PPE intensity (blue: low, white: high) versus final state energy and pump-probe delay. Positive delay values correspond to the situation in which the visible pulse ($h\nu$ = 2.22 eV) is the probe pulse. The bottom graph shows the cross-correlation traces of the IPS and CB+n together with the cross-correlation of the two laser pulses (XC) which has been measured at around 6.7 eV and which yields a single pulse width (FWHM) of 62 fs. The right graph shows a 2C-2PPE spectrum at zero delay with the IPS and CB+n. The increased intensity at the secondary edge is due to hot electrons.

states are probed with a different photon energy, namely $h\nu_1 = 2.22$ eV. Due to their energetic position close to the vacuum level, both unoccupied states are probed with the visible pulse rather than the UV pulse.

The cross-correlation of the two laser pulses has been measured at the Fermi edge (around a final state energy of 6.7 eV), which provides the origin of the delay axis as well as the temporal pulse width of the laser pulses, namely 62 fs (FWHM of a single pulse). Together with this measurement of the pulse duration, the cross-correlation traces of the two unoccupied states are shown in Fig. 3.27. The traces for both states have the same shape as the cross-correlation of the laser pulses and no asymmetry is observed. We can thus concluded that neither state possesses a lifetimes which can be resolved with the present temporal resolution. The short lifetime indicates effective de-excitation channels both for the IPS as well as for the CB+n which might be due to decay within the CGNR or charge-transfer into the substrate.

In summary, 2PPE has been investigated to study the properties of the IPS which is delocalized and possesses a short lifetime. Furthermore we find a weak signal of an energetically higher-lying band with a localized character. As already mentioned above, we have conducted analogous 2PPE measurements for the (singly and doubly) doped CGNR. The results are very similar (see Fig. 3.28) and the reader is referred to appendix G for a detailed discussion. The main difference lies in changes of the binding energy of the IPS, which follows the behavior of the work function rather than the doping-induced down-shift

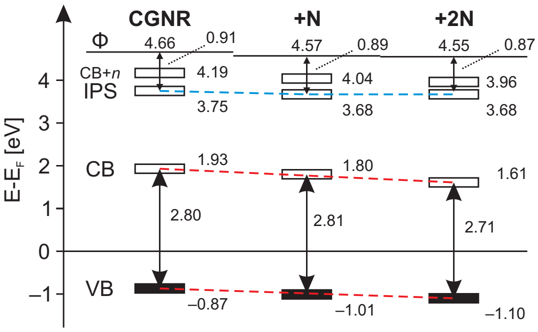

Figure 3.28: Comparison of the electronic structure of the undoped CGNR with the singly and doubly doped CGNR, which are described in appendix G. While the gradual down-shift of the bands has been described in sect. 3.3.1, we find that the image potential state is aligned to the vacuum level rather than the Fermi level, as expected.

of the CGNR band structure. This behavior is in full agreement with the behavior expected for an IPS and furthermore in full analogy to the AGNR discussed in sect. 3.2.4. Compared to the IPS of the AGNR, the effective mass in the IPS of the CGNR is reduced by approximately half.

3.4 Summary: GNR

In the present chapter we have first reviewed the electronic structure of GNR as well as the previous work concerning their fabrication through thermally induced covalent self-assembly of molecular precursors on the Au(111) surface. We then discussed the results obtained in this thesis work in the context of measurements and calculations by different collaborators and other groups. A straight AGNR with armchair-shaped edges was investigated as well as a chevron-shaped CGNR and two N-doped derivatives.

We investigated the thermal synthesis reaction toward the AGNR by analyzing the different intermediate phases and additionally studied a photo-induced reaction of the molecular precursors. In the initial monomer phase DBBA molecules are adsorbed in islands comprised of dimer rows which indicates molecule–molecule interaction. Furthermore, upon adsorption of DBBA on the Au(111) surface at room temperature, the molecule is not immediately dehalogenated. This activation of the precursors must therefore occur during the first annealing step which yields the polyanthrylene. Using 2PPE and STS, a total of five molecular orbitals of DBBA are observed which appear to be involved in the photo-induced reaction of the adsorbed monomers.

Using TPD, the thermal on-surface synthesis reaction could be followed “live” by analyzing the desorption behavior of the anthracene backbone as well as other fragments. The multilayer structure does not contain Br which is somewhat puzzling and may be due to polymerization in the higher layers. In the first layer, atomic Br is present even after the polymerization step and desorbs only associatively with H which is released in the cyclodehydrogenation reaction.

Experiments on the intermediate polyanthrylene reveal the presence of dispersing bands and a rather large band gap of 5.25 eV. DFT calculations show that the charge carrier mobility is mainly due to the overlap of the π-systems of neighboring anthracene units which is fostered by the flattened structure of the adsorbed polyanthrylene. Complementary 2PPE and HREELS measurements demonstrate that the band gap in the fully conjugated AGNR is only half as large as in the polymer and amounts to 2.60 eV, in good agreement with other calculations and recent experiments. Surprisingly, the conduction band of the AGNR has a very high effective mass and does not show a measurable dispersion either on the Au(111) or on the stepped Au(788) surface where the AGNR are aligned parallel to each other. We furthermore investigated the IPS of the AGNR which is energetically pinned to the local work function during co-adsorption of Xe. Due to their low density of states, we can not use our averaging photoemission technique to investigate the edge states which are localized at the zigzag edges (ends) or the AGNR.

Illumination experiments demonstrate a light-induced covalent coupling of the DBBA monomers on the Au(111) surface which is initiated by ionic resonances of the adsorbate molecule. This non-thermal process is interesting as it opens a perspective toward photo-induced assembly of GNR on surfaces, combining the structural advantages of atomically precise bottom-up synthesis with the controllability of top-down processes.

In addition to the AGNR, we investigated the influence of pyridine-like N-doping in CGNR which leads to a gradual down-shift of the band structure with respect to the Fermi level, while the size of the band gap and the on-surface synthesis itself remain unaffected by the precursor doping. Therefore, an independent tailoring of the band gap and its alignment with the electronic structure of other materials (e.g. in a nanotechnological device) seems possible. Furthermore, using 2PPE, we characterized the IPS of the CGNR which does not shift along with the band structure but remains pinned to the local vacuum level.

Chapter 4

Photoisomerization and Thermally Induced Reaction of an Azobenzene Derivative on Bi(111)

The following, second part of this thesis discusses reactions of di-meta-cyano-azobenzene (DMC) adsorbed directly on the semi-metallic Bi(111) surface as well as in higher layers of thin adsorbate films on the same substrate. First, we will review the isomerization mechanism of the isolated azobenzene molecule and reactions of DMC as well as the different photo-induced electronic excitation mechanisms at adsorbate-covered surfaces. We will then turn to the results of the present work, namely photo-induced isomerization reactions of an azobenzene derivative in the different coverage regimes and thermally induced processes performed by the resulting *cis* isomers.

4.1 Background: Reactions of Azobenzene and Excitation Mechanisms at Surfaces

The preceding, first part of this thesis has been concerned with graphene-derived structures as an approach to address the nanotechnological challenges of our day. A different strategy, which will be followed in this second part, is the development of molecular or supramolecular units with specific functions. One class of these units are molecular switches which have different molecular states and can be converted from one state to another by different forms of external manipulation, the most prominent stimulus being light. The different properties of these molecular states determine the function of the molecular unit [79, 23, 24, 25]. A large variety of different molecular switches exists [80, 82, 89, 87] which constitutes an equally diverse spectrum of interest and proposed applications, ranging from fundamental research to nanotechnological devices [104, 96, 98, 29, 31, 14, 101].

One major challenge is the transfer of molecular switches into the condensed phase, e.g. on a surface or at an interface, which is a necessary prerequisite for most applications. Different forms of molecule–substrate interaction, such as steric effects and efficient de-excitation due to electronic coupling, frequently lead to quenching of the molecular functionality. On the other hand, the substrate may also offer new excitation channels which are not available for the isolated molecule. Investigation of the substrate–adsorbate interplay is therefore crucial for the understanding of functional molecules on surfaces.

4.1.1 Isomerization Reactions of Azobenzene in Solution

Among the photochromic molecular switches, the function of which is initiated by light, azobenzene arguably is the most prominent representative due to its relatively simple structure (see Fig. 4.1a) [211, 80, 212, 81, 213]. The thermodynamically stable form of azobenzene is the *trans* isomer (or *E* isomer) in which both phenyl rings are bound to an sp^2-hybridized diazo group with a stiff double bond. Two characteristic angles are typically used to describe the conformation of azobenzene, which are closely related to two different isomerization pathways: the inversion angle θ and the rotation angle φ. The *trans* isomer is planar and has a vanishing dipole moment due to its inversion symmetry. The other, meta-stable conformation of azobenzene is the *cis* isomer which is three-dimensional and possesses a dipole moment of around 3 D [214] due to the electronegative N atoms. On the potential energy surface (PES) of the electronic ground state S_0, the *cis* isomer is separated from the *trans* isomer by an activation barrier of 0.91 to 1.22 eV (in *cis*–*trans* direction) [215, 216, 217] and the energetic difference between both isomers amounts to 0.58 eV [218].

While the activation barrier between the *cis* and the *trans* isomer can be transcended thermally and unidirectionally, photo-induced isomerization pathways allow bidirectional switching (see Fig. 4.1b). Absorption of UV light around 300 nm by the *trans* isomer leads to an excitation into the S_2 state ($\pi \rightarrow \pi^*$ transition). The system then relaxes along the PES of this state following the rotation pathway until it reaches a conical intersection and transitions to the S_1 state. There, it relaxes further, via the *trans* geometry and

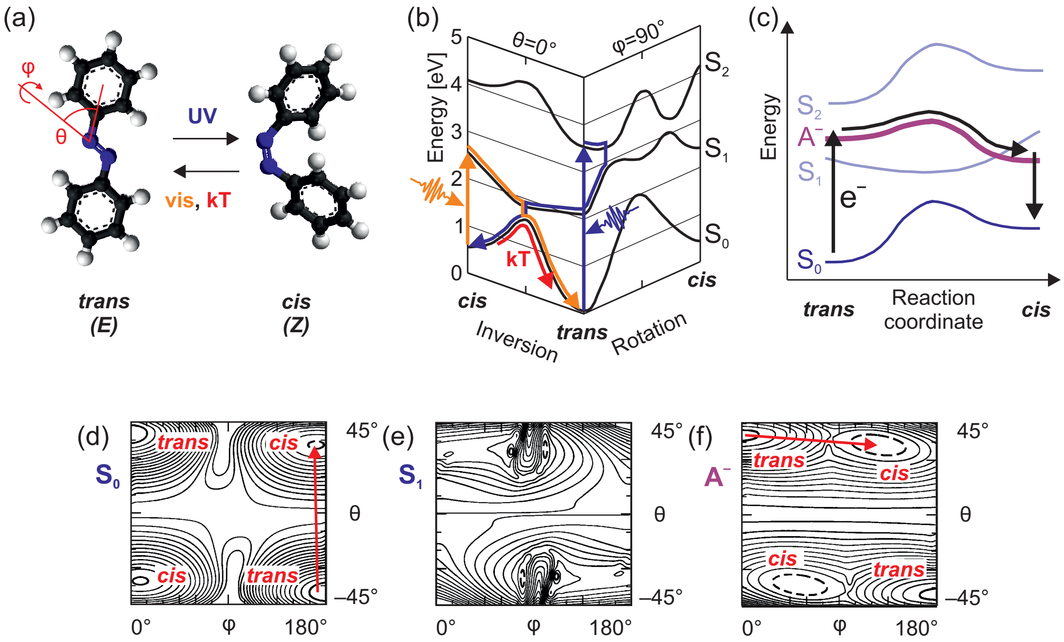

Figure 4.1: (a) Structure of *trans* (E) and *cis* (Z) azobenzene and interconversion channels in solution. Θ is the angle associated with inversion, whereas φ describes the rotation pathway. (black: C, blue: N, white: H atoms) (b) Photoisomerization mechanisms for the *trans–cis* (blue) and *cis–trans* (orange) reactions along the PES of the ground state S_0 and the first two excited singlet states $S_{1,2}$ in the free molecule and thermally induced *cis–trans* reaction (red). Adapted from ref. [81]. (c) Schematic depiction of an isomerization along the PES of an anionic resonance upon electron attachment. (d-f) Contour plots of the calculated PES for the first two singlet states of the neutral molecule (d,e) and the ground state of the anionic azobenzene molecule (f). Arrows schematically indicate *trans–cis* isomerization pathways. Adapted from ref. [109].

the minimum of S_1 which lies above the barrier of the ground state. The system de-excites into the ground state and, with considerable probability, follows the inversion pathway toward the *cis* isomer. The photo-induced back-reaction is initiated by the absorption of a photon in the visible spectrum around 435 nm which excites the molecule into the S_1 state ($n \to \pi^*$ transition), followed by relaxation along the inversion pathway back toward the *trans* isomer [80, 81]. Both isomerization directions can however be initiated by transitions to either S_1 or S_2. Therefore, absorption of both visible and UV light leads to the establishment of a photostationary state (PSS) consisting of *trans* and *cis* isomers in a specific ratio [219, 220].

While the above discussed molecular states were all neutral excited states induced by intramolecular absorption of a photon, another form of molecular excitation is the attachment of electrons (holes), leading to anionic (cationic) resonances of the molecule. Fig. 4.1c shows how the PES of an ionic resonance can lead to *trans–cis* isomerization if it has a minimum close to the *cis* geometry and an activation barrier which can be overcome at a given temperature. Fig. 4.1d-f shows PES of the electronic ground state and the S_1 state of the neutral molecule as well as the PES of the anionic ground state calculated for di-meta-cyano-azobenzene using DFT and time-dependent DFT (TD-DFT) [109]. While according to these calculations, the activation barrier for *trans–cis* isomerization in the neutral ground state is 1.72 eV, the barrier is reduced to 0.54 eV in the anionic state. This barrier reduction can be attributed to a weakening of the double bond of the diazo group due to occupation of an antibonding π^* orbital in the anionic case. Nevertheless, even in the anionic state, the *trans* isomer is the stable form and therefore *trans–cis* isomerization along the PES of the anionic state can not be achieved. When the molecule is adsorbed on a surface however, it is conceivable (i) that the activation barrier may be lowered due to additional filling of the antibonding π^* orbitals and (ii) that the *cis* form may be stabilized due to the formation of a partially covalent bond between the lone pair orbitals of the diazo group and the substrate atoms. Both effects have been observed for DMC adsorbed on Cu(100) (see sect. 4.1.2) [221].

4.1.2 Interaction of Adsorbed DMC with Different Substrates

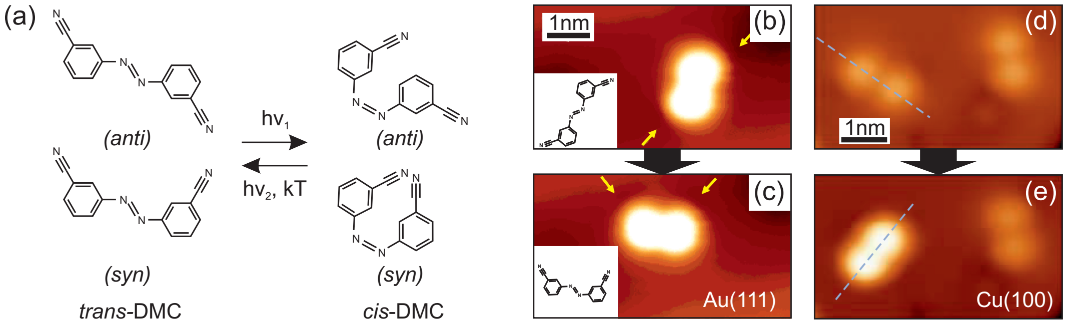

Figure 4.2: (a) Structure of DMC for the two isomers (*trans* and *cis*) and their two respective rotamers (*syn* and *anti*), along with interconversion pathways. For simplicity, the structures are drawn in plane although the *cis* isomer is not planar. (b) STM image of *anti-trans*-DMC on Au(111). Arrows indicate depressions in the tunneling current associated with the cyano groups. (c) STM image of the same molecule as in (b) after applying a voltage pulse of $V_S = 1.8$ V, resulting in *syn-trans*-DMC. (c) and (d) adopted from ref. [111]. (d) STM image of two *anti-trans*-DMC molecules adsorbed on Cu(100) ($V_S = -0.72$ V, $I_t = 0.54$ nA). (e) STM image of the same two molecules after positioning the tip over the left molecule with a bias of $V_S = -2$ V which leads to *trans–cis* isomerization. (d) and (e) adopted from ref. [221].

In order to foster the isomerization efficiency of azobenzene derivatives, especially on surfaces, a modification of the PES in the ground state and the excited molecular states is desirable, i.e. a reduction of the barriers. In the ground state, a reduced barrier between the *trans* and *cis* isomers leads to an increased efficiency of the thermal reaction, which however is unidirectional toward the stable form. The relative stability of the conformational forms of an adsorbed photoswitch may be inverted with respect to the free molecule [221, 92]. On the other hand, a reduced barrier between the two isomers in an excited molecular state (neutral or ionic) may increase the efficiency of the photoisomerization toward the meta-stable isomer.

The activation barriers of an azobenzene molecule can be influenced mainly in two ways: by substitution of the phenyl rings with various side groups or by adsorption on a substrate. DFT calculations predict that substitution of azobenzene with two cyano groups in the meta positions (DMC, see Fig. 4.2a) lowers the barrier in the ground state and additionally results in a relatively low barrier in the anionic state [109]. This lowering of the barriers is due to the electronegative character of the cyano groups which withdraw electron density from the central diazo bridge—more precisely, from the bonding π orbitals of the double bond.

Besides reduced barriers in the ground state and the anionic state, DMC furthermore has a relatively high dipole moment of 7.0 D which is also attributed to the electronegative cyano groups [109]. This increased dipole moment makes DMC suited for photoisomerization experiments using a photoemission setup because a change in the surface dipole moment results in a change of the (easily measurable) work function.

DMC has previously been studied on two different metal surfaces by means of STM. Using the STM tip, reactions of adsorbed DMC can be induced in both cases which grant an insight into the substrate–adsorbate interaction for these systems.

On the Au(111) surface, DMC adsorbs in the *trans* form and the bond to this noble metal can be expected to be governed by physisorption. In a topographic STM image, the molecule shows two elliptical protrusions accompanied by subtle depressions associated with the cyano groups from which the rotational form (*syn* vs. *anti*) can be determined (see Fig. 4.2b) [111]. Upon application of a voltage pulse in the STM junction, the appearance of the molecule changes: the relative orientation of the two characteristic depressions changes which is ascribed to the rotation of a single phenyl ring by 180°, i.e. an *anti*–*syn* rotation of *trans*-DMC, as shown in Fig. 4.2c. The reaction is initiated by electron attachment to the LUMO of DMC, thus creating an anionic resonance of the molecule, in connection with the electric field of the STM junction. Isomerization reactions of azobenzenes adsorbed on metallic surfaces have frequently been induced with STM [93, 95, 94, 112, 221]. However, in the present case of DMC on Au(111), such a reaction can not be observed. In the presence of Co adatoms on the Au(111) surface, DMC forms metal–organic networks in which the electronegative cyano groups are bound to the adatoms [222].

When adsorbed on a different, namely the more reactive Cu(100) surface, DMC initially adsorbs in its *trans* isomer, too (see Fig. 4.2d) [221]. The geometry of the *trans* isomer on this surface is slightly bent due to the partially covalent character of the adsorbate–substrate bond at the diazo bridge. Particularly, the lone pair orbitals of the diazo bridge hybridize with the electronic states of the substrate. By applying voltage pulses in the STM junction, a *trans–cis* isomerization of the adsorbed DMC molecules can be induced which leads to a molecular configuration in which the cyano groups are oriented toward the vacuum [221]. A stability inversion is observed, i.e. the *cis* isomer is the stable conformation at the Cu(100) surface, which is due to the formation of a relatively strong covalent bond between the lone pair electrons of the diazo bridge and the substrate atoms. Because of this high degree of stability, the isomerization toward this form is unidirectional.

The two above case studies of DMC on Au(111) and Cu(100) demonstrate the crucial influence of the substrate on the adsorption and the isomerization behavior of adsorbed molecular switches. While the partially covalent character of the DMC–Cu bond is somewhat beneficial for the isomerization ability, as it weakens the double bond at the diazo group, it also eliminates the pathways leading back to the *trans* configuration. On the other hand, the attractive van der Waals interaction of the phenyl rings with the highly polarizable Au(111) substrate is disadvantageous with regard to isomerization, too. Due to the sensitivity of the molecular functionality to the interaction with the underlying substrate, a careful balance between van der Waals and covalent character has to be achieved in order to facilitate efficient bi-directional switching.

In the present thesis we investigate DMC adsorbed on the semi-metallic Bi(111) surface which should lead to a reduced van der Waals interaction with the molecule (compared to the Au(111) surface) due to the low density of states around the Fermi level. However, Bi is not as inert as Au and the DMC–Bi bond may thus have a partially covalent character which could weaken the double bond of the diazo bridge. Bi has shown to be a suitable substrate for photo-induced bidirectional isomerization of spiropyran [118]. Previously, we have investigated the unoccupied electronic structure of the Bi(111) surface in detail using 2PPE [223, 224] and the work presented in this thesis shows that the alignment of the molecular orbitals of DMC with the band structure of Bi fosters the photoisomerization.

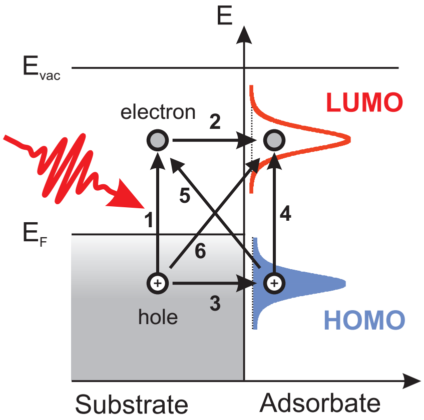

Figure 4.3: Different photo-induced excitation mechanisms at an adsorbate–substrate interface. Electron–hole pairs can be created by absorption of light in the substrate (**1**) or the adsorbate (**4**). Charge transfer processes (**2**,**3**) can transfer an excitation between the substrate and the adsorbate. Additionally, direct excitations from the substrate into the adsorbate orbital are possible (**5**,**6**).

4.1.3 Photo-Excitation Mechanisms at Adsorbate-Covered Surfaces

Generally, a (photo-)isomerization process of a molecular switch into the metastable state requires an excited molecular state which can be achieved by (i) an intramolecular electronic excitation in which an electron is promoted to an unoccupied molecular orbital or (ii) by creation of an anionic or cationic resonance, where a charge transfer between the molecule and its environment (e.g. the substrate) excites the adsorbate.

Different excitation mechanisms are depicted schematically in Fig. 4.3. As mentioned above, the simplest molecular excitation is the intramolecular absorption of a photon and hence electronic transition from an occupied to an unoccupied molecular orbital, e.g. from the HOMO to the LUMO (**4**) [225, 226, 227]. Although this initial process occurs within the molecule, the substrate has an influence on the subsequent evolution of the electronic and nuclear systems of the adsorbate molecule: for example, the HOMO–LUMO gap can be affected by the substrate (as compared to the free molecule), charge transfer of the excited electron or hole can lead to an ionic resonance or the potential energy surface of the molecular states may be altered due to the presence of the substrate (e.g. the surface can pose a steric barrier). This excitation pathway can only be initiated by absorption of a photon with a specific photon energy, $h\nu = E_{\mathrm{LUMO}} - E_{\mathrm{HOMO}}$. Besides in isolated molecules, intramolecular excitations often occur in the multilayer regime [228, 113, 122].

The substrate can also take a more central role in the photoexcitation process, namely by acting as a chromophore. Due to the higher phase space for electronic excitation and the ability to absorb photons in several atomic layers, the substrate usually has a higher photoabsorption cross section than an adsorbate (**1**). The excited charge carriers (electrons and holes) decay back toward the Fermi level via carrier–carrier scattering processes leading to a hot electron (hot hole) distribution [229, 230, 231]. These hot carriers can be transferred into the respective molecular orbitals of an adsorbate: electron attachment to unoccupied molecular orbitals creates an anionic resonance (negative ion resonance, **2**) [232, 233, 234, 140] whereas hole attachment to occupied molecular orbitals creates a cationic resonance (positive ion resonance), **3**) [235, 139]. Such charge transfer processes have been known to initiate chemical reactions in adsorbates due to the different PES of the respective resonance compared to the neutral molecule. Other effects of the substrate may influence the adsorbate reaction as well, such as steric effects or de-excitation of the ionic resonance by fast back-transfer of the charge carriers. In contrast to the discrete energy levels of an adsorbate, the bands of a substrate have a continuous energy distribution, allowing for excitation over a wide range of photon energies [205, 206].

Besides hot carrier transfer, ionic molecular resonances can be created by direct excitations from occupied substrate bands into unoccupied molecular orbitals (**6**) or from occupied molecular orbitals into unoccupied substrate bands (**5**). The difference to hot carrier transfer is a direct photo-induced transition due to a finite spatial overlap of the adsorbate orbital's wavefunction and the Bloch waves of the substrate bands. Compared to hot carrier transfer, direct excitations involving adsorbate molecular orbitals thus have a reduced phase space for electronic excitation [236].

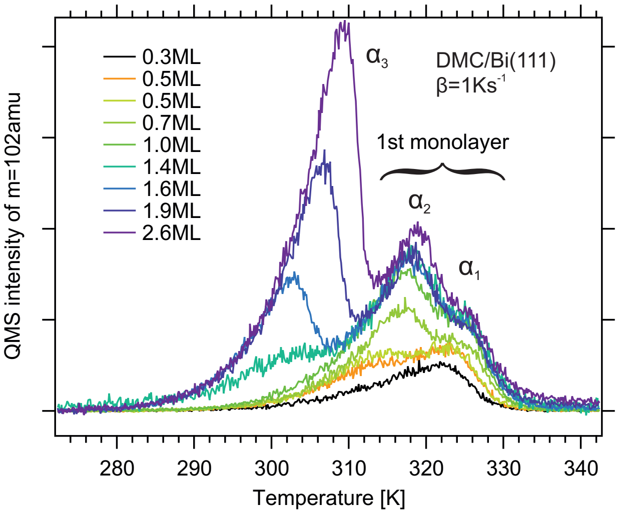

Figure 4.4: TPD curves of DMC desorbing from the Bi(111) surface recorded at a fragment mass of 102 amu ($C_6H_4CN^+$) for different initial coverages as indicated in the legend. Two saturating peaks $\alpha_{1,2}$ are assigned to the first monolayer while the non-saturating feature α_3 shows zero-order desorption behavior typical for the multilayer regime. A linear background has been subtracted from all TPDs. Published in ref. [172].

4.2 Results: Reactions of DMC in the First Monolayer and in the Multilayer Regime

In this section we will discuss the results obtained from photoemission and illumination experiments conducted on di-meta-cyano-azobenzene (DMC) adsorbed in different coverage regimes on the Bi(111) surface. First, a substrate-mediated photoisomerization reaction in the first adsorbate layer will be discussed in sect. 4.2.1. The subsequent section comprises experiments in the multilayer regime where we observe two photoisomerization processes and finally, in sect. 4.2.3, thermally induced reactions of the photo-fabricated *cis* isomers will be presented. DMC was synthesized by B. Priewisch in the group of Prof. Rück-Braun (Technische Universität Berlin) [237].

4.2.1 Photoisomerization of DMC in the First Monolayer

This section describes the *trans–cis* photoisomerization reaction of DMC adsorbed in the first monolayer on Bi(111). The results presented here have been published in *J. Phys. Chem. C* **117**, 27031 (2013) [172].

Thin films of DMC on the Bi(111) surface were prepared by evaporation of DMC from an effusion cell held at 107 °C onto a Bi(111) surface which was cooled to 120 K. These films were characterized by TPD of a prominent molecular fragment with a mass of 102 amu, namely a cyano-substituted phenyl ring ($C_6H_4CN^+$), as shown in Fig. 4.4. The coverage of the DMC film was varied by changing the evaporation time and it is proportional to the integral of the TPD. A total of three desorption peaks can be observed, one of which (α_3)

exhibits a zero-order peak form and does not saturate with increasing initial DMC coverage, which are both typical attributes of a multilayer desorption peak. The other two peaks (α_1 and α_2) saturate as the initial DMC coverage is increased. We assign both peaks to desorption from the first monolayer and interpret α_2 as a compressed phase which is common for azobenzenes adsorbed on metals [116, 175, 106]. Upon heating the sample to temperatures above 335 K, DMC is completely desorbed, as evident from posterior 2PPE, HREELS or Auger electron spectroscopy (AES) measurements.

An alternative explanation for a second, saturating desorption peak would be the formation of a bilayer. However, this can be ruled out based on the behavior of the IPS with increasing DMC coverage: as we will see below, the IPS of the bare Bi(111) surface decreases in intensity and simultaneously, a new IPS associated with the DMC-covered surface arises at a lower energy. The IPS of the bare surface is quenched completely when a coverage of 1 ML is reached (i.e. if defining a monolayer as comprised of both α_1 and α_2) and thus, α_2 arises due to DMC desorption from the first monolayer.

An absolute quantification of the coverage can be obtained from the TPD curves by integration and normalization to the area of a TPD which is defined as 1.0 ML. However, due to the limited number of available curves, the TPD defined as 1.0 ML has a coverage which is lower because one chooses the TPD with the highest integral in which the multilayer feature α_3 is not observed. Due to this systematic error in the coverage gauging, the stated coverages generally deviate toward higher values. We have taken this effect into account by stating coverages only to a precision of 0.1 ML.

For the illumination experiments in this section, we prepared a coverage of 1.0 ML by adsorption of a multilayer film and subsequent annealing at 300 K for 1 min in order to thermally desorb the higher lying layers. A temperature of 240 K was thereafter maintained for 30 min to allow for ordering processes to occur.

Before investigating the photo-induced reactions, we use UPS and 2PPE to characterize the electronic structure of the system which will prove to be highly relevant for the understanding of the photoisomerization mechanism. Fig. 4.5a shows UPS spectra recorded with the quadrupled fundamental of the Ti:Sapphire laser system for the bare Bi(111) surface and various coverages of DMC. In the absence of an adsorbate, three peaks, $\mathrm{Bi}^{(1-3)}$, are observed which arise from electronic bands and surface states or resonances of the substrate, respectively, and have been studied previously by the author of the present thesis [223]. The spectrum can be reproduced by three Gaussian fit functions on a linear background which is cut off by a Fermi function. With increasing DMC coverage, a new peak rises in intensity. Consequently, the spectra recorded on the DMC-covered surfaces have been fitted with an ad-

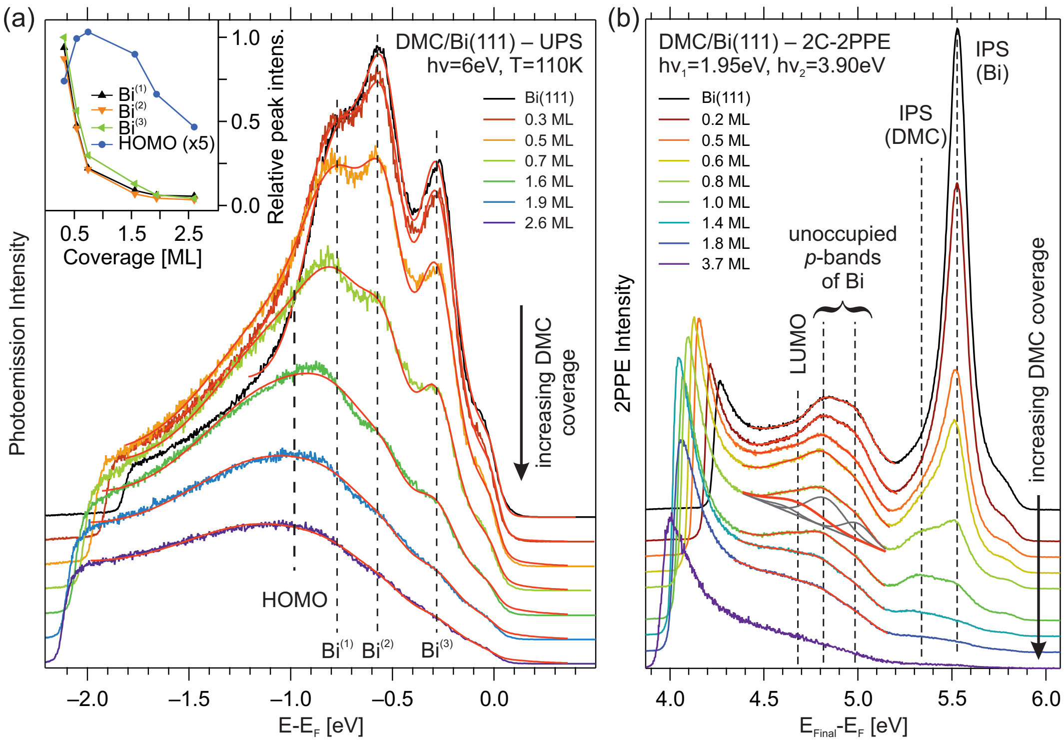

Figure 4.5: (a) UPS spectra recorded for increasing coverages of DMC on Bi(111). Besides three features originating from the substrate ($\mathrm{Bi}^{(1-3)}$), the HOMO of adsorbed DMC is found. The red curves represent fits to the spectra as described in the text. The inset shows the intensity of the fit components with increasing coverage. (b) 2C-2PPE spectra for various coverages of DMC on Bi(111). The features associated with the unoccupied substrate *p*-bands (grey) and the LUMO of DMC (bold red curve) were fitted as described in the text. The individual fit components are shown exemplarily for the spectrum recorded at a coverage of 0.8 ML. (a) and (b) published in ref. [172].

ditional Gaussian peak while keeping the position and width of the other fit components (originating from the substrate) fixed. Although the intensity of the fit components was kept free, the relative intensity of all three substrate peaks changes in the same manner (see inset in Fig. 4.5a). We assign the new peak to the HOMO of DMC. Its binding energy is determined from the fits as -0.98 ± 0.05 eV with respect to the Fermi level and angle-resolved UPS measurements demonstrate that it is localized, i.e. it doesn't show a dispersion.

In analogy to these UPS results, 2C-2PPE spectra have been recorded for various DMC coverages in order to investigate the unoccupied electronic states of the system, as shown in Fig. 4.5b. The work function decreases with increasing DMC coverage, from 4.23 ± 0.03 eV for the clean substrate to 4.05 ± 0.02 eV at a coverage of 1.0 ML. The spectrum of the bare Bi(111) surface contains an intense feature at a final state energy of 5.54 ± 0.04 eV which can be assigned to the $n = 1$ IPS based on previous experiments by our group and Muntwiler *et al.*, respectively [238, 223]. From the present spectra we find a binding energy of 3.59 ± 0.05 eV with respect to the Fermi level.

The peak intensity decreases upon adsorption of DMC and at the same time, a new peak gains intensity at 5.35 ± 0.04 eV. The energetic different between these two peaks corresponds to the work function difference between the clean surface and a DMC-covered one with a coverage of 1.0 ML. Furthermore, the corresponding electronic state can be identified as unoccupied based on the peak shift with varying photon energy. The peak exhibits a dispersion with an effective mass of $m^* = 1.3 \pm 0.3$ in angle-resolved 2PPE experiments (at a coverage of 1.0 ML). This unoccupied electronic state is consequently identified as the IPS of the adsorbate-covered surface and its binding energy amounts to 3.40 ± 0.05 eV.

In the spectrum which was recorded at a coverage of 1.0 ML, the IPS of the bare surface shows a residual intensity even though it should be completely quenched. This is a consequence of the systematic error that is made in the coverage gauging as described above. Since the energetic position of the two IPS features is independent of the coverage and one IPS rises in intensity while the other loses intensity we can conclude that DMC grows in islands on the Bi(111) surface. Otherwise, a continuous energetic shift of a single IPS peak would be expected due to the pinning of the IPS to the (continuously shifting) average vacuum level of the entire sample rather than the local vacuum level within the island (see discussion of the IPS of AGNR in sect. 3.2.4).

At lower final state energies between 4.5 eV and 5.2 eV, the spectrum of the bare surface contains a broad feature which can be fitted with three Gaussian fit functions on a linear background and arises due to unoccupied p-bands [223]. Note, that the intensity distribution of the spectral feature reflects the density of states of the respective bands. In analogy to UPS, the 2PPE spectra show a new feature at a final state energy of 4.67 ± 0.03 eV upon adsorption of DMC (this features is also observed in 1C-2PPE, see appendix H). The respective spectra have consequently been fitted with four Gaussian peak profiles. However, the free parameters were limited by keeping the energetic position and width of the substrate features fixed as well as their relative intensity. The individual fit components for all fitted spectra can be found in appendix I. The electronic state associated with the DMC-induced peak can be identified as unoccupied due to its photon-energy dependent energetic shift. Furthermore, it does not show a dispersion in angle-resolved 2PPE measurements or a significant lifetime in time-resolved 2PPE experiments. Due to these properties we assign this state to the LUMO of DMC, the binding energy of which amounts to 0.77 ± 0.05 eV.

When the DMC-covered surface is exposed to UV photons such as those

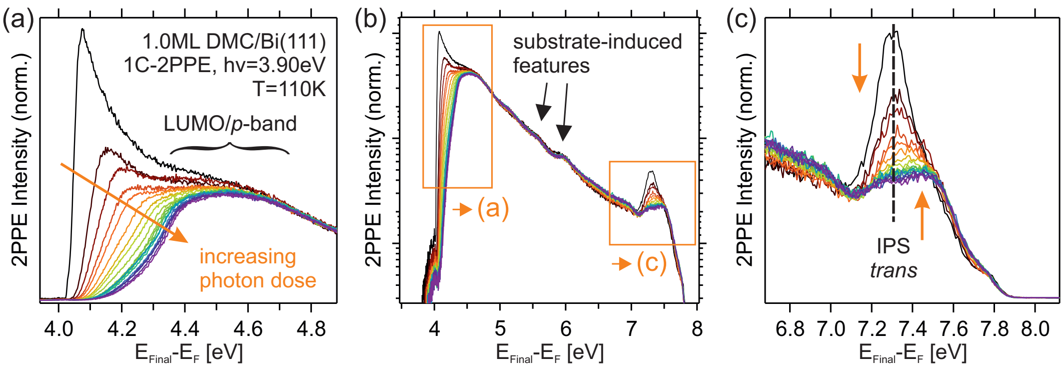

Figure 4.6: Continuous photo-induced changes in 1C-2PPE spectra of a DMC-covered surface. The three graphs show different energy regions of the same data set. The spectra have been normalized to the intensity at a final state energy around 5 eV. Orange arrows indicate the spectral changes with increasing photon dose. The averaged photon fluence in this experiment was $f = 5.9 \times 10^{20}$ cm^{-2}s^{-1} and the stated sample temperature of 110 K was maintained during the entire illumination experiment. (a) Changes to the secondary edge as well as a broad feature arising from the LUMO and the unoccupied p-bands. (b) Complete spectra. The energy regions shown in (a) and (c) are highlighted. (c) Changes near the Fermi edge and most notably, the IPS. (a) and (c) published in ref. [172].

used in 1C-2PPE, continuous changes can be observed in the spectra as shown exemplarily in Fig. 4.6a-c for a photon energy of 3.90 eV. Note, that the photon doses necessary to acquire a single spectrum are negligible compared to those necessary to induce spectral changes[1]. The work function increases gradually by 250 meV (see Fig. 4.6a), which is a relatively large value compared to the work function increase of 50 meV during photoisomerization of tetra-*tert*-butyl-azobenzene (TBA) on the Au(111) surface [116]. If we assume that the spectral changes observed for DMC/Bi(111) are due to a photoisomerization as well (as we will see later on), an increase of the work function is consistent with the electronegative cyano groups pointing toward the vacuum. The relatively large work function increase might be attributed to the higher dipole moment of DMC, compared to TBA [109], or a different isomer ratio in the photostationary state (PSS), or both.

At final state energies between 4.9 eV and 6.7 eV, no significant changes are observed in the spectra (see Fig. 4.6b). The broad feature observed between 4.4 eV and 4.8 eV arises both due to the LUMO of DMC and unoccupied p-bands of the substrate but in these 1C-2PPE experiments the components can not be resolved as well as in 2C-2PPE. Therefore we can not conclude to the behavior of the LUMO during the photo-induced process. The IPS of the

---

[1] For example, in order to record one spectrum of the series shown in Fig. 4.6a-c, the sample was exposed to a photon dose of $2.0 \pm 0.5 \times 10^{21}$ cm^{-2} whereas the accumulated photon dose in the entire experiment was $1.7 \pm 0.2 \times 10^{24}$ cm^{-2}.

Figure 4.7: TPD curves recorded for eight different preparations of 1.0 ML DMC/Bi(111), showing the monolayer desorption peaks $\alpha_{1,2}$. One of the samples was illuminated with a KrF laser, the spot of which covered 33% of the sample surface (sample diameter: 10 mm). The corresponding TPD is shown in red. The right graph shows the coverage of the eight preparations as determined from the integral of the TPD. The inset shows the work function change during KrF illumination, measured with the visible OPA output ($h\nu_{\text{meas.}}$ = 2.44 eV). Published in ref. [172].

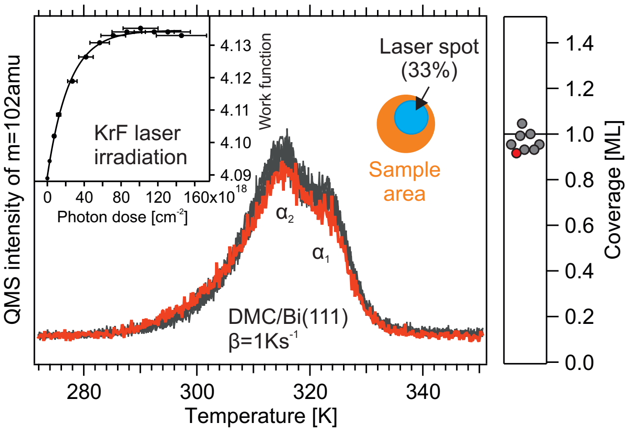

DMC-covered surface, located at a final state energy of 7.3 eV (see Fig. 4.6c), loses intensity with increasing photon dose and the spectral weight in this region is shifted to higher energies. However, due to the noise level we can not distinguish between a continuous shifting of the IPS energy on the one hand or a decrease of the IPS peak accompanied by a simultaneous increase of a new IPS feature associated with the photo-product on the other hand. The former would be expected in case of a photo-induced process which is independent of the molecular environment. While intensity variations of spectral features can only be observed for those photon energies at which the respective features occur in the spectra, the work function is an easily accessible quantity in every photoemission spectrum. Consequently, we use the work function change as a measure for the photo-induced changes of the adsorbate in the quantitative analysis presented below.

Before quantifying the photo-induced process, we should however first discuss its nature. A number of light-induced processes are conceivable for molecular adsorbates on metal surface. With regard to previous studies of DMC on Au(111), a phenyl ring rotation [111] could be one of them but is inconsistent with the observed changes in the spectra, most notably the increased work function. Another possible process could be laser-induced desorption. However, the spectra do not evolve toward those recorded on the clean surface. Upon irradiation with UV light, dissociation processes could lead to a fragmentation of the molecule. In order to rule out such a beam damage effect, we conducted an experiment in which a substantial portion of the sample surface was illuminated using a KrF excimer laser[2] with a spot diameter of 5.8 mm,

---

[2] $\lambda = 248$ nm, $h\nu = 5.0$ eV, repetition rate 57 Hz, pulse energy 1.7 ± 0.4 mJ cm^{-2}.

in contrast to experiments with the Ti:Sapphire laser setup where the spot diameter is usually on the order of 50 to 100 μm. The system was brought into saturation, as evident from the work function which was monitored during illumination (see inset of Fig. 4.7). A subsequently recorded TPD at the mass of the $C_6H_4CN^+$ ion (102 amu) shows no significant changes in either shape or area of the desorption peaks which demonstrates that the photo-product can not be comprised of molecular fragments smaller than a cyano-substituted phenyl ring and that the binding energy is unaffected by the process, which would not be expected in case of dissociation. We therefore conclude that the most likely origin for the changes observed in the spectra is a photo-induced *trans–cis* isomerization of DMC on the Bi(111) surface[3].

Based on this conclusion and the interconversion channels of azobenzene in solution, a photo-induced *cis–trans* reaction on the surface is conceivable which would be initiated by light in the visible spectrum. Indeed we illuminated samples, which had previously been brought into saturation with UV light, with visible light between 1.9 eV and 2.5 eV but from our data we can not conclude to a *cis–trans* isomerization. This might be explained by a stabilization of the *cis* isomer on the Bi(111) surface, efficient quenching of the respective excited molecular state (S_1 in solution).

A quantitative analysis of the photoisomerization process can be performed in order to gain an insight into the mechanism that drives this reaction. As already mentioned, the work function Φ is the suitable measure for this task and we henceforth assume the change of Φ to be proportional to the number of molecules in the *cis* state. Fig. 4.8a shows the evolution of the work function in an illumination experiment with $h\nu = 3.90$ eV as a function of the photon dose to which the sample has been exposed. The behavior can be described very well with a mono-exponential fit function

$$\Phi(d) = \Phi(0) + \Delta\Phi \exp\left(-\sigma d\right), \tag{4.1}$$

where $\Delta\Phi$ is the asymptotic work function change and σ is the effective cross section which in this particular experiment amounts to $\sigma = 2.1 \pm 0.2 \times 10^{-24}$ cm^2. This value is relatively low compared to the effective cross section of the photoisomerization of TBA/Au(111), which is on the order of 10^{-22} cm^2 [139] or 10^{-23} cm^2 [240] for photon energies below 4.5 eV. In another study, an effective cross section of 6×10^{-20} cm^2 is found for the photoisomerization of a different azobenzene derivative on the Cu(111) surface [117]. In comparison, the present isomerization reaction is a rather inefficient one.

---

[3] DMC is adsorbed in the first monolayer of the Bi(111) surface in its *trans* configuration, as determined using HREELS in our group (conducted by S. Stremlau) [190] and near-edge x-ray absorption fine structure (NEXAFS) measurements [239].

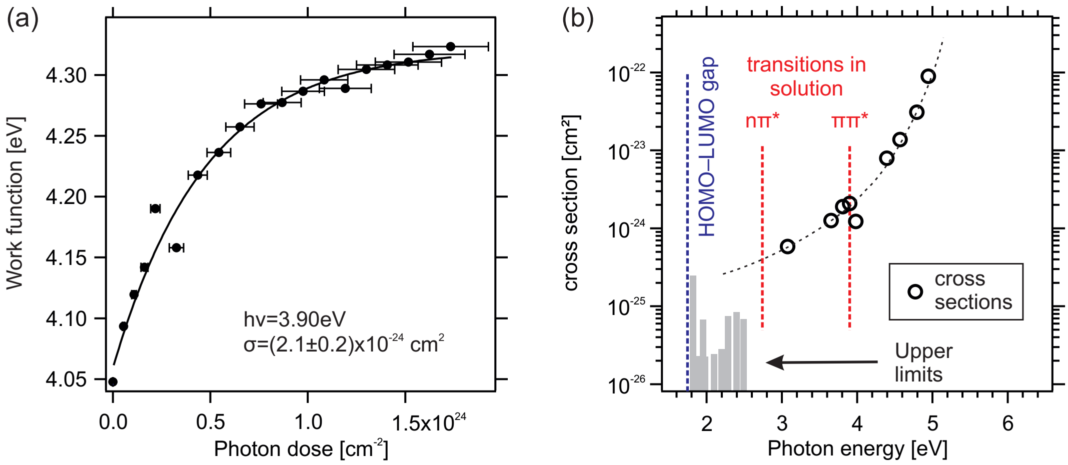

Figure 4.8: (a) Work function change as a function of photon dose during the illumination experiment shown in Fig. 4.6. The data are well described by a mono-exponential function which yields an effective cross section $\sigma = 2.1 \pm 0.2 \times 10^{-24}$ eV. (b) Dependence of the effective cross section σ on the photon energy. The black dashed line is to guide the eye. In the visible spectrum ($h\nu < 3$ eV) no spectral changes can be observed after illumination but upper limits to σ are given as grey bars. The HOMO–LUMO gap as determined from UPS and 2PPE is shown as well as the energies of the $n\pi^*$ and $\pi\pi^*$ transitions of DMC in solution [237]. (a) and (b) published in ref. [172].

We have performed illumination experiments like the one presented for $h\nu = 3.90$ eV above for various other photon energies in the visible and in the UV spectrum (see Fig. 4.8b). For photon energies in the visible spectrum (i.e. $h\nu < 3$ eV), no changes can be observed in the spectra. Therefore, upper limits for the effective cross section are stated in this energetic region. In the photon energy regime above 3 eV, we always observe similar spectral changes, particularly a mono-exponential increase of the work function with increasing photon dose. A more than exponential increase of σ with the photon energy can be observed but we do not find particularly increased effective cross sections at the photon energies corresponding to the HOMO–LUMO gap as determined from UPS and 2PPE experiments shown above or at the photon energies corresponding to the $n\pi^*$ and $\pi\pi^*$ absorption bands of DMC in solution, excitation of which leads to an isomerization reaction in the free molecule [237].

The exponential increase of the effective cross section with the photon energy contradicts a process induced thermally by the deposited energy of the laser beam because this would be reflected in a linear dependence of the effective cross section on the photon energy. On the other hand, since no intramolecular, resonant transitions can be observed, we conclude that the excitation mechanism which initiates photoisomerization in solution, is quenched

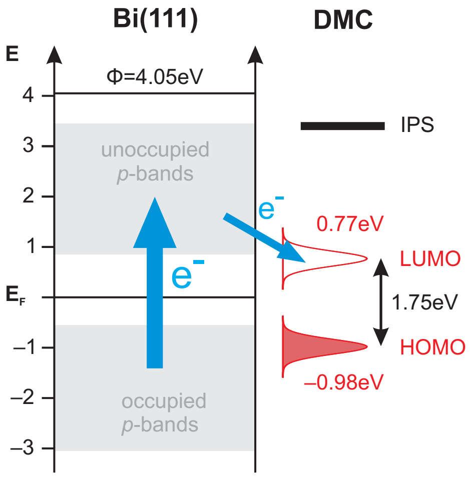

Figure 4.9: Summary of the electronic structure of DMC adsorbed on the Bi(111) surface and proposed excitation mechanism for the photoisomerization process: electrons are excited in the substrate p-bands and subsequently transferred into the LUMO of DMC, creating an anionic resonance of the molecule. Published in ref. [172].

at the surface, possibly due to fast de-excitation of the $S_{1,2}$ states into the substrate or an altered PES of these states due to the adsorbate–substrate interaction. Instead, the broad range of photon energies which lead to the photoisomerization of the adsorbed DMC molecules is indicative of a substrate-mediated process. See sect. 4.1.3 for a discussion of various photoexcitation processes of adsorbate–substrate complexes.

For example, in case of sufficient wave function overlap, a direct electronic transition between the occupied p-bands of Bi and the LUMO of DMC could be induced [236]. However, as can be seen from Fig. 4.9, the limited band width of the substrate bands would only allow for such a transition up to a photon energy of 3.8 eV. Analogously, excitations from the HOMO of DMC to the unoccupied p-bands would energetically only be possible up to a photon energy of 4.4 eV. Since we observe (relatively efficient) photoisomerization well beyond these photon energies, we propose a different substrate-mediated excitation mechanism which is depicted in Fig. 4.9. Absorption of a photon in the substrate leads to an electronic excitation from the occupied to the unoccupied p-bands. The electrons thermalize within the unoccupied p-bands via electron–electron scattering and can subsequently tunnel into the LUMO of DMC, creating an anionic resonance. As discussed in sects. 4.1.1 and 4.1.2, a relatively low activation barrier as well as a stability inversion due to hybridization of the lone pair orbitals at the diazo bridge with the substrate is conceivable in the anionic state of DMC. Consequently, the anionic resonance initiates nuclear motion toward the *cis* conformation.

The energetic alignment of a molecular orbital with the substrate bands has an important influence on photoisomerization reactions which are initiated by the formation of an ionic resonance [115]: if the energetic overlap of the molecular orbital and the bands is too low, charge transfer is inefficient. On the other hand, the excited charge carriers accumulate at the edges of the substrate bands after thermalization (e.g. hot electrons accumulate at the low-energy edge of the unoccupied *p*-bands). If the molecular orbital lies well within the energetic range of the bands, the carrier concentration at the energy of the molecular orbital is too low. Considering the energetic alignment of the frontier orbitals with the respective substrate bands in case of DMC/Bi(111), we conclude that the creation of an anionic resonance is more likely than the formation of a cationic resonance because the HOMO lies well within the range of the occupied *p*-bands.

The mechanism leading to photoisomerization of DMC on Bi(111) is in analogy to that of TBA/Au(111), where a cationic resonance created by hole tunneling into the HOMO of TBA initiates the isomerization process [139, 241].

In summary, we have used complementary surface-sensitive spectroscopies to determine the energetic position of the frontier orbitals with respect to the electronic structure of the underlying Bi(111) substrate. Upon illumination with UV light, the adsorbate molecule performs an isomerization reaction toward the *cis* isomer which is initiated by absorption of a photon in the substrate and subsequent electron tunneling into the LUMO of DMC, leading to an anionic resonance and, ultimately, isomerization. It is noteworthy that the photoisomerization ability of DMC is restored rather than preserved at the surface: while the intramolecular isomerization channel is quenched at the surface, the interplay of substrate and adsorbate allow for a new excitation mechanism.

4.2.2 Photoisomerization of DMC in the Multilayer Regime

Having observed a substrate-mediated photoisomerization reaction in the first layer of DMC-covered Bi(111), we now turn to DMC films in the multilayer regime. These films have been characterized using TPD and Auger electron spectroscopy (AES). The latter was conducted in a different setup with similar facilities for sample preparation and temperature control as in the setup used for 2PPE experiments.

As discussed already in sect. 4.2.1, TPD curves of DMC desorbing from the Bi(111) surface exhibit three desorption peaks which can be attributed to the desorption from the first adsorbate layer (α_1 and α_2) and the multilayer (α_3). Fig. 4.10a shows TPD curves for a variety of prepared DMC films, including those which have been used for the measurements in this section (shown in red). For these preparations, coverages between 3.9 ML and 6.3 ML were obtained with an average of 4.7 ML (inset of Fig. 4.10a).

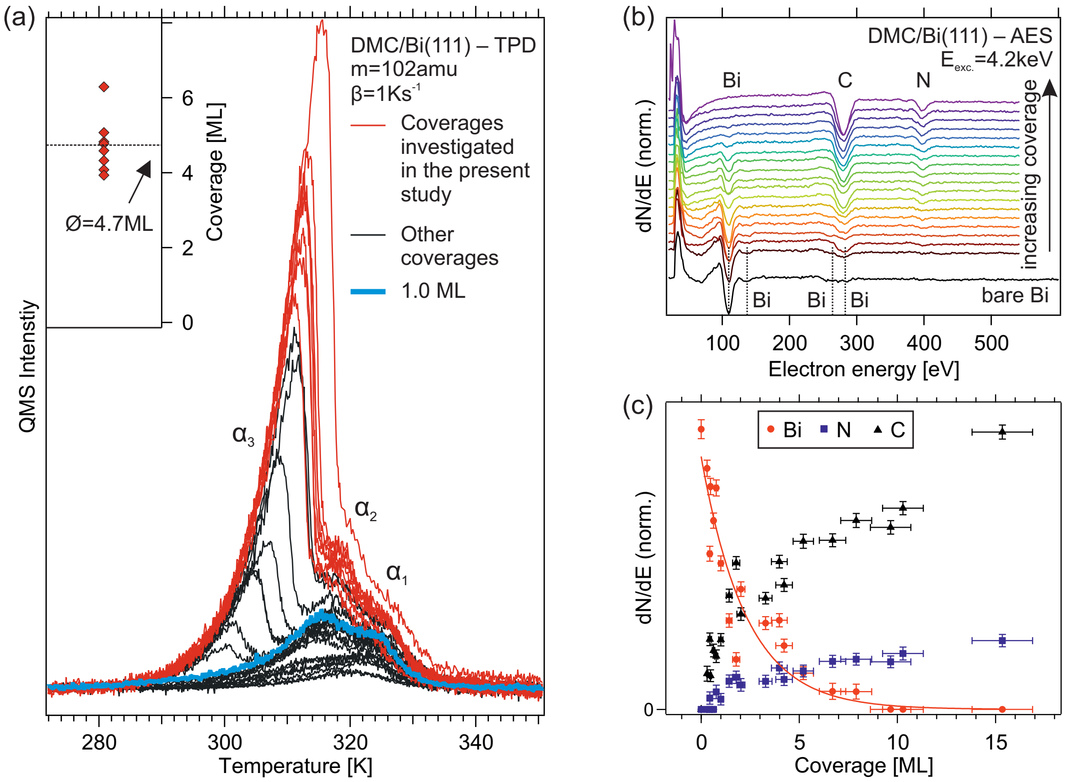

Figure 4.10: (a) TPD curves for different initial DMC coverages on Bi(111) with desorption peaks arising from the first layer ($\alpha_{1,2}$) and the multilayer (α_3). TPD curves shown in red represent preparations which have been used for the measurements in sect. 4.2.2. The TPD shown in blue corresponds to the desorption of 1.0 ML. The inset shows the coverage values for the preparations used for the experiments in this section determined by integration of the red TPD curves. The average coverage was 4.7 ML. A linear background has been subtracted from all TPD. (b) AE spectra recorded for increasing DMC coverages on Bi(111) with an excitation energy of $E_{\text{exc.}} = 4.2$ keV. The spectra were normalized as described in the text. (c) Peak intensity from the data shown in (b) as a function of DMC coverage for Bi (peak at 110 eV), C (283 eV) and N (399 eV). An exponential fit yielding the attenuation length of the Bi peak is shown as a red, solid line.

in [eV]	Bi	Bi	Bi	Bi	C	N	O
experiment	110	137	264	283	283	399	–
literature [242]	101	129	249	268	272	381	510

Table 4.1: AES peak positions for Bi, C, N and O found in our experiments in comparison to literature values.

Generally, adsorbate films can grow in three different modes, named Volmer-Weber (islands), Stransky-Krastanov (wetting layer and islands on top) and Frank-van der Merwe (layer-by-layer). Following the intensities of substrate and adsorbate peaks, respectively, with an element-specific method (e.g. AES) allows to distinguish between Volmer-Weber or Stransky-Krastanov growth on the one hand and Frank-van der Merwe growth on the other hand. Only in the latter case does the intensity of substrate-related peaks vanish completely. In the other growth modes, the surface areas with no or only one adsorbate layer lead to a finite signal intensity of the substrate peaks even at high coverages [243].

In order to characterize the adsorbate films, we recorded an AE spectrum of a freshly prepared Bi(111) surface, then prepared a DMC layer by thermal evaporation and recorded another AE spectrum. After this procedure, a TPD was performed in order to determine the coverage. The intensity of the most prominent Bi peak in the spectra recorded before evaporation was used to normalize the spectra recorded after evaporation with respect to each other. The spectra recorded after evaporation are shown in Fig. 4.10b together with a spectrum of the bare surface which exhibits four features at 110 eV, 137 eV, 264 eV and 283 eV which can all be assigned to Bi (see Tab. 4.1). A constant energy offset of around 10 eV in the measured peak energies is most likely due to the insufficiently calibrated cylindrical mirror analyzer (*Omicron CMA150*).

Upon adsorption of DMC, the Bi peaks lose intensity with increasing coverage while two new peaks appear at 283 eV and 399 eV which can be assigned to C and N, respectively. The respective peak intensities are shown in Fig. 4.10c together with an exponential fit of the Bi peak intensity which yields an attenuation length of 2.3 ± 0.4 ML. The intensity ratio of the adsorbate-induced C and N peaks is independent of the coverage and amounts to $\mathrm{N} : \mathrm{C} = 0.26 \pm 0.03$. Considering the corresponding ratio calculated from the molecular structure of DMC ($4 : 14 = 0.29$) we may conclude that the adsorbate is chemically clean. The fact that the Bi peak is quenched completely at DMC coverages exceeding 10 ML demonstrates a Frank-van der Merwe mode of growth.

Both 2PPE ($h\nu < \Phi$) and UPS ($h\nu > \Phi$) spectra of multilayer DMC on Bi(111) do not show any features. However, similarly to the first monolayer we can use the work function as a measure for the light-induced changes, which are observed in this coverage regime as well. Fig. 4.11a shows an illumination experiment in which photoemission spectra were recorded in between phases of illumination with the same laser beam[4]. An increase of the work function by around 500 meV is observed, at much lower photon dose than that required to

---

[4] During illumination, the beam intensity was increased such that spectroscopy is no longer feasible due to space charge effects.

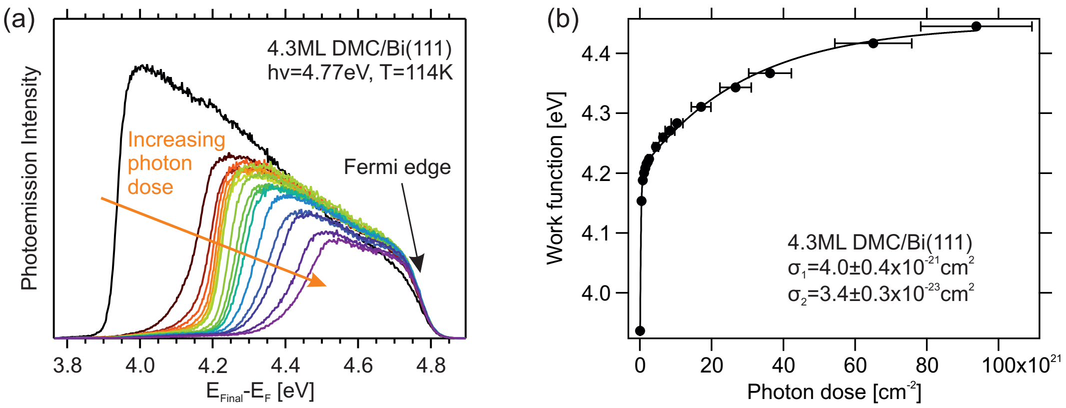

Figure 4.11: (a) Photoemission spectra of multilayer DMC on Bi(111) recorded during illumination of the sample with the same laser beam. The secondary edge shifts to higher energies with rising photon dose. (b) Work function change as a function of photon dose for the experiment shown in (a). The photon fluence was $3.2 \pm 0.6 \times 10^{19}$ $\text{cm}^{-2}\text{s}^{-1}$. The data have been fitted with a bi-exponential function yielding two effective cross sections $\sigma_{1,2}$ (see text).

bring the molecules in the first layer into saturation. Fig. 4.11b shows that the work function change in this experiment does not follow a simple exponential behavior but can only be described with a bi-exponential function, as the one in eq. 3.6, which indicates two different photo-induced processes. The two effective cross sections obtained from the fit, $\sigma_1 = 4.0 \pm 0.4 \times 10^{-21}$ cm^2 and $\sigma_2 = 3.4 \pm 0.3 \times 10^{-23}$ cm^2, are a measure for the efficiency of the reactions, similarly to the effective cross section of the photoisomerization in the first layer.

The occurrence of two different processes with different efficiencies is also reflected in the changing shape of the secondary edge. At low photon doses, a broadening of the secondary edge can be observed simultaneously to its shift toward higher energies. When the work function reaches values of around 4.2 eV, the secondary edge becomes narrower again but subsequently broadens again. The reason for this behavior lies in the inhomogeneity of the laser spot which is less intense in the periphery than in its center [244]. Consequently, a light-induced process occurs faster in the center. Once the reaction in the corresponding sample areas, which have been exposed to a higher photon dose, reaches saturation, the molecules in the periphery of the laser spot can “catch up” which leads to the intermediate narrowing of the secondary edge. The same phenomenon then occurs again for the less efficient reaction with the lower effective cross section.

Illumination experiments similar to the one described above have been conducted for various photon energies in the visible and UV spectral region. In

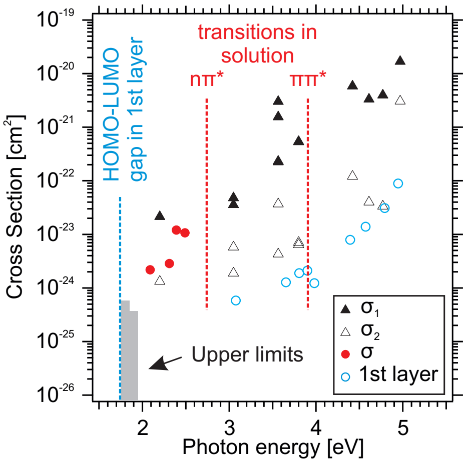

Figure 4.12: Effective cross sections σ_1 and σ_2 observed in the multilayer as function of photon energy. For some photon energies, the work function is described by only one effective cross section σ. The effective cross section of the photoisomerization reaction in the first monolayer is shown as blue, open circles. Dashed lines represent the HOMO–LUMO gap as determined in sect. 4.2.1 for the first monolayer and the energies of the $n\pi^*$ and $\pi\pi^*$ transitions of DMC in solution [237]. For photon energies below 2 eV, no reaction can be observed and therefore upper limits to the effective cross section are given as grey bars.

most cases a work function increase could be observed in the UPS or 2PPE spectra. However, illumination did not affect the sample at photon energies below 2 eV, for which we can only give upper cross section limits. The work function increase at higher photon energies could be fitted with a bi-exponential function, as described above, except for four photon energies in the visible spectrum, where the work function behaves according to a mono-exponential function, resulting in a single effective cross section σ.

The photon energy dependence of the different effective cross sections is shown in Fig. 4.12. Both σ_1 and σ_2 increase in the same, exponential manner with rising photon energy, similar to the behavior in the first monolayer. This is an indication that the processes in the multilayer are mediated by the substrate, too, and that thermally induced reactions (heating of the sample by the deposited laser power) can be ruled out. Furthermore, intramolecular excitations appear to be quenched even in the multilayer, as evident from the absence of a resonant enhancement of the effective cross section near the $n\pi^*$ and $\pi\pi^*$ transitions of the free molecule, respectively.

σ_1 is around two orders of magnitude larger than σ_2 over the entire spectral range for which both reactions are observed. The less efficient process has an effective cross section which is comparable to that of the photoisomerization in the first monolayer. Due to the limited photon dose which can be applied under the given experimental conditions, we are limited to the detection of effective cross sections below approximately 10^{-24} cm^2 (this value varies for different photon energies). The work function change at lower photon energies can be described by a mono-exponential function because in these cases, the inefficient photo-induced process probably falls below the detection limit.

To summarize the above findings, two processes occur in the multilayer which are mediated by the substrate, not thermally induced, and have an exponential dependence of the respective effective cross section over a wide range of photon energies, similar to the photoisomerization in the first monolayer. The cross section of the less efficient process is even on the same order of magnitude as the corresponding quantity which describes isomerization in the first layer. Due to these similarities as well as the results of the thermally induced reactions of the photo-product (see sec. 4.2.3) we assign the processes in the multilayer to *trans–cis* photoisomerization reactions. Indeed, light-induced changes of molecular conformation is not uncommon in the multilayer regime of adsorbed photoswitches due to the high degree of decoupling from the substrate [113, 121, 122, 123].

DMC molecules occur in three inequivalent locations within the multilayer film, namely at the substrate–adsorbate interface, in the bulk multilayer and at the adsorbate–vacuum interface. It is conceivable that the effective photoisomerization cross section differs for molecules situated in these different locations and it is thus very likely that the two photoisomerization processes observed here are due to the different molecular environment. While steric effects should of course strongly influence the conformational changes in the buried layers, one should keep in mind that photo-induced *trans–cis* isomerization can even be observed in bulk azobenzene [125].

The different molecular environments have several effects on the efficiency of the substrate-mediated photoisomerization reaction. On the one hand, the tunneling probability for charge transfer into the adsorbate decreases exponentially with increasing molecule–substrate distance, thereby reducing the effective cross section. On the other hand, molecules in the topmost layer, at the vacuum interface, should experience less steric hindrance, which increases the effective cross section. Due to these two competing effects, one can not say whether photoisomerization is more or less efficient in a given molecular environment and therefore we can not assign the two different effective cross sections to a specific location within the multilayer film.

In this section we have investigated multilayer DMC films on Bi(111). We found that the films grow in a Frank-van der Merwe mode and that the molecules undergo photo-induced *trans–cis* reactions with an effective cross section that depends on the molecular environment, i.e. the location of the molecule within the film. Surprisingly, both processes are mediated by the substrate similar to the photoisomerization in the first monolayer.

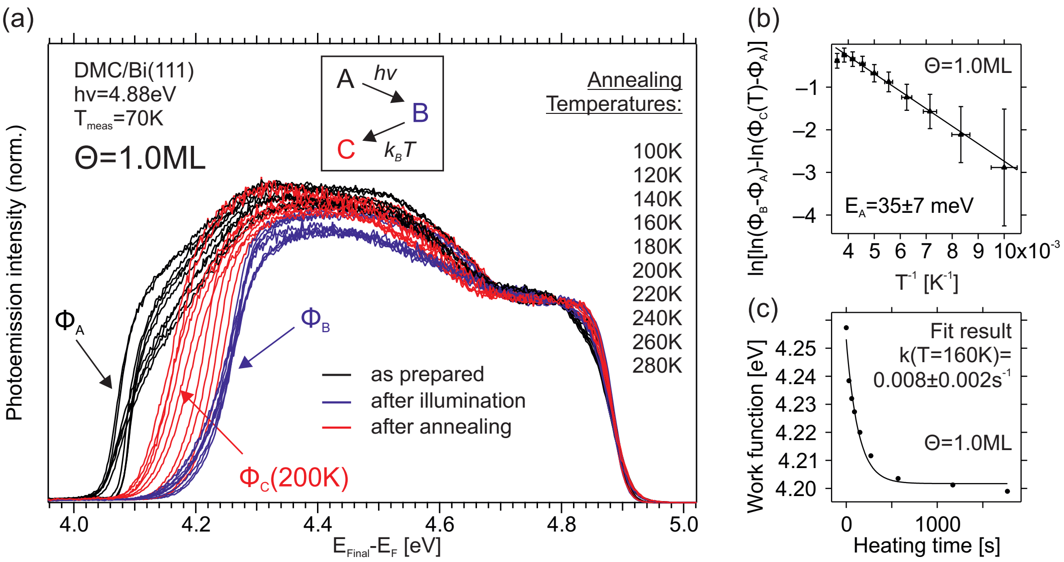

Figure 4.13: (a) Photoemission spectra of 1.0 ML DMC on Bi(111) directly after preparation (black), after illumination (blue) and after subsequent annealing to the temperatures given in the figure (red, 5 min). The experimental procedure is shown schematically in the inset. The spectra were normalized to a region around 4.7 eV and all spectra were measured at 70 K. (b) Arrhenius plot for the data shown in (a). A quantity representative of the thermally induced changes is plotted over the inverse annealing temperature. A linear fit yields the activation barrier, E_A, of the observed process. (c) Work function change as a function of heating time at 160 K. A fit according to eq. 4.2 yields the rate constant at this temperature.

4.2.3 Thermally Induced Reactions of Adsorbed DMC

In this section we will discuss the effect of annealing on the *cis* isomers which are obtained after the photoisomerization reactions of the first monolayer and the multilayer, respectively. We will mainly discuss the thermally induced process found in the first monolayer and then briefly compare the result with a very similar experiment conducted for multilayer DMC. Generally, annealing the adsorbate after photoisomerization leads to a decrease of the work function.

For the following experiments, a monolayer of DMC was prepared and the sample was annealed at 240 K for 30 min which allows to unambiguously assign any thermally induced changes after illumination to the *cis* isomers. We define the situation after this initial annealing, in which all DMC molecules have *trans* configuration, as state A. Before the procedure described in the following, which was conducted for every annealing temperature, we always recorded a UPS spectrum of the respective, new spot in state A first (black spectra in Fig. 4.13a). In order to quantitatively investigate the effect of annealing on the *cis* isomers according to Arrhenius, we have to bring the adsorbate into a well-defined state with a certain concentration of *cis* isomers for every annealing step. Due to the low effective cross section of the photoisomerization reaction, bringing the system into saturation is not practically feasible for the following experiment. Instead, we have prepared a well-defined state (henceforth referred to as state B) by exposing the sample to a photon dose of 1×10^{23} cm^{-2} at a photon energy of 4.88 eV, using the same laser beam as for recording the UPS spectra, and subsequently verifying that state B was actually reached by recording a photoemission spectrum (blue spectra). Then, the sample was annealed at a specific temperature between 100 K and 280 K for 5 min and a third spectrum was recorded in this annealed state C (red spectra).

After the annealing step, the work function is reduced, compared to state B. In the following, we will assume a linear relation between the work function change relative to state A and the concentration of *cis* isomers ($[cis]$) on the surface, $[cis] \propto \Phi_\mathrm{C}(T) - \Phi_\mathrm{A}$. In a first-order reaction *cis* → *trans*, the time-dependent concentration of *cis* isomers is

$$[cis] = [cis]_0 \exp(-kt). \tag{4.2}$$

The rate constant is temperature-dependent, as described by the following Arrhenius expression:

$$k(T) = k_0 \exp\left(-\frac{E_\mathrm{A}}{k_\mathrm{B}T}\right) \tag{4.3}$$

Here, k_0 is the pre-exponential factor (or attempt frequency) and E_A denotes the activation energy. By inserting eq. 4.3 into eq. 4.2, the following expression is obtained which describes the temperature dependence of $\Phi_\mathrm{C}(T)$.

$$\ln\left[\ln\left(\Phi_\mathrm{B} - \Phi_\mathrm{A}\right) - \ln\left(\Phi_\mathrm{C}(T) - \Phi_\mathrm{A}\right)\right] = -\frac{E_\mathrm{A}}{k_\mathrm{B}T} + const. \tag{4.4}$$

Fig. 4.13b displays the work function measured after annealing, $\Phi_\mathrm{C}(T)$, in the form of eq. 4.4 as a function of the inverse temperature. From a linear fit we thus obtain the activation energy $E_\mathrm{A} = 35 \pm 7$ meV. Note, that the work function obtained after annealing at 280 K is higher than the one after annealing at 260 K which is due to partial desorption (see Fig. 4.4).

Another interesting observation in Fig. 4.13a is that the work function of the all-*trans* sample (state A) is never fully restored. This is also the case for longer annealing times. This observation indicates that the thermally induced process investigated here is not due to a thermal *cis*–*trans* isomerization in the molecular ground state as it occurs in the free molecule.

Using a modified experimental procedure, we can furthermore determine the attempt frequency k_0. To that end, state B was prepared as described above and the work function was measured. Then, the sample was annealed at 160 K for a certain heating time and subsequently the work function was measured (at 115 K). Further cycles of annealing and measuring eventually yield the *cis* concentration (in the form of the work function change) as a function of time. This relation is described in eq. 4.2 and indeed, the data follow a first order behavior, as seen in Fig. 4.13c. From an exponential fit, the rate constant at 160 K is obtained as $k(160 \text{ K}) = 0.008 \pm 0.002 \text{ s}^{-1}$. Using eq. 4.3 and the above measured activation energy, we obtain an attempt frequency of $k_0 = 0.10 \pm 0.06 \text{ s}^{-1}$.

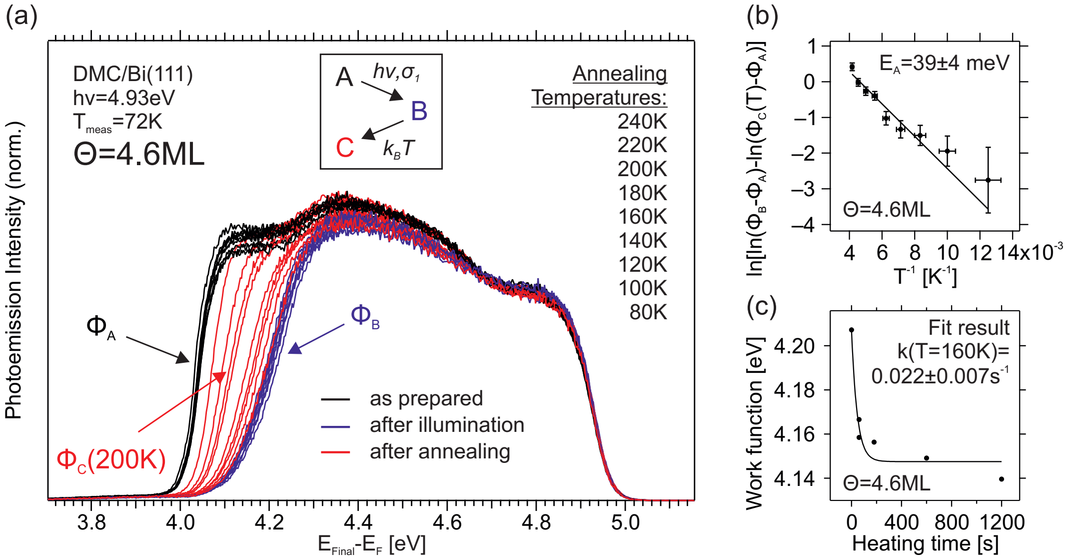

Figure 4.14: (a) Photoemission spectra of multilayer DMC on Bi(111) directly after preparation (black), after illumination (blue) and after subsequent annealing to the temperatures given in the figure (red, 5 min). The experimental procedure is shown schematically in the inset. The spectra were normalized to a region around 4.7 eV and all spectra were measured at 72 K. (b) Arrhenius plot for the data shown in (a). A quantity representative of the thermally induced changes is plotted over the inverse annealing temperature. A linear fit yields the activation barrier, E_A, of the observed process. (c) Work function change as a function of heating time at 160 K. A fit according to eq. 4.2 yields the rate constant at this temperature.

For comparison, the same experiment was conducted for a multilayer of DMC (4.6 ML, see Fig. 4.14). Unlike in other multilayer experiments we annealed the multilayer film at 240 K for 30 min before illumination, as for the monolayer. The state B, into which the multilayer phase was brought by illumination with a photon dose of 2.6×10^{21} cm^{-2} was such that the efficient photoisomerization reaction characterized by σ_1 has saturated to a large extent but the much less efficient reaction described by σ_2 has had little effect on the sample. The work function decreases upon annealing, too, and the resulting parameters of the thermal reaction in the multilayer are very similar to the first layer, namely $E'_{\mathrm{A}} = 39 \pm 4$ meV and $k'_0 = 0.37 \pm 0.16\ \mathrm{s}^{-1}$ (calculated from the rate constant at 160 K, $k'(160\ \mathrm{K}) = 0.022 \pm 0.007\ \mathrm{s}^{-1}$). The values for the activation energy are identical in the two coverage regimes and the attempt frequencies are on the same order of magnitude.

Due to the aforementioned agreement between the results for the two coverage regimes, we may conclude that both thermally induced reactions are in fact the same. Furthermore, in the first monolayer we know that the thermal process occurs only for the *cis* isomers (because of the initial annealing at 240 K for 30 min). In the multilayer on the other hand, the thermal reaction can be attributed mainly to the photo-product of the efficient reaction described by σ_1 which has been assigned to a photoisomerization as well. This assignment is now supported due to the fact that the photo-product of this reaction undergoes the same thermally induced reaction as the *cis* isomers in the first monolayer.

Concerning the nature of the observed thermal process, we have already noted that a *cis–trans* reaction along the PES of the molecular ground state which is observed in the free molecule, is not consistent with the observation that the work function of the all-*trans* sample can not be observed after annealing of the *cis* isomers. Furthermore, the observed activation energy of $E_{\mathrm{A}} = 35 \pm 7$ meV is very low compared to the activation barrier for the *trans–cis* isomerization of TBA (i) on the Au(111) surface, which amounts to 240 ± 30 meV, or (ii) in solution where it has a value of 1.01 ± 0.03 eV [245]. DFT calculations predict the activation barrier for free DMC (TBA) to be 1.03 eV (1.39 eV) [109]. The activation barrier for the thermally induced ring-opening reaction of a spiropyran adsorbed on the Au(111) surface has been measured as 840 ± 50 meV [92]. Isomerization of an imine derivative on Au(111) exhibits an activation barrier of 0.6 ± 0.1 eV [246]. We may thus conclude that the thermally induced process observed in different coverage regimes of DMC on Bi(111) is not due to an isomerization reaction.

As shown in Fig. 4.2a, DMC occurs in two different rotamers, *syn* and *anti*. Interconversion between these two forms requires only a rotation around a σ bond which can be assumed to have a much lower activation barrier than an isomerization during which the double bond of the diazo bridge has to be broken. When DMC is adsorbed in the flat *trans* geometry, the surface poses an additional steric barrier for the phenyl ring rotation around the σ-bond. However, in the *cis* isomer, at least one of the phenyl rings can be expected to be tilted out of the surface plane and therefore, the steric hindrance due to the substrate should be lower for this isomer. Calculations for a phenyl ring rotation around a σ-bond for a comparable molecule predict an activation barrier of 37 meV for the isolated molecule [247]. This value is identical to the activation barrier observed in our experiments. Nevertheless, it is important to note that the calculations have been performed for a free molecule.

In the *trans–cis* photoisomerization, the work function increases which is consistent with the cyano groups pointing toward the vacuum side in the *cis* conformation. The work function shift toward lower values (rather than higher ones) in the annealing experiments on the other hand is consistent with a rotation of a phenyl ring in which one electronegative cyano group changes its orientation toward the surface, thus a *syn–anti* reaction.

The attempt frequency observed both in the multilayer and the monolayer regime is very low. For comparison, the corresponding value for the thermally induced *cis–trans* isomerization of TBA/Au(111) is $10^{6\pm1}$ s^{-1} [245]. For TBA in solution, this value even amounts to 1.6×10^{10} s^{-1}. If we consider the above proposed phenyl ring rotation in the *cis* form of DMC, the potential energy surface along the rotational coordinate around the σ-bond can be expected to be rather flat. In such a shallow potential minimum, the vibrational frequency would be relatively low which might explain the small attempt frequency observed in experiment. For comparison, the attempt frequency for a phenyl ring rotation of a comparable molecule on a surface is 10^6 s^{-1}. However, in this case, the phenyl ring is adsorbed in a rather flat geometry and thus the steric hindrance due to the underlying substrate can be expected to be higher than for *cis*-DMC, resulting in a higher vibrational frequency.

In conclusion, a thermally induced reaction of the *cis* isomers of DMC is observed both in the monolayer and the multilayer regime. The activation energy is relatively low, as is the attempt frequency. Since we can rule out a thermally induced *cis–trans* reaction to be the underlying process, we propose a phenyl ring rotation which is consistent with the kinetic parameters that we obtain in experiment.

4.3 Summary: DMC

In this chapter we have discussed the results of photoemission and 2PPE experiments on DMC adsorbed on Bi(111) which reveal photoisomerization reactions in the first and higher lying layers as well as a thermally induced reaction of the *cis* isomer.

Using both UPS and 2PPE, we were able to observe the frontier orbitals of DMC on the Bi(111) surface as well as an IPS. With increasing photon dose, the spectra change due to *trans–cis* isomerization which changes the surface dipole moment and thus the work function. By quantifying this process for various excitation photon energies, we conclude to a substrate-mediated excitation pathway in which a transient anionic resonance of DMC is created which lowers the barrier for the isomerization and possibly stabilizes the *cis* isomer. We do not observe a back-reaction toward the *trans* form induced with either light or thermal activation.

Using AES we determined that DMC grows in a Frank-van der Merwe (layer-by-layer) mode. The multilayer therefore has three inequivalent molecular environments: the substrate–adsorbate interface, the bulk multilayer and the adsorbate–vacuum interface. Illumination of a DMC multilayer leads to changes of the work function which are governed by two different photoisomerization reactions with different effective cross sections, most likely due to different molecular environments. As in the first monolayer, the photon energy dependence of the effective cross sections reveals a substrate-mediated process while the intramolecular excitation pathway is quenched.

In both coverage regimes, thermal activation of the photo-produced *cis*-isomers leads to a work function change which was used to quantify the reactions according to Arrhenius. Since the kinetic parameters in the first monolayer and the multilayer are very similar, we conclude that the same reaction occurs in both regimes. A thermally induced *trans*–*cis* reaction is highly unlikely and instead we propose a rotation of cyano-substituted phenyl rings around the σ-bond to the diazo group to be the underlying process.

Chapter 5

Conclusion

As outlined in the introduction, generally two different approaches to the present day challenges of nanotechnology have been followed in this thesis: (i) on the one hand, we have investigated graphene nanostructures, the interesting properties of which are governed by the unique properties of a delocalized two-dimensional electronic system of massless charge carriers. (ii) On the other hand, the second, conceptually different strategy for the development of nanoscale devices is the use of functional single molecules, i.e. molecular switches.

In the first part of this thesis, we followed the graphene nanostructure approach by investigating the electronic properties and the synthesis of two different graphene nanoribbons (GNR), a straight armchair GNR (AGNR) and a chevron-shaped GNR (CGNR) which were fabricated in a thermally induced bottom-up on-surface synthesis reaction.

One goal of this thesis was to investigate the thermally-induced reaction by following different reaction products in temperature-programmed desorption and particularly to shed light on the reaction pathway of Br after dehalogenation. Studying the thermal synthesis of the AGNR on the Au(111) surface we found that the Br substituents are bound to the surface until they are associatively desorbed in the form of HBr during the cyclodehydrogenation reaction, the final reaction step of the on-surface synthesis, which provides the necessary H. Furthermore, we can not exclude that the adsorbed atomic Br participates in the cyclodehydrogenation reaction, e.g. by catalyzing C–H dissociation. Surprisingly, Br is not present in the higher layers of adsorbed precursor molecule films which raises the question how the corresponding multilayers are structured. Altogether, the low interest that the pathway of the Br substituents after dehalogenation have received previously, may not have been adequate.

We used 2PPE to study the electronic structure of the various reaction intermediates (the adsorbed molecular precursors, the polyanthrylene and the AGNR) and we were particularly interested in the band gap of the systems. A comparative analysis of the electronic structure of the intermediate polyanthrylene, which occurs in the thermal on-surface synthesis, and the eventually formed AGNR reveals insight into the respective electronic systems. The electronic coupling between the π systems of neighboring anthracene units in the polyanthrylene leads to the formation of a one-dimensional band structure, particularly in the distorted geometry of the adsorbed form. However, the band gap of the AGNR is by a factor of two smaller (2.60 eV) than that of the intermediate polyanthrylene which we attribute to the fundamentally different nature of the electronic system of the fully conjugated graphene nanostructure. Additionally, it leads to the formation of edge states at the zigzag-shaped ends of the AGNR.

Photo-induced assembly of GNR from molecular precursors would offer exciting opportunities for the fabrication of GNR devices because it would combine the atomic precision of bottom-up on-surface synthesis with the ability to control the nanostructures on a mesoscopic scale, as in lithography. One objective of this work was to induce such a photo-induced synthesis reaction of the adsorbed monomers. By illuminating the precursors with UV light, we indeed observe dehalogenation and covalent coupling due to a non-thermal process which is initiated by electronic excitation in the substrate bands followed by charge transfer into unoccupied electronic states of the adsorbate.

Besides parameters such as the width and the chirality of GNR, which influence the electronic structure of GNR, doping with N atoms is another approach to tailor their properties. Using electron spectroscopies, we wanted to investigate the effect of precursor N substitution on the size of the band gap as well as its alignment with the electronic structure of the environment, i.e. the underlying substrate. We found that substitution of the precursor molecules allows doping of CGNR with well-defined dopant sites and concentrations which does not affect the thermal on-surface synthesis and leads to n-doping of the electronic system without affecting the size of the band gap.

The second part of this work was motivated by the second major development strategy toward nanotechnological systems. Specifically, we have studied the interaction of a photochromic molecular switch, di-meta-cyano-azobenzene, with a semi-metallic Bi(111) surface and particularly the switching capability of this system. We chose both the azobenzene derivative as well as the substrate due to their properties which were supposed to foster the photoisomerization ability. In order to investigate whether this goal was achieved, we used different photoemission techniques to follow the light-induced changes of DMC both in the first and in the higher lying layers.

Unlike several other systems of molecular switches which are directly adsorbed on a metallic substrate, the molecules in the present system are able to perform photoisomerization reactions both in direct contact with the surface and in the multilayer regime. However, the mechanism governing these conformational changes is fundamentally different compared to the intramolecular excitation pathway of the isolated molecule. In the adsorbed state, this intramolecular pathway is quenched, but the substrate acts as a chromophore instead. Absorption of light in the Bi p-bands creates hot electrons, some of which tunnel into the LUMO of the adsorbate molecule. Relaxation along the potential energy surface of this anionic resonance subsequently leads to a *trans–cis* isomerization. The activation barrier for this isomerization in the anionic state is reduced due to substitution with electronegative cyano groups of the azobenzene and possibly hybridization with the substrate bands.

The energetic overlap between the molecular orbitals and the substrate bands, which we have investigated with spectroscopic methods, is crucial for the substrate-mediated process. When this electronic substrate–adsorbate interaction is taken into account, the need for electronic decoupling of the photochromic center of the molecule from the underlying substrate becomes obsolete.

Since the isomerization reaction of azobenzene in solution is reversible with light and thermal activation, we investigated this capability also for the adsorbed DMC on Bi(111). Unlike in other systems, the *cis* isomers can not be converted back to the *trans* form. However, thermally activated processes are observed for the *cis* isomers both in the first monolayer and higher lying layers. The reaction is the same in both coverage regimes and can not be attributed to a *cis–trans* isomerization. Instead we propose the rotation of a phenyl ring in the three-dimensional *cis* form.

Overall, the broad range of reactions that we observe for large organic molecules adsorbed on surfaces in this thesis demonstrates that the surface has the potential to not only provide the bedrock for chemical reactions and molecular function but that the electronic structure of the substrate can play a central role in surface photochemistry of large molecular building blocks with exciting possibilities for the assembly of functional nanostructures.

The results of this work provide grounds for further interesting studies on nanoscale materials. For example, the perspective of photo-induced on-surface synthesis of GNR is very tempting. Instead of the dimerization which was achieved here, fabrication of extended GNR structures with light could be investigated on different metal and semiconductor surfaces, possibly with different halogen substituents. Concerning the photoisomerization ability of adsorbed molecular switches, the crucial balance of covalent and van der Waals interaction between the molecule and the underlying substrate, which we tried to meet with the semi-metal bismuth in this work, could possibly be achieved with a graphene substrate as well. Experiments with switching molecules adsorbed particularly on surface-fabricated GNR could enable bi-directional isomerization due to the band gap which can be expected not to lead to efficient de-excitation of excited molecular states on the potential energy surface of which the conformation changes occur in the free molecule.

Appendix A

AGNR: Xe Adsorbed on Clean and AGNR-Covered Au(111)

In order to roughly estimate the coverage of AGNR on the Au(111) surface after the thermal fabrication of the AGNR, we co-adsorbed Xe from a dosing valve while the sample was positioned in front of the TOF spectrometer. The respective dosing experiment is shown in Fig. 3.16a,b. After exposure of the sample to 116 L, a TPD was recorded which shows two broad desorption peaks between 67 K and 90 K (see Fig. A.1). The high-temperature peak α_{Au} is also observed when Xe is desorbed from the bare Au(111) surface, unlike the low-temperature peak α_{AGNR}, which only occurs in the presence of the AGNR. Interestingly, α_{Au} saturates before α_{AGNR}, indicating a lower sticking coefficient of Xe on the graphene structure which is probably due to the lower polarizability. At even lower temperatures, two peaks can be observed which are associated with desorption from the multilayer, both on the AGNR-covered areas and the initially clean surface areas. From the integrated TPD, the ratio

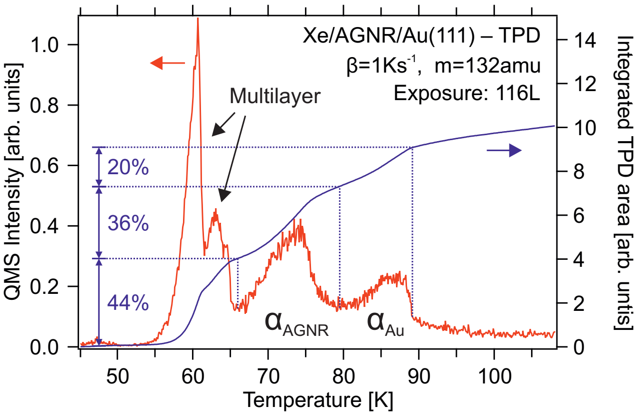

Figure A.1: TPD curve of Xe/AGNR/Au(111) recorded after co-adsorption of Xe on a surface covered with the thermally produced AGNR. This TPD has been recorded after the dosing experiment shown in Fig. 3.16a,b. The integrated signal is shown in blue on the right axis and the relative areas of the observed peaks are given in percent of the total area.

of Xe adsorbed on AGNR/Au(111) to the overall Xe coverage in the first layer can be determined as $\frac{36}{36+20} = 64\%$. However, due to different packing densities and a relatively strong, non-linear background, the resulting AGNR coverage is only an estimate.

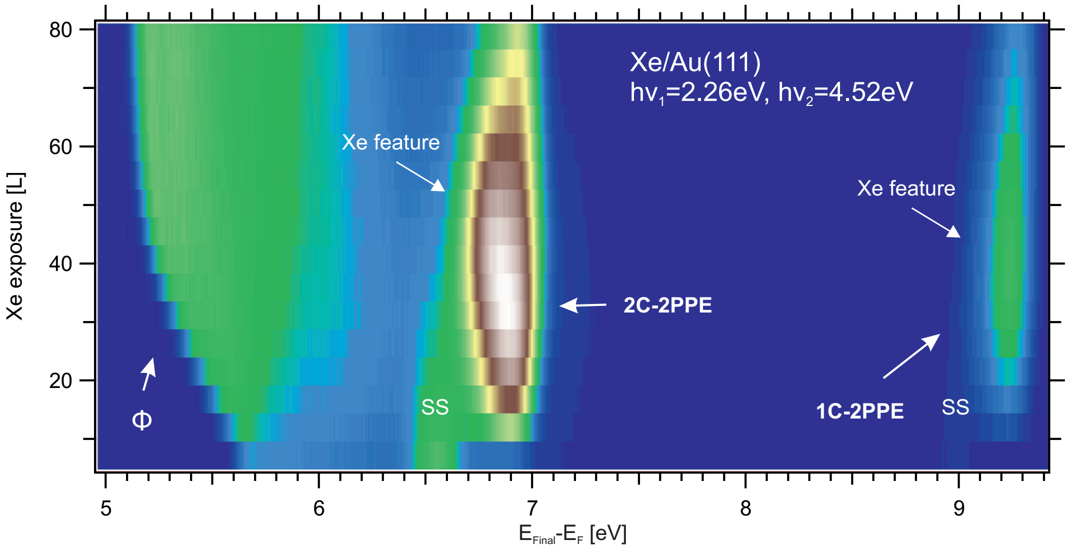

Figure A.2: Continuous 2C-2PPE experiment (without background subtraction) during Xe adsorption. The false color plot indicated 2PPE intensity (blue: low, white: high).

As a control experiment for the Xe co-adsorption experiments presented in sect. 3.2.4, we performed the same measurement without adsorbed GNR. Fig. A.2 shows a false color plot depicting continuously acquired 2C-2PPE spectra while dosing Xe via the background pressure. Note, that the 1C-2PPE background of the UV beam ($h\nu_2$) was not subtracted from the signal and consequently, the spectra show features of the 2C-2PPE signal and the 1C-2PPE signal, as indicated. With increasing Xe exposure, the work function Φ decreases continuously until it saturates after an exposure of around 60 L at a value which is 0.5 eV lower. In the initial spectrum, the surface state of Au(111) is a prominent feature which is quickly quenched. At the same time, a new and intense peak associated with the Xe overlayer arises both in the 1C- and 2C-2PPE spectrum.

Appendix B

AGNR: Comparison of 2C- and 1C-2PPE Spectra

In the 1C-2PPE spectra shown in sect. 3.2.4, the IPS and the CB+n were assigned to unoccupied electronic states based on the fact that their relative energetic position to the Fermi edge is not independent of the photon energy. This observation would however also be consistent with one or both of the peaks arising from an electronic final state which is energetically located above the vacuum level. Fig. B.1 shows a series of 1C-2PPE spectra similar to those shown in Fig. 3.14a. The IPS and the CB+n can be observed at final state energies between 8.0 eV and 9.5 eV. In addition to these spectra, 2C-2PPE spectra recorded in the same series are overlaid (red lines). These 2C-2PPE spectra have been energetically offset by $h\nu_1$ which results in an overlap of peaks arising from occupied states (as well as the Fermi edge) and unoccupied states which are pumped with the UV pulse ($h\nu_2$). In contrast, states populated with the other laser pulse in 2C-2PPE ($h\nu_1$) or final states would not overlap. As we can see, the peaks associated with the IPS and the CB+n overlap with their counterparts in the 1C-2PPE spectra. Since both could already be ruled out to be occupied electronic states, they must hence be unoccupied but not final states. The third feature observable in the 2C-2PPE spectra is due to the conduction band (CB), which is populated with $h\nu_1$ and probed with $h\nu_2$ here.

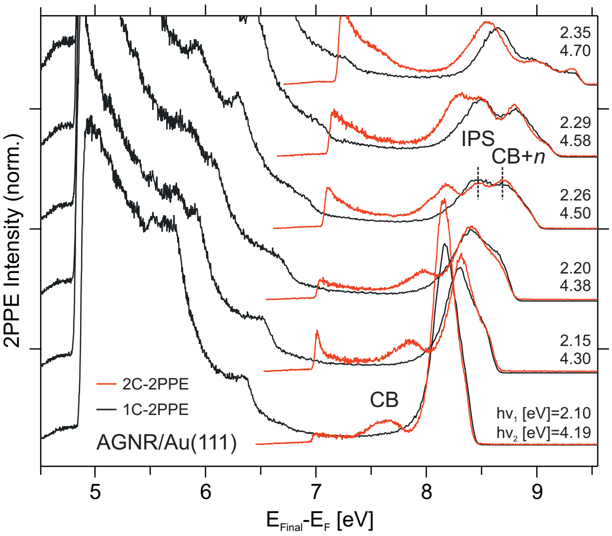

Figure B.1: Comparison of 1C-2PPE (using $h\nu_2$ only) and 2C-2PPE spectra of AGNR on the Au(111) surface recorded for various photon energies. The 1C spectra were normalized to one of the *d*-band features, the 2C spectra were normalized to the region with slightly lower energy than the CB. The 2C-2PPE spectra were offset toward higher values on the energy scale by an energy corresponding to $h\nu_1$.

Appendix C

AGNR: Dynamics of Unoccupied States Measured with Time-Resolved 2PPE

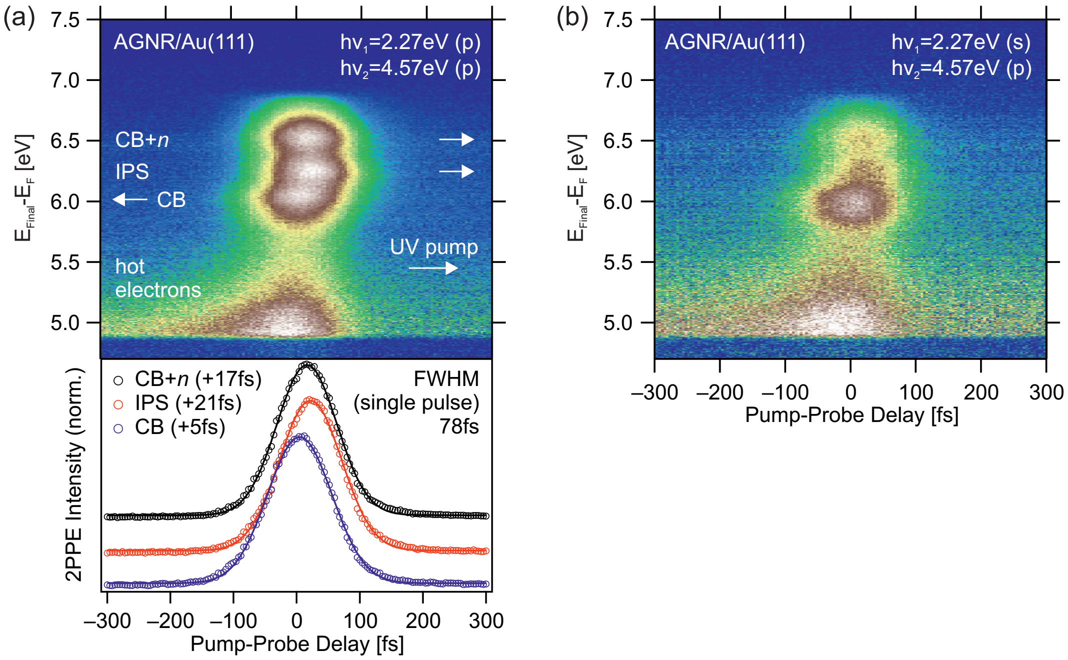

Figure C.1: (a) Time-resolved 2PPE experiment of the AGNR on Au(111). Both beams were p-polarized. The color code represents the 2PPE intensity (blue: low, white: high). Arrows indicate toward which delay values an asymmetry would be expected. The bottom graph shows cross-correlation traces for the three observed states. The values given in the legend are the relative peak shift. (b) Same experiment as in (a) but here the visible beam is s-polarized.

We used time-resolved 2PPE (TR-2PPE) to investigate the ultrafast dynamics of the three unoccupied states of the AGNR on Au(111) which are found in 2PPE. Fig. C.1a shows a TR-2PPE experiment conducted with both beams in p-polarized configuration. The peaks corresponding to the IPS and the CB+n are probed with visible light ($h\nu_1$) at positive delays in this 2C-2PPE experiment. The CB is probed with UV light ($h\nu_2$). As evident from the three cross-correlation traces, none of the states exhibits a lifetime which can be resolved in this experiment. However, the maxima of all three cross-correlation traces show a shift toward higher delays, as indicated in the figure. The fact that the CB peak has a positive peak shift value is not realistic. The reason for this unrealistic behavior is that there is no energetic region where only occupied states contribute to the signal and where a pure cross-correlation of the two laser pulses could be measured. Therefore, the shifts of the peak maxima can only be interpreted relative to each other. The temporal pulse width (full width at half maximum, FWHM) was 78 fs in this experiment.

Fig. C.1b shows the same experiment as discussed above, but the visible laser beam was s-polarized, which changes the intensities of the peaks according to the orientation of the respective transition dipole moments. Both the IPS and CB+n peak lose intensity which indicates that the respective transition dipole moments are oriented perpendicular to the surface plane. In contrast, the transition dipole moment associated with the CB seems to be oriented in the surface plane.

Appendix D

DBBA: 2PPE Intensity Change of Individual Molecular Orbitals During Photo-Coupling

In sect. 3.2.5 we have discussed the effect of illumination on the features observed in the 2PPE spectra of DBBA/Au(111). The 1C-2PPE spectrum shown there was recorded using a relatively high photon energy and allows simultaneous analysis of both IPS and a resonance feature in which the peaks associated with the three observed molecular orbitals are all comprised. However, due to the overlap of the three molecular features, their individual behavior during the photo-coupling reaction can not be studied at this photon energy.

Fig. D.1 shows another illumination experiment of 1 ML DBBA/Au(111), recorded with a lower photon energy of 4.01 eV. At this energy, the HOMO$-$1, the HOMO and the LUMO+2 can all be observed separately in the spectrum before illumination. At the Fermi edge, the onset of the $n = 1$ IPS can be observed as well. In the spectrum after illumination, none of the three molecular features is present anymore which points toward a drastic change of the electronic system during the photo-induced dimerization.

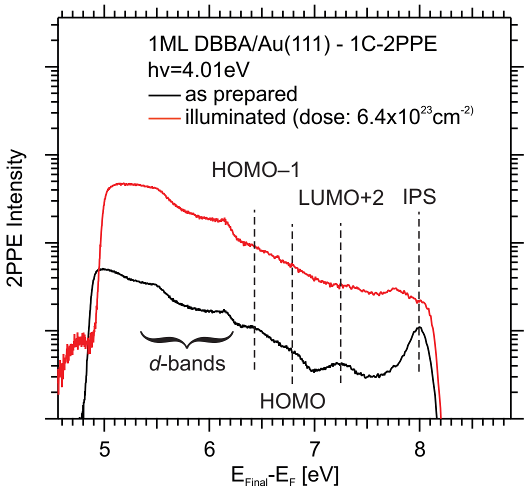

Figure D.1: Effect of the photocoupling reaction on the observed molecular orbitals. 1C-2PPE spectra before and after illumination of 1 ML DBBA/Au(111) with a photon energy of 4.01 eV and a photon dose of 6.4×10^{23} cm^{-2}.

Appendix E

DBBA: Equivalence of Illumination with ArF Excimer Laser and Ti:Sapphire Laser System

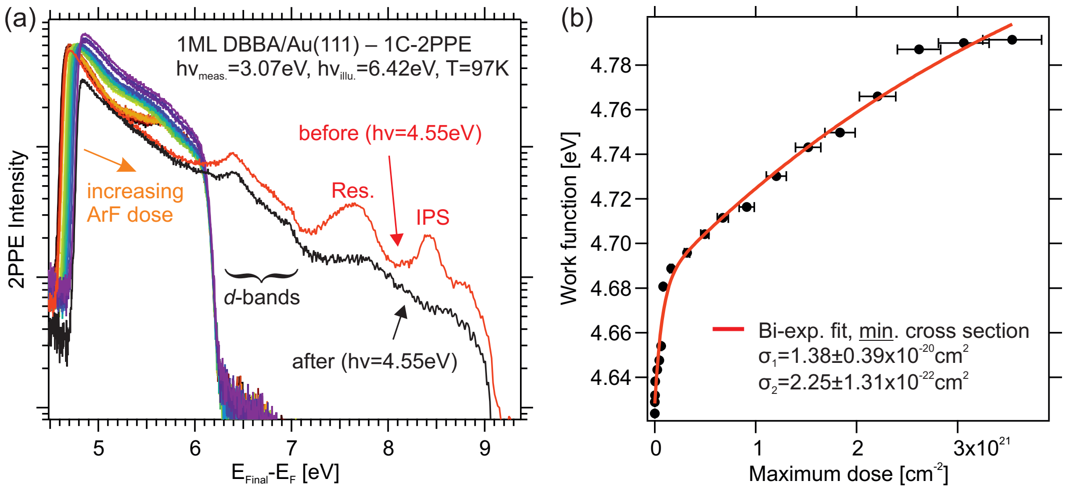

Figure E.1: a) Illumination experiment on 1 ML DBBA/Au(111) in the 2PPE setup. 1C-2PPE spectra were recorded before and after the illumination experiment with a photon energy of 4.55 eV. Between these two measurements, the sample was illuminated with the ArF excimer laser ($h\nu_{\text{illu.}} = 6.42$ eV) while simultaneously 1C-2PPE spectra with a different photon energy, namely 3.07 eV, were recorded. Res.: resonance feature consisting of HOMO−1, HOMO and LUMO+2. (b) Work function shift in the experiment shown in (a) as a function of the maximum photon dose yielding minimum cross sections σ_1 and σ_2.

In sect. 3.2.5 we discussed a photo-induced covalent dimerization of DBBA on the Au(111) surface. This reaction was studied in two different setups with two different methods, namely 2PPE and STM. The illumination experiments in the 2PPE setup were performed using the Ti:Sapphire laser system (which is also used for the spectroscopy itself, see sect. 2.2) as the light source. Since the STM setup was located in a different room (and for other reasons), we used a different light source for illumination experiments, namely an ArF excimer laser with a wavelength of 193 nm ($h\nu_{\text{illu.}} = 6.42$ eV).

In order to verify that illumination with the excimer laser induces the same kind of photo-reaction as the beams of the Ti:Sapphire laser setup, we performed a test experiment in the 2PPE setup, the results of which are shown in Fig. E.1a. First, we recorded a 1C-2PPE spectrum with a photon energy of 4.55 eV which shows the resonant excitation feature comprised of three molecular orbitals and an IPS, as expected (compare to Fig. 3.8). We then illuminated the sample with the excimer laser and monitored the changes of the work function during this illumination. For technical reasons, this could not be done using the beam with a photon energy of 4.55 eV but rather with another beam of the Ti:Sapphire laser setup with a photon energy of 3.07 eV. Fig. E.1b shows the work function as a function of the photon dose of the excimer laser. We observed that the work function increases in a bi-exponential fashion, as represented by two minimum cross sections $\sigma_1 = 1.38 \pm 0.39 \times 10^{-20}$ cm^2 and $\sigma_2 = 2.25 \pm 1.31 \times 10^{-22}$ cm^2. These values are lower limits to the respective cross sections since the excimer laser spot is much larger (diameter: 0.9 mm) than the laser spot used for 2PPE. Therefore, in order to determine the photon dose, we cannot use a value for the power of the excimer laser beam which was averaged over the entire spot. Since, for technical reasons, we cannot determine the exact position of the probing laser spot ($h\nu = 3.07$ eV) within the laser spot of the excimer laser, we used the peak power at the center of the excimer laser spot in order to estimate an upper limit for the photon dose. After illumination with the excimer laser, we again recorded a 1C-2PPE spectrum with the same laser beam as used before the illumination, with a photon energy of 4.55 eV. This posterior spectrum corresponds exactly to the spectra which are obtained after illumination with a laser beam of the Ti:Sapphire laser system, which proves the equivalence of illumination with the excimer laser.

Appendix F

CGNR: Multi-Mass TPD During the Thermal Synthesis of Doped and Pristine CGNR

In order to follow the on-surface reaction toward the undoped and doped CGNR, respectively, HREELS has been employed in our group (S. Stremlau) [209]. Since the photoemission setup is not equipped with a HREELS spectrometer, we used TPD to characterize the adsorbate and the CGNR formation in this setup. This has already been done in case of the AGNR where the different phases of the reaction can be identified by desorption of the molecular backbone as well as other fragments (see sect. 3.2.2).

For the CGNR system, the TPD curves for various masses exhibit a similar behavior, as can be seen in Fig. F.1. The TPD for the undoped CGNR (Fig. F.1a) shows a zero-order peak associated with desorption from the multilayer at around 400 K. The fragment masses 91 amu and 158 amu are representative of the molecular backbone. Note, that the fragment at 158 amu can not be associated with Br_2 since no desorption peak is present in the curve recorded at 160 amu which corresponds to $^{79}Br^{81}Br$. At around 600 K, the traces of Br (79 amu and 81 amu) and HBr (80 amu and 82 amu) all show a desorption feature which is identical for the two respective traces associated with the two different Br isotopes. Note, that the sharp peak in the 79 amu signal at around 400 K is not due to desorption of Br but rather due to the doubly ionized 158 amu fragment of the molecular backbone. In contrast to the AGNR, only one zero-order desorption peak is observed, possibly indicating that the second layer is decoupled from the substrate more strongly than the second layer of DBBA molecules. Similarly to the AGNR, no Br is observed in the multilayer (as demonstrated by the 81 amu trace). The desorption peaks associated with Br and HBr at around 600 K indicate associative desorption of HBr during the

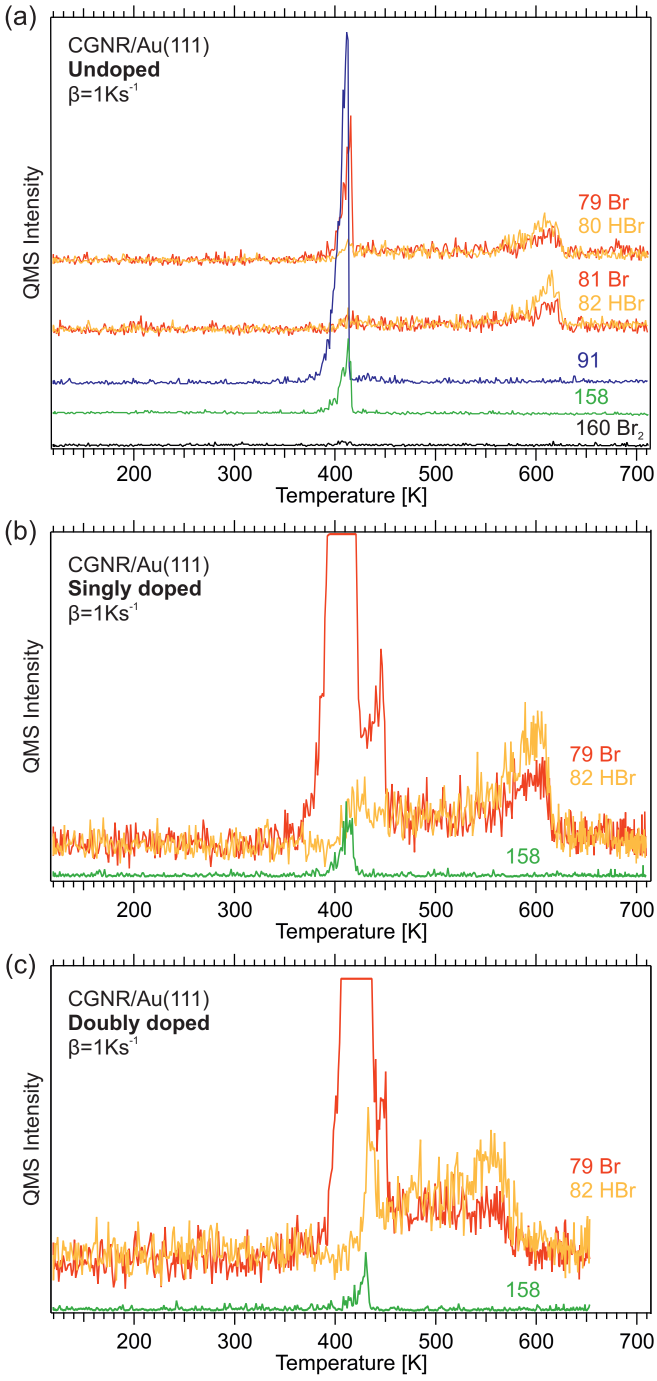

Figure F.1: TPD curves for the (a) undoped as well as (b) singly and (c) doubly doped CGNR on Au(111). The fragment masses (in amu) are given next to the respective curves, along with their assignment. Masses 91 and 158 are characteristic of the molecular backbone. A linear background has been subtracted from the TPD curves and in (b) and (c), the signal at 79 amu was in overrange at around 400 K.

cyclodehydrogenation reaction, in analogy to the AGNR synthesis (see sect. 3.2.2).

The TPD of the doped CGNR (Fig. F.1b,c) show a very similar desorption behavior for both the molecular backbone and the Br and HBr species. However, the TPD of the doped CGNR show a very intense desorption feature at 79 amu which may be due to intact precursor molecules in the multilayer, which is surprising because they were not found for the AGNR and the pristine CGNR. Additionally, a second Br desorption feature can be observed at around 450 K which may be due to desorption of (intact) precursor molecules from the second layer in analogy to the AGNR. The doubly doped CGNR furthermore shows a desorption peak in the HBr trace which is neither coincident with the multilayer desorption nor with the second, less intense desorption feature of the Br trace and might be due to associative desorption of HBr in the multilayer. Note, that despite these unresolved questions concerning the desorption curves of the doped species, the TPDs shown in Fig. F.1 demonstrate successful fabrication of the respective CGNR for which associative desorption of HBr is characteristic.

Appendix G

CGNR: IPS of Singly and Doubly Doped CGNR Investigated with 2PPE

In sect. 3.3.2 we used 2PPE to study the IPS of the pristine CGNR. We found a binding energy of 910 meV with respect to the vacuum level, a dispersion with an effective mass of 0.63 ± 0.04 and a very short lifetime which can not be resolved in our time-resolved 2PPE experiments (TR-2PPE). We have conducted the same 2PPE experiments for the doped CGNR (both with one and two N atoms per precursor), too, and the results are presented here.

In Fig. G.1a, we show a photon energy dependent series of 1C-2PPE spectra for the singly doped CGNR. Similarly to the spectra recorded for the pristine CGNR (see Fig. 3.25) we observe two features near the Fermi edge, one being more intense than the other. We have fitted the spectra with a fit function composed of two Gaussian peak profiles on a linear background which was cut off by a Fermi function. The peak energies shift with the photon energy but the respective slopes are not integer. The behavior of the peaks with increasing photon energy is in complete analogy to that of the pristine CGNR and we therefore assign the intense feature to the IPS lying at 3.68 ± 0.05 eV with respect to the Fermi level and the less intense feature to an unoccupied, high-lying band, CB+n, at 4.04 ± 0.09 eV. The work function amounts to 4.57 ± 0.04 eV. In angle-resolved 2PPE measurements, we find a dispersion of the IPS which can be described by a free-electron like behavior with an effective mass of 0.7 ± 0.1 as shown in Fig. G.1b.

A series of 1C-2PPE spectra recorded for the doubly doped CGNR is shown in Fig. G.1c. Again, we fitted the spectra (in the same way as described above) and two peaks are observed which behave similarly to their counterparts in the pristine and singly doped CGNR. The IPS lies at 3.68 ± 0.05 eV whereas the higher-lying band is found at 3.96 ± 0.17 eV. The work function amounts to 4.55 ± 0.02 eV and the IPS disperses parallel to the surface with an effective mass of 0.8 ± 0.1.

The ultrafast dynamics of the unoccupied electronic states of both the singly and the doubly doped CGNR were studied with TR-2PPE, as shown in Fig. G.2a,b. At the respective photon energies, at which the measurements were conducted, the intensity of the peak associated with the CB+n peak is too low to be detectable. In both CGNR systems we observe an asymmetry of the cross-correlation traces for the IPS and additionally asymmetric intensity distributions near the Fermi edges which points toward unoccupied electronic states probed with the visible pulses. Since the peaks of these states near the Fermi level are partially cut off, we can not determine their energies exactly. However, From the positions relative to the lower lying $n = 1$ IPS and the similar lifetimes, it is reasonable to assume that these higher-lying states originate from the IPS with higher quantum number $n = 2$. The cross-correlation traces of the two IPS yield very similar lifetimes for the two IPS of one system, respectively. For the singly doped CGNR, they amount to 32 fs ($n = 1$) and 36 fs ($n = 2$), respectively, whereas they are an order of magnitude lower in the doubly doped CGNR, namely 5 fs ($n = 1$) and 4 fs ($n = 2$). These values have been determined from fitting a convolution of two pulse shapes and an exponentially decaying population. Since the pulse widths (FWHM of a single pulse) are 71 fs and 61 fs for the two measurements, respectively, the temporal resolution in the regime below these values is limited and the above stated lifetimes have to be considered with care.

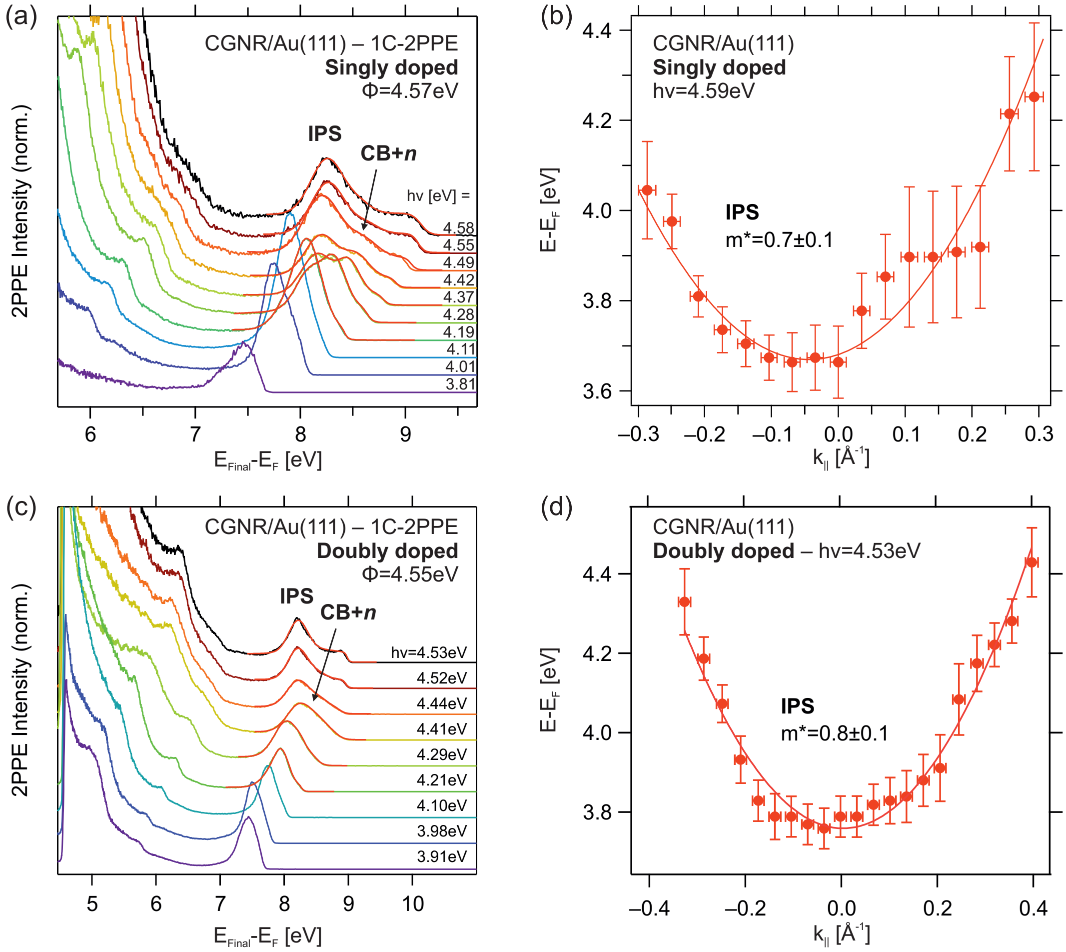

Figure G.1: (a) 1C-2PPE spectra of the singly doped CGNR recorded at various photon energies together with fits (see text). The spectra were normalized to one of the *d*-band features. (b) Dispersion of the IPS of the singly doped CGNR shown on a binding energy scale with respect to the Fermi level. A parabolic fit yields an effective mass of $m^* = 0.7{\pm}0.1$. (c) Photon-energy dependent 1C-2PPE spectra of the doubly doped CGNR. The spectra were normalized to one of the *d*-band features. (d) Shift of the binding energy (with respect to the Fermi level) of the IPS for the doubly doped CGNR. A parabolic fit yields an effective mass of $m^* = 0.8 \pm 0.1$.

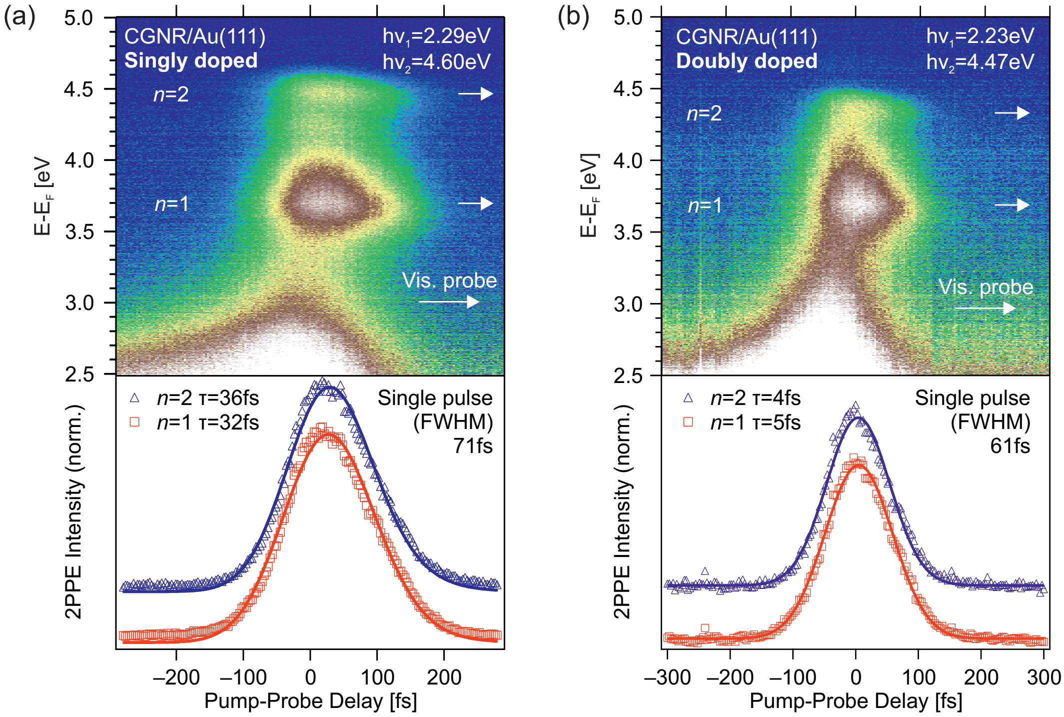

Figure G.2: (a) TR-2PPE experiment of the singly doped CGNR. The false color plot shows the 2PPE intensity (blue: low, white: high) as a function of the time delay and the binding energy of an unoccupied state probed with the visible beam ($h\nu_1$) relative to the Fermi level. Arrows indicate at which orientation of the pump-probe delay an asymmetry is observed. The bottom graph shows the cross-correlation curves of the two unoccupied states which were normalized to their maxima. (b) TR-2PPE experiment of the doubly doped CGNR, analogous to (a).

Appendix H

DMC: LUMO Observed in 1C-2PPE

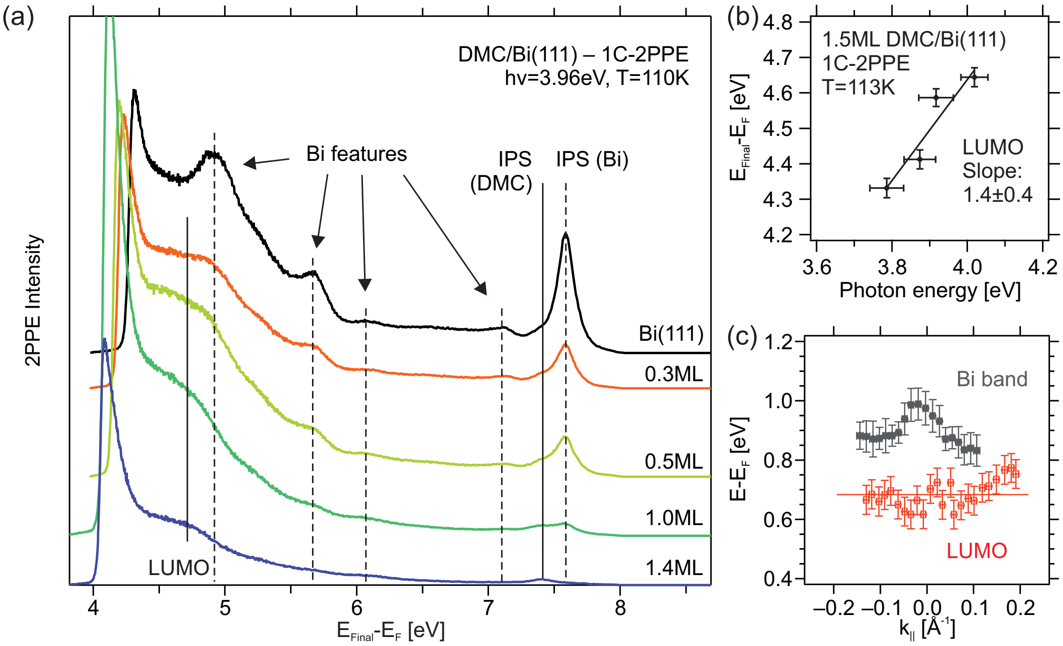

Figure H.1: (a) 1C-2PPE spectra recorded for varying coverages of DMC on the Bi(111) surface. Dashed lines indicate substrate-induced features while the solid lines mark the adsorbate-induced peaks, most notably the LUMO which becomes more pronounced with increasing coverage. (b) Energetic peak shift of the peak associated with the LUMO as a function of photon energy and a linear fit yielding the slope. (c) Dispersion of the LUMO feature measured at a coverage of 1.2 ML and a photon energy of 4.00 eV (red). For comparison, the dispersion of a feature associated with the unoccupied *p*-bands is shown in grey (data of Bi band published in ref. [223]). All graphs adapted from ref. [172].

In sect. 4.2.1, the frontier orbitals of DMC are investigated with UPS and 2C-2PPE. The feature associated with the LUMO is relatively weak in the spectra shown there. Here we present additional 1C-2PPE spectra for different DMC coverages which, too, contain a peak arising from the LUMO of DMC (see Fig. H.1a). In the spectrum of the bare Bi(111) surface, five substrate-related peaks can be observed which are discussed in detail in ref. [223]. One of them, the intense peak at 7.6 eV is due to the IPS of the bare surface. Upon adsorption of DMC, the intensity of these peaks is reduced continuously. Two new peak arise with increasing DMC coverage, one of which is assigned to the IPS of the adsorbate-covered surface at a final state energy of around 7.4 eV. The other DMC-induced peak is broader and has a final state energy of 4.72 eV. The energetic shift of this peak with varying photon energy is shown in Fig. H.1b but the slope of the peak shift is 1.4 ± 0.4 which hardly allows for an unambiguous assignment to an occupied or unoccupied electronic state. However, assuming the peak to correspond to an unoccupied state, the binding energy would amount to 0.76 eV with respect to the Fermi level, in perfect agreement with the value found for the binding energy of the LUMO in 2C-2PPE. We therefore assign this peak to the LUMO as well. Fig. H.1c shows the results of an angle-resolved experiment which demonstrates that the LUMO does not exhibit a dispersion parallel to the surface, as expected. In particular, this behavior is in contrast to the peak arising from the Bi p-bands which lies in the same energetic region, but which does show a dispersion [223].

Appendix I

DMC: Fit of the 2C-2PPE Spectra Yielding the LUMO

The 2C-2PPE spectra recorded of DMC on Bi(111) contain a relatively weak signal from the LUMO of DMC which in addition partially overlaps with the unoccupied *p*-band features of the substrate (see Fig. 4.5b). In order to determine the binding energy of the LUMO, we fitted the spectra for all DMC coverages, as shown in Fig. I.1. The spectra of the bare surface can well be described by three Gaussian fit functions (modeling the density of states of the bands) on a linear background. For the spectra recorded from the adsorbate-covered surface, one additional Gaussian peak profile in the fit was necessary to account for the LUMO. In these fits, the energetic position and width of the Bi features were fixed and their intensity was kept free. In contrast, the energy, width and intensity of the peak associated with the DMC LUMO were all left variable.

Fig. I.2 shows the coverage-dependent behavior of the individual fit components. The energetic position of the LUMO is very stable at a final state energy of (averaged) 4.67 ± 0.03 eV, corresponding to a binding energy of 0.77 ± 0.05 eV with resepect to the Fermi level, and the peak width of the LUMO feature is around 0.2 eV (see Fig. I.2a). With increasing DMC coverage, the intensities of the Bi fit components decrease while the intensity of the LUMO feature first rises and then decreases again (see Fig. I.2b). As evident from Fig. I.2c, the relative intensities of the peaks originating from the Bi substrate change in the same manner which demonstrates that an additional peak contributes to the spectra in this energy region.

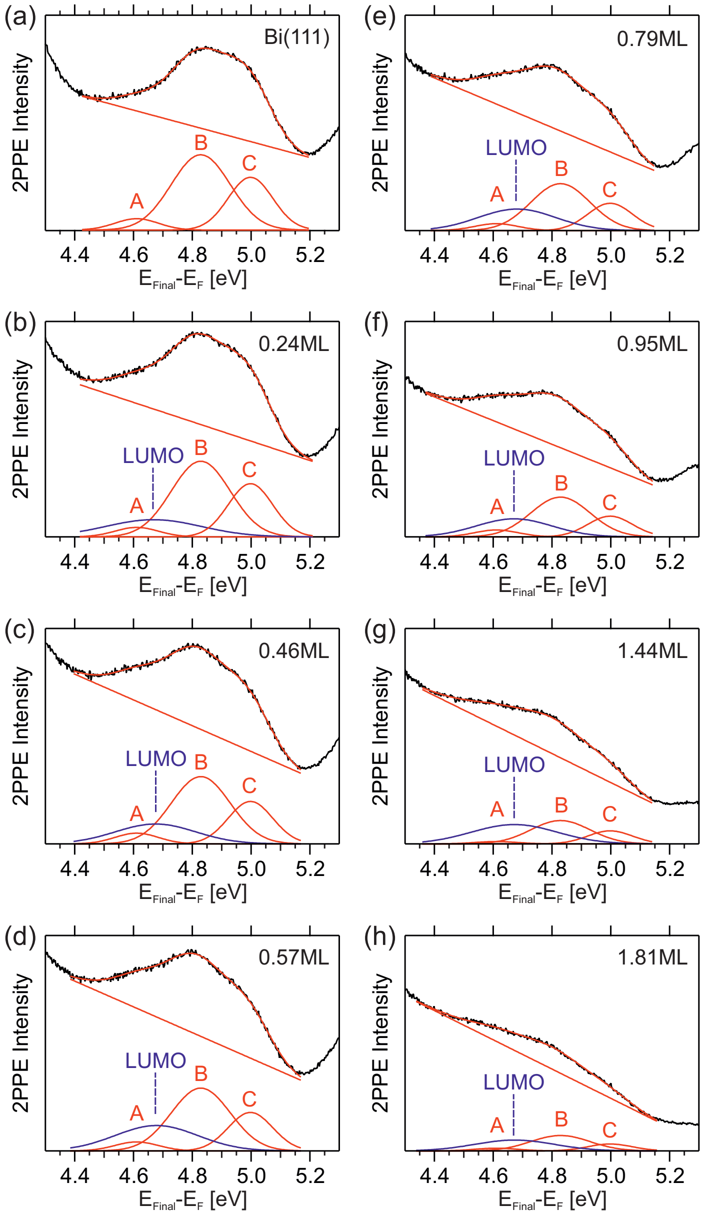

Figure I.1: Fits to the 2C-2PPE spectra of DMC/Bi(111) shown in Fig. 4.5b for different coverages. (a) Fit of the spectrum recorded from the bare Bi(111) surface composed of three Gaussian peak profiles representing the unoccupied *p*-bands on a linear background. (b-h) For the spectra corresponding to the DMC-covered surface, an additional peak was included for the LUMO. In all spectra, the photon energies were $h\nu_1 = 1.95$ eV and $h\nu_2 = 3.90$ eV, respectively. Published in ref. [172].

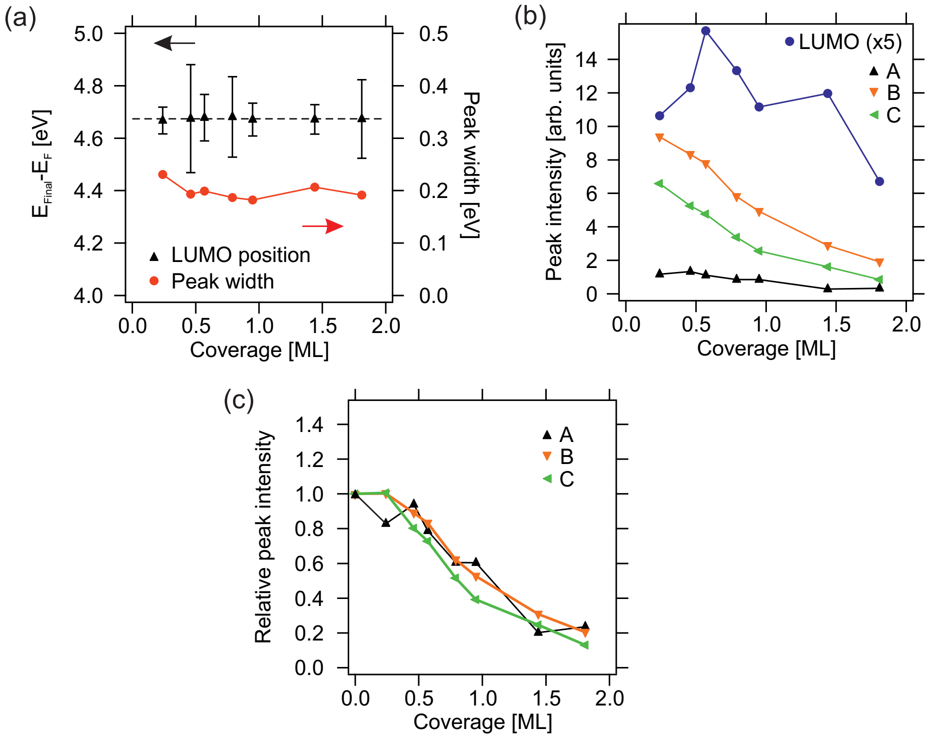

Figure I.2: (a) Coverage-dependence of the energetic position and the peak width of the LUMO feature, as obtained from the fits to the 2C-2PPE spectra. (b) Fitted peak intensity of the three Bi features and the LUMO for varying coverages of DMC. (c) Relative intensity change of the three Bi features with increasing DMC coverage. Published in ref. [172].

Acknowledgments

First of all I would like to thank my advisor Petra Tegeder for supervising my thesis work, for the continuous support and countless helpful discussions over the past five years and particularly for giving me the opportunity to contribute to numerous meetings and conferences as well as to attend beamtimes at BESSY in Berlin and ESRF in Grenoble. I would also like to thank Katharina Franke for agreeing to be the second advisor of my thesis and for the fruitful collaborations over the past years as well as a series of very constructive discussions.

I am especially grateful for having been able to collaborate with several excellent groups in the course of my thesis work. Particularly, I would like to thank Bo Chen, Gelavizh Ahmadi, Benjamin Heinrich and Katharina Franke (Freie Universität Berlin) for our experiments on the structure and photo-induced reactions of DBBA. I am grateful for the productive collaboration concerning the electronic structure of the polyanthrylene and the AGNR with Manuel Utecht, Tillmann Klamroth and Peter Saalfrank (Universität Potsdam). Furthermore, I would like to acknowledge Marie Gille, Felix Braußе and Stefan Hecht (Humboldt-Universität zu Berlin) for synthesis of the CGNR precursors as well as many stimulating discussions. In addition, I would like to thank Beate Priewisch and Karola Rück-Braun (Technische Universität Berlin) for providing the DMC molecules for our experiments.

For the many pleasant hours of working together in the lab I would like to thank my co-workers in Berlin and Heidelberg, Lea Bogner, Alexander Broska, Rocío Cortés, David Gerbert, Marc Hänsel, Felix Leyssner, Friedrich Maaß, Michael Meyer, Laurenz Rettig, Michael Schulze, Stephan Stremlau and Erwan Varene. Particularly, I would like to thank Anton Haase who I enjoyed working with during the time of his diploma thesis. Furthermore I would like to acknowledge Celina Schulze, Judith Specht and Sören Testorp who worked with me during the experiments for their respective bachelor's theses.

For introducing me to the 2PPE setup and his valuable tips and hints concerning the alignment of the laser system I would like to thank my predecessor Sebastian Hagen. I am also grateful for critical review of this thesis'

manuscript by Friederike Ernst, Frank Essenberger and Max Hoffmann.

Working at the ESRF and discussing various aspects of molecular switches at surfaces with our collaborators was highly beneficial for the work presented in this thesis and I would therefore like to thank Giuseppe Mercurio, Martin Willenbockel, Sergey Soubatch and Stefan Tautz (Forschungszentrum Jülich) as well as Reinhard Maurer, Jörg Meyer and Karsten Reuter (Technische Universität München).

The Department of Physics at the Freie Universität Berlin provided an excellent and pleasant environment for me as a PhD student. I am grateful for the opportunity to get valuable feedback during presentations that I could give in the familiar atmosphere of the seminars in the groups of Katharina Franke, Nacho Pascual and Stephanie Reich. Furthermore, the research training group of the collaborative research center SFB 658 offered many opportunities for exchange with other doctoral students from our department and all over Berlin and I especially enjoyed the two meetings of this group which I could attend. Last but not least I would like to acknowledge Dietgard Mallwitz who helped me deal with all kinds of administrative struggles over the past years.

For enabling me to complete my education in public institutions and to conduct the work presented in this thesis, I would like to acknowledge funding by the citizens of Germany and the European Union, through the collaborative research center SFB 658 of the German Research Foundation (DFG), the German Academic Exchange Service (DAAD), the Freie Universität Berlin and the Ruprecht-Karls-Universität Heidelberg.

For their enduring friendship and support well beyond our time in Berlin, I am particularly grateful to my fellow students and friends Frank Essenberger, Max Hoffmann, Andreas Linscheid and Kai Schmitz.

I am also deeply grateful for my parents and grandparents who have supported me all my life and enabled me to pursue my goals.

Finally, I would like to thank Isabelle for accompanying me through all those things that were and those that are yet to come.

Curriculum Vitae

The curriculum vitae is omitted in this version for reasons of data privacy.

List of Publications

Publications Related to this Thesis

Photo-induced and thermal reactions in thin films of an azobenzene derivative on Bi(111)
Christopher Bronner and Petra Tegeder
New J. Phys. **16**, 053004 (2014)

Electronic structure changes during the surface-assisted formation of a graphene nanoribbon
Christopher Bronner, Manuel Utecht, Anton Haase, Peter Saalfrank, Tillmann Klamroth and Petra Tegeder
J. Chem. Phys. **140**, 024701 (2014)

Photoisomerization of an Azobenzene on the Bi(111) Surface
Christopher Bronner, Beate Priewisch, Karola Rück-Braun and Petra Tegeder
J. Phys. Chem. C **117**, 27031 (2013)

Aligning the Band Gap of Graphene Nanoribbons by Monomer Doping
Christopher Bronner, Stephan Stremlau, Marie Gille, Felix Brauße, Anton Haase, Stefan Hecht and Petra Tegeder
Angew. Chem. Int. Ed. **52**, 4422 (2013)

Electronic structure of a sub-nanometer wide bottom-up fabricated graphene nanoribbon: End states, band gap, and dispersion
Christopher Bronner, Felix Leyssner, Stephan Stremlau, Manuel Utecht, Peter Saalfrank, Tillmann Klamroth and Petra Tegeder
Phys. Rev. B **86**, 085444 (2012)

Publications Not Related to this Thesis

Adsorption energetics of azobenzenes on noble metal surfaces
Michael Schulze, Christopher Bronner and Petra Tegeder
J. Phys.: Condens. Matter, in press (2014)

Relaxation Dynamics of Photoexcited Charge Carriers at the Bi(111) Surface
Christopher Bronner and Petra Tegeder
Phys. Rev. B **89**, 115105 (2014)

Unoccupied electronic band structure of the semi-metallic Bi(111) surface probed with two-photon photoemission
Christopher Bronner and Petra Tegeder
Phys. Rev. B **87**, 035123 (2013)

Ultrafast Exciton Population, Relaxation, and Decay Dynamics in Thin Oligothiophene Films
Erwan Varene, Lea Bogner, Christopher Bronner and Petra Tegeder
Phys. Rev. Lett. **109**, 207601 (2012)

The influence of the electronic structure of adsorbate–substrate complexes on photoisomerization ability
Christopher Bronner, Michael Schulze, Sebastian Hagen and Petra Tegeder
New J. Phys. **14**, 043023 (2012)

Switching ability of nitro-spiropyran on Au(111): electronic structure changes as a sensitive probe during a ring-opening reaction
Christopher Bronner, Gunnar Schulze, Katharina J. Franke, José Ignacio Pascual and Petra Tegeder
J. Phys.: Condens. Matter **23**, 484005 (2011)

Azobenzene versus 3,3',5,5'-tetra-tert-butyl-azobenzene (TBA) at Au(111): characterizing the role of spacer groups
Erik R. McNellis, Christopher Bronner, Jörg Meyer, Martin Weinelt, Petra Tegeder and Karsten Reuter
Phys. Chem. Chem. Phys. **12**, 6404-6412 (2010)

Publications In Preparation or Under Review

Photoinduced Topochemistry on a Metal Surface
Christopher Bronner, Bo Chen, Benjamin W. Heinrich, Gelavizh Ahmadi, Katharina J. Franke and Petra Tegeder
submitted

Role of Br Atoms in the Bottom-Up Synthesis of a Graphene Nanoribbon on Au(111)
Christopher Bronner and Petra Tegeder
in preparation

List of Conference Contributions

All contributions listed here were as presenting author.

Photoisomerization of an azobenzene derivative on Bi(111)
Christopher Bronner and Petra Tegeder
Poster
563. Wilhelm and Else Heraeus Seminar on 'Functional Molecules at Surfaces', Bad Honnef, Germany, 2014

Monomer Doping of Self-Assembled Graphene Nanoribbons for Band Gap Alignment
Christopher Bronner, Stephan Stremlau, Marie Gille, Felix Brauße, Anton Haase, Stefan Hecht and Petra Tegeder
Presentation
DPG Spring Meeting, Dresden, Germany, 2014

Monomer Doping of Self-Assembled Graphene Nanoribbons for Band Gap Alignment
Christopher Bronner, Stephan Stremlau, Marie Gille, Felix Brauße, Anton Haase, Stefan Hecht and Petra Tegeder
Presentation
APS March Meeting, Denver, CO, USA, 2014

Aligning the Band Gap of Graphene Nanoribbons by Monomer Doping
Christopher Bronner, Stephan Stremlau, Marie Gille, Felix Brauße, Anton Haase, Stefan Hecht and Petra Tegeder
Poster
Dresden School on Functional Nanomaterials, Dresden, Germany, 2013

Optically and thermally induced reactions of an azobenzene derivative on Bi(111)
Christopher Bronner, Beate Priewisch, Karola Rück-Braun and Petra Tegeder
Presentation
Workshop of the Research Training Group of the SFB658, Zeuthen, Germany, 2013

Optically and thermally induced reactions of an azobenzene derivative on Bi(111)
Christopher Bronner, Beate Priewisch, Karola Rück-Braun and Petra Tegeder
Presentation
DPG Spring Meeting, Regensburg, Germany, 2013

Evolution of the electronic structure during formation of a graphene nanoribbon in an on-surface synthesis
Christopher Bronner, Felix Leyssner, Stephan Stremlau, Manuel Utecht, Anton Haase, Peter Saalfrank, Tillmann Klamroth and Petra Tegeder
Presentation
European Conference on Surface Science (ECOSS 29), Edinburgh, UK, 2012

Measuring the one-dimensional band structure of an armchair graphene nanoribbon
Christopher Bronner, Felix Leyssner, Stephan Meyer, Manuel Utecht, Peter Saalfrank, Tillmann Klamroth and Petra Tegeder
Presentation
DPG Spring Meeting, Berlin, Germany, 2012

Band Structure Measurements of Bottom-up Fabricated Graphene Nanoribbons
Christopher Bronner, Felix Leyssner, Stephan Meyer, Manuel Utecht, Tillmann Klamroth, Peter Saalfrank and Petra Tegeder
Presentation
APS March Meeting, Boston, MA, USA, 2012

Role of the electronic structure on the isomerization ability of adsorbed photoswitches
Christopher Bronner, Michael Schulze, Sebastian Hagen and Petra Tegeder
Poster
International Sfb658 Symposium on Molecular Switches, Potsdam, Germany, 2012

The electronic structure of a bottom-up fabricated graphene nanoribbon on Au(111)
Christopher Bronner, Felix Leyssner, Stephan Meyer and Petra Tegeder
Presentation
European Conference on Surface Science (ECOSS 28), Wroclaw, Poland, 2011

Electronic Structure of a Spiropyran Derived Molecular Switch in Direct Contact with the Au(111) Surface
Christopher Bronner, Gunnar Schulze, Katharina J. Franke, José Ignacio Pascual and Petra Tegeder
Presentation
Workshop of the Research Training Group of the SFB658, Lübbenau, Germany, 2011
Part of the organizing committee

Electronic structure of bottom-up fabricated graphene nanoribbons at the gold surface
Christopher Bronner, Felix Leyssner, Stephan Meyer and Petra Tegeder
Poster
International workshop on Elementary Processes in Solids and at Interfaces (ElePSI), Kloster Banz, Germany, 2011

Electronic Structure of a Spiropyran Derived Molecular Switch in Direct Contact with the Au(111) Surface
Christopher Bronner, Gunnar Schulze, Katharina J. Franke, José Ignacio Pascual and Petra Tegeder
Presentation
DPG Spring Meeting, Dresden, Germany, 2011

List of Acronyms

1C-2PPE	One-color two-photon photoemission
2C-2PPE	Two-color two-photon photoemission
2PPE	Two-photon photoemission
3PPE	Three-photon photoemission
AC	Auto-correlation
AES	Auger electron spectroscopy
AGNR	Armchair graphene nanoribbon
AR-2PPE	Angle-resolved two-photon photoemission
ARUPS	Angle-resolved ultraviolet photoelectron spectroscopy
BBO	β-barium-borate
CB	Conduction band
CCD	Charge-coupled device
CGNR	Chevron graphene nanoribbon
CNT	Carbon nanotube
DBBA	10,10'-dibromo-9,9'-bianthryl
DEA	Dissociative electron attachment
DFT	Density functional theory
DMC	Di-meta-cyano azobenzene
DOS	Density of states
FET	Field-effect transistor
FWHM	Full width at half maximum
GGA	General gradient approximation
GNR	Graphene nanoribbon
HOMO	Highest occupied molecular orbital
HREELS	High-resolution electron energy loss spectroscopy
IPES	Inverse photoelectron spectroscopy
IPS	Image-potential state
LDA	Local density approximation
LEED	Low energy electron diffraction
LSDA	Local spin density approximation
LUMO	Lowest unoccupied molecular orbital

ML	Monolayer
OES	Occupied edge state
OPA	Optical parametric amplifier
PBE	Perdew-Burke-Enzerhof
PES	Potential energy surface
PSS	Photostationary state
QMS	Quadrupole mass spectrometer
SAM	Self-assembled monolayer
SS	Surface state
STM	Scanning tunneling microscope
STS	Scanning tunneling spectroscopy
TBA	tetra-*tert*-butyl azobenzene
TBU	Tight binding $+U$ approach
TOF	Time-of-flight spectrometer
TPD	Temperature-programmed desorption
TR-2PPE	Time-resolved two-photon photoemission
UES	Unoccupied edge state
UHV	Ultra-high vacuum
UPS	Ultraviolet photoelectron spectroscopy
VB	Valence band
XC	Cross-correlation

Bibliography

[1] Packan, P. A.: Pushing the Limits. *Science* 285, 2079–2081 (1999)

[2] Schulz, M.: The end of the road for silicon? *Nature* 399, 729–730 (1999)

[3] Chau, R., Doyle, B., Datta, S., Kavalieros, J., and Zhang, K.: Integrated nanoelectronics for the future. *Nat Mater* 6, 810–812 (2007)

[4] Meric, I., Han, M. Y., Young, A. F., Ozyilmaz, B., Kim, P., and Shepard, K. L.: Current saturation in zero-bandgap, top-gated graphene field-effect transistors. *Nat Nanotechnol* 3, 654–659 (2008)

[5] Lin, Y.-M., Jenkins, K. A., Valdes-Garcia, A., Small, J. P., Farmer, D. B., and Avouris, P.: Operation of Graphene Transistors at Gigahertz Frequencies. *Nano Lett* 9, 422–426 (2009)

[6] Xia, F., Farmer, D. B., Lin, Y.-m., and Avouris, P.: Graphene Field-Effect Transistors with High On/Off Current Ratio and Large Transport Band Gap at Room Temperature. *Nano Lett* 10, 715–718 (2010)

[7] Schwierz, F.: Graphene transistors. *Nat Nanotechnol* 5, 487–496 (2010)

[8] Lin, Y.-M., Dimitrakopoulos, C., Jenkins, K. A., Farmer, D. B., Chiu, H.-Y., Grill, A., and Avouris, P.: 100-GHz Transistors from Wafer-Scale Epitaxial Graphene. *Science* 327, 662 (2010)

[9] Wu, Y., Lin, Y.-m., Bol, A. A., Jenkins, K. A., Xia, F., Farmer, D. B., Zhu, Y., and Avouris, P.: High-frequency, scaled graphene transistors on diamond-like carbon. *Nature* 472, 74–78 (2011)

[10] Reed, M. A., Zhou, C., Muller, C. J., Burgin, T. P., and Tour, J. M.: Conductance of a Molecular Junction. *Science* 278, 252–254 (1997)

[11] Cui, X. D., Primak, A., Zarate, X., Tomfohr, J., Sankey, O. F., Moore, A. L., Moore, T. A., Gust, D., Harris, G., and Lindsay, S. M.: Reproducible Measurement of Single-Molecule Conductivity. *Science* 294, 571–574 (2001)

[12] Lafferentz, L., Ample, F., Yu, H., Hecht, S., Joachim, C., and Grill, L.: Conductance of a Single Conjugated Polymer as a Continuous Function of Its Length. *Science* 323, 1193–1197 (2009)

[13] Koch, M., Ample, F., Joachim, C., and Grill, L.: Voltage-dependent conductance of a single graphene nanoribbon. *Nat Nanotechnol* 7, 713–717 (2012)

[14] Parthenopoulos, D. A. and Rentzepis, P. M.: Three-Dimensional Optical Storage Memory. *Science* 245, 843–845 (1989)

[15] Liu, Z. F., Hashimoto, K., and Fujishima, A.: Photoelectrochemical information storage using an azobenzene derivative. *Nature* 347, 658–660 (1990)

[16] Ikeda, T. and Tsutsumi, O.: Optical Switching and Image Storage by Means of Azobenzene Liquid-Crystal Films. *Science* 268, 1873–1875 (1995)

[17] Kawata, S. and Kawata, Y.: Three-Dimensional Optical Data Storage Using Photochromic Materials. *Chem Rev* 100, 1777–1788 (2000)

[18] Berkovic, G., Krongauz, V., and Weiss, V.: Spiropyrans and Spirooxazines for Memories and Switches. *Chem Rev* 100, 1741–1753 (2000)

[19] Kim, K. S., Zhao, Y., Jang, H., Lee, S. Y., Kim, J. M., Kim, K. S., Ahn, J.-H., Kim, P., Choi, J.-Y., and Hong, B. H.: Large-scale pattern growth of graphene films for stretchable transparent electrodes. *Nature* 457, 706–710 (2009)

[20] Smith, M. B. and Michl, J.: Singlet Fission. *Chem Rev* 110, 6891–6936 (2010)

[21] Chan, W.-L., Ligges, M., Jailaubekov, A., Kaake, L., Miaja-Avila, L., and Zhu, X.-Y.: Observing the Multiexciton State in Singlet Fission and Ensuing Ultrafast Multielectron Transfer. *Science* 334, 1541–1545 (2011)

[22] Gabor, N. M., Zhong, Z., Bosnick, K., Park, J., and McEuen, P. L.: Extremely Efficient Multiple Electron-Hole Pair Generation in Carbon Nanotube Photodiodes. *Science* 325, 1367–1371 (2009)

[23] Balzani, V., Credi, A., and Venturi, M.: Molecular Machines Working on Surfaces and at Interfaces. *ChemPhysChem* 9, 202–220 (2008)

[24] Feringa, B. L., ed.: *Molecular Switches.* Wiley-VCH, Weinheim (2001)

[25] Browne, W. R. and Feringa, B. L.: Making molecular machines work. *Nat Nanotechnol* 1, 25–35 (2006)

[26] Aviram, A. and Ratner, M. A.: Molecular Rectifiers. *Chem Phys Lett* 29, 277–283 (1974)

[27] Kudernac, T., Ruangsupapichat, N., Parschau, M., Maciá, B., Katsonis, N., Harutyunyan, S. R., Ernst, K.-H., and Feringa, B. L.: Electrically driven directional motion of a four-wheeled molecule on a metal surface. *Nature* 479, 208–211 (2011)

[28] Tierney, H. L., Murphy, C. J., Jewell, A. D., Baber, A. E., Iski, E. V., Khodaverdian, H. Y., McGuire, A. F., Klebanov, N., and Sykes, E. C. H.: Experimental demonstration of a single-molecule electric motor. *Nat Nanotechnol* 6, 625–629 (2011)

[29] Ichimura, K., Oh, S.-K., and Nakagawa, M.: Light-Driven Motion of Liquids on a Photoresponsive Surface. *Science* 288, 1624–1626 (2000)

[30] Niazov, T., Shlyahovsky, B., and Willner, I.: Photoswitchable Electrocatalysis and Catalyzed Chemiluminescence Using Photoisomerizable Monolayer-Functionalized Surfaces and Pt Nanoparticles. *J Am Chem Soc* 129, 6374–6375 (2007)

[31] Liu, D., Xie, Y., Shao, H., and Jiang, X.: Using Azobenzene-Embedded Self-Assembled Monolayers To Photochemically Control Cell Adhesion Reversibly. *Angew Chem Int Ed* 48, 4406–4408 (2009)

[32] Klajn, R.: Immobilized azobenzenes for the construction of photoresponsive materials. *Pure Appl Chem* 82, 2247–2279 (2010)

[33] Whitesides, G. M., Mathias, J. P., and Seto, C. T.: Molecular self-assembly and nanochemistry: a chemical strategy for the synthesis of nanostructures. *Science* 254, 1312–1319 (1991)

[34] Barth, J. V., Costantini, G., and Kern, K.: Engineering atomic and molecular nanostructures at surfaces. *Nature* 437, 671–679 (2005)

[35] Grill, L., Dyer, M., Lafferentz, L., Persson, M., Peters, M. V., and Hecht, S.: Nano-architectures by covalent assembly of molecular building blocks. *Nat Nanotechnol* 2, 687–691 (2007)

[36] Hsieh, D., Qian, D., Wray, L., Xia, Y., Hor, Y. S., Cava, R. J., and Hasan, M. Z.: A topological Dirac insulator in a quantum spin Hall phase. *Nature* 452, 970–974 (2008)

[37] Zhang, H., Liu, C.-X., Qi, X.-L., Dai, X., Fang, Z., and Zhang, S.-C.: Topological insulators in Bi2Se3, Bi2Te3 and Sb2Te3 with a single Dirac cone on the surface. *Nat Phys* 5, 438–442 (2009)

[38] Datta, S. and Das, B.: Electronic analog of the electro-optic modulator. *Appl Phys Lett* 56, 665 (1990)

[39] Koga, T., Nitta, J., Takayanagi, H., and Datta, S.: Spin-Filter Device Based on the Rashba Effect Using a Nonmagnetic Resonant Tunneling Diode. *Phys Rev Lett* 88, 126601 (2002)

[40] Novoselov, K. S., Geim, A. K., Morozov, S. V., Jiang, D., Zhang, Y., Dubonos, S. V., Grigorieva, I. V., and Firsov, A. A.: Electric Field Effect in Atomically Thin Carbon Films. *Science* 306, 666–669 (2004)

[41] Novoselov, K. S., Geim, A. K., Morozov, S. V., Jiang, D., Katsnelson, M. I., Grigorieva, I. V., Dubonos, S. V., and Firsov, A. A.: Two-dimensional gas of massless Dirac fermions in graphene. *Nature* 438, 197–200 (2005)

[42] Geim, A. K. and Novoselov, K. S.: The rise of graphene. *Nat Mater* 6, 183–191 (2007)

[43] Castro Neto, A. H., Guinea, F., Peres, N. M. R., Novoselov, K. S., and Geim, A. K.: The electronic properties of graphene. *Rev Mod Phys* 81, 109 (2009)

[44] Ni, Z. H., Yu, T., Lu, Y. H., Wang, Y. Y., Feng, Y. P., and Shen, Z. X.: Uniaxial Strain on Graphene: Raman Spectroscopy Study and Band-Gap Opening. *ACS Nano* 2, 2301–2305 (2008)

[45] Mohiuddin, T. M. G., Lombardo, A., Nair, R. R., Bonetti, A., Savini, G., Jalil, R., Bonini, N., Basko, D. M., Galiotis, C., Marzari, N., Novoselov, K. S., Geim, A. K., and Ferrari, A. C.: Uniaxial strain in graphene by Raman spectroscopy: G peak splitting, Grüneisen parameters, and sample orientation. *Phys Rev B* 79, 205433 (2009)

[46] Guinea, F., Katsnelson, M. I., and Geim, A. K.: Energy gaps and a zero-field quantum Hall effect in graphene by strain engineering. *Nat Phys* 6, 30–33 (2010)

[47] Ohta, T., Bostwick, A., Seyller, T., Horn, K., and Rotenberg, E.: Controlling the Electronic Structure of Bilayer Graphene. *Science* 313, 951–954 (2006)

[48] Zhang, Y., Tang, T.-T., Girit, C., Hao, Z., Martin, M. C., Zettl, A., Crommie, M. F., Shen, Y. R., and Wang, F.: Direct observation of a widely tunable bandgap in bilayer graphene. *Nature* 459, 820–823 (2009)

[49] Nakada, K., Fujita, M., Dresselhaus, G., and Dresselhaus, M. S.: Edge state in graphene ribbons: Nanometer size effect and edge shape dependence. *Phys Rev B* 54, 17954 (1996)

[50] Ezawa, M.: Peculiar width dependence of the electronic properties of carbon nanoribbons. *Phys Rev B* 73, 045432 (2006)

[51] Barone, V., Hod, O., and Scuseria, G. E.: Electronic Structure and Stability of Semiconducting Graphene Nanoribbons. *Nano Lett* 6, 2748–2754 (2006)

[52] Son, Y.-W., Cohen, M. L., and Louie, S. G.: Energy Gaps in Graphene Nanoribbons. *Phys Rev Lett* 97, 216803 (2006)

[53] Han, M. Y., Özyilmaz, B., Zhang, Y., and Kim, P.: Energy Band-Gap Engineering of Graphene Nanoribbons. *Phys Rev Lett* 98, 206805 (2007)

[54] Zheng, H., Wang, Z. F., Luo, T., Shi, Q. W., and Chen, J.: Analytical study of electronic structure in armchair graphene nanoribbons. *Phys Rev B* 75, 165414 (2007)

[55] Yang, L., Park, C.-H., Son, Y.-W., Cohen, M. L., and Louie, S. G.: Quasiparticle Energies and Band Gaps in Graphene Nanoribbons. *Phys Rev Lett* 99, 186801 (2007)

[56] Li, X., Wang, X., Zhang, L., Lee, S., and Dai, H.: Chemically Derived, Ultrasmooth Graphene Nanoribbon Semiconductors. *Science* 319, 1229–1232 (2008)

[57] Chaves, A. J., Lima, G. D., de Paula, W., Cordeiro, C. E., Delfino, A., Frederico, T., and Oliveira, O.: Dynamical gap generation in graphene nanoribbons: An effective relativistic field theoretical model. *Phys Rev B* 83, 153405 (2011)

[58] Fujita, M., Wakabayashi, K., Nakada, K., and Kusakabe, K.: Peculiar Localized State at Zigzag Graphite Edge. *J Phys Soc Jpn* 65, 1920–1923 (1996)

[59] Son, Y.-W., Cohen, M. L., and Louie, S. G.: Half-metallic graphene nanoribbons. *Nature* 444, 347–349 (2006)

[60] Hod, O., Peralta, J. E., and Scuseria, G. E.: Edge effects in finite elongated graphene nanoribbons. *Phys Rev B* 76, 233401 (2007)

[61] Lee, Y.-L., Kim, S., Park, C., Ihm, J., and Son, Y.-W.: Controlling Half-Metallicity of Graphene Nanoribbons by Using a Ferroelectric Polymer. *ACS Nano* 4, 1345–1350 (2010)

[62] Tao, C., Jiao, L., Yazyev, O. V., Chen, Y.-C., Feng, J., Zhang, X., Capaz, R. B., Tour, J. M., Zettl, A., Louie, S. G., Dai, H., and Crommie, M. F.: Spatially resolving edge states of chiral graphene nanoribbons. *Nat Phys* 7, 616–620 (2011)

[63] Zhang, X., Yazyev, O. V., Feng, J., Xie, L., Tao, C., Chen, Y.-C., Jiao, L., Pedramrazi, Z., Zettl, A., Louie, S. G., Dai, H., and Crommie, M. F.: Experimentally Engineering the Edge Termination of Graphene Nanoribbons. *ACS Nano* 7, 198–202 (2013)

[64] Cervantes-Sodi, F., Csányi, G., Piscanec, S., and Ferrari, A. C.: Edge-functionalized and substitutionally doped graphene nanoribbons: Electronic and spin properties. *Phys Rev B* 77, 165427 (2008)

[65] Wang, X., Li, X., Zhang, L., Yoon, Y., Weber, P. K., Wang, H., Guo, J., and Dai, H.: N-Doping of Graphene Through Electrothermal Reactions with Ammonia. *Science* 324, 768–771 (2009)

[66] Terrones, H., Lv, R., Terrones, M., and Dresselhaus, M. S.: The role of defects and doping in 2D graphene sheets and 1D nanoribbons. *Rep Prog Phys* 75, 062501 (2012)

[67] Wei, D., Liu, Y., Wang, Y., Zhang, H., Huang, L., and Yu, G.: Synthesis of N-Doped Graphene by Chemical Vapor Deposition and Its Electrical Properties. *Nano Lett* 9, 1752–1758 (2009)

[68] Wang, H., Maiyalagan, T., and Wang, X.: Review on Recent Progress in Nitrogen-Doped Graphene: Synthesis, Characterization, and Its Potential Applications. *ACS Catal* 2, 781–794 (2012)

[69] Wang, X., Ouyang, Y., Li, X., Wang, H., Guo, J., and Dai, H.: Room-Temperature All-Semiconducting Sub-10-nm Graphene Nanoribbon Field-Effect Transistors. *Phys Rev Lett* 100, 206803 (2008)

[70] Zhang, Y., Tan, Y.-W., Stormer, H. L., and Kim, P.: Experimental observation of the quantum Hall effect and Berry's phase in graphene. *Nature* 438, 201–204 (2005)

[71] Kosynkin, D. V., Higginbotham, A. L., Sinitskii, A., Lomeda, J. R., Dimiev, A., Price, B. K., and Tour, J. M.: Longitudinal unzipping of carbon nanotubes to form graphene nanoribbons. *Nature* 458, 872–876 (2009)

[72] Jiao, L., Zhang, L., Wang, X., Diankov, G., and Dai, H.: Narrow graphene nanoribbons from carbon nanotubes. *Nature* 458, 877–880 (2009)

[73] Shimizu, T., Haruyama, J., Marcano, D. C., Kosinkin, D. V., Tour, J. M., Hirose, K., and Suenaga, K.: Large intrinsic energy bandgaps in annealed nanotube-derived graphene nanoribbons. *Nat Nanotechnol* 6, 45–50 (2011)

[74] Theobald, J. A., Oxtoby, N. S., Phillips, M. A., Champness, N. R., and Beton, P. H.: Controlling molecular deposition and layer structure with supramolecular surface assemblies. *Nature* 424, 1029–1031 (2003)

[75] Bieri, M., Treier, M., Cai, J., Aït-Mansour, K., Ruffieux, P., Gröning, O., Gröning, P., Kastler, M., Rieger, R., Feng, X., Müllen, K., and Fasel, R.: Porous graphenes: two-dimensional polymer synthesis with atomic precision. *Chem Commun* 6919–6921 (2009)

[76] Lafferentz, L., Eberhardt, V., Dri, C., Africh, C., Comelli, G., Esch, F., Hecht, S., and Grill, L.: Controlling on-surface polymerization by hierarchical and substrate-directed growth. *Nat Chem* 4, 215–220 (2012)

[77] Cai, J., Ruffieux, P., Jaafar, R., Bieri, M., Braun, T., Blankenburg, S., Muoth, M., Seitsonen, A. P., Saleh, M., Feng, X., Müllen, K., and Fasel, R.: Atomically precise bottom-up fabrication of graphene nanoribbons. *Nature* 466, 470–473 (2010)

[78] Chen, Y.-C., de Oteyza, D. G., Pedramrazi, Z., Chen, C., Fischer, F. R., and Crommie, M. F.: Tuning the Band Gap of Graphene Nanoribbons Synthesized from Molecular Precursors. *ACS Nano* 7, 6123–6128 (2013)

[79] Irie, M.: Photochromism: Memories and Switches–Introduction. *Chem Rev* 100, 1683–1684 (2000)

[80] Nägele, T., Hoche, R., Zinth, W., and Wachtveitl, J.: Femtosecond photoisomerization of *cis*-azobenzene. *Chem Phys Lett* 272, 489–495 (1997)

[81] Satzger, H., Root, C., and Braun, M.: Excited-State Dynamics of *trans*- and *cis*-Azobenzene after UV Excitation in the $\pi\pi^*$ Band. *J Phys Chem A* 108, 6265–6271 (2004)

[82] Görner, H.: Photochromism of nitrospiropyrans: effects of structure, solvent and temperature. *Phys Chem Chem Phys* 3, 416–423 (2001)

[83] Futami, Y., Chin, M. L. S., Kudoh, S., Takayanagi, M., and Nakata, M.: Conformations of nitro-substituted spiropyran and merocyanine studied by low-temperature matrix-isolation infrared spectroscopy and density-functional-theory calculation. *Chem Phys Lett* 370, 460–468 (2003)

[84] Cottone, G., Noto, R., and La Manna, G.: Theoretical study of spiropyran-merocyanine thermal isomerization. *Chem Phys Lett* 388, 218–222 (2004)

[85] Matsuda, K. and Irie, M.: Diarylethene as a photoswitching unit. *J Photoch Photobio C* 5, 169–182 (2004)

[86] Kim, Y., Hellmuth, T. J., Sysoiev, D., Pauly, F., Pietsch, T., Wolf, J., Erbe, A., Huhn, T., Groth, U., Steiner, U. E., and Scheer, E.: Charge Transport Characteristics of Diarylethene Photoswitching Single-Molecule Junctions. *Nano Lett* 12, 3736–3742 (2012)

[87] Tsukahara, N., Noto, K.-i., Ohara, M., Shiraki, S., Takagi, N., Takata, Y., Miyawaki, J., Taguchi, M., Chainani, A., Shin, S., and Kawai, M.: Adsorption-Induced Switching of Magnetic Anisotropy in a Single Iron(II) Phthalocyanine Molecule on an Oxidized Cu(110) Surface. *Phys Rev Lett* 102, 167203 (2009)

[88] Komeda, T., Isshiki, H., Liu, J., Zhang, Y.-F., Lorente, N., Katoh, K., Breedlove, B. K., and Yamashita, M.: Observation and electric current control of a local spin in a single-molecule magnet. *Nat Commun* 2, 217 (2011)

[89] Wende, H., Bernien, M., Luo, J., Sorg, C., Ponpandian, N., Kurde, J., Miguel, J., Piantek, M., Xu, X., Eckhold, P., Kuch, W., Baberschke, K., Panchmatia, P. M., Sanyal, B., Oppeneer, P. M., and Eriksson, O.: Substrate-induced magnetic ordering and switching of iron porphyrin molecules. *Nat Mater* 6, 516–520 (2007)

[90] Wäckerlin, C., Chylarecka, D., Kleibert, A., Müller, K., Iacovita, C., Nolting, F., Jung, T. A., and Ballav, N.: Controlling spins in adsorbed molecules by a chemical switch. *Nat Commun* 1, 61 (2010)

[91] Whitten, D. G., Wildes, P. D., Pacifici, J. G., and Irick, G., Jr.: Solvent and substituent on the thermal isomerization of substituted azobenzenes. Flash spectroscopic study. *J Am Chem Soc* 93, 2004–2008 (1971)

[92] Piantek, M., Schulze, G., Koch, M., Franke, K. J., Leyssner, F., Krüger, A., Navío, C., Miguel, J., Bernien, M., Wolf, M., Kuch, W., Tegeder, P., and Pascual, J. I.: Reversing the Thermal Stability of a Molecular Switch on a Gold Surface: Ring-Opening Reaction of Nitrospiropyran. *J Am Chem Soc* 131, 12729–12735 (2009)

[93] Alemani, M., Peters, M. V., Hecht, S., Rieder, K.-H., Moresco, F., and Grill, L.: Electric Field-Induced Isomerization of Azobenzene by STM. *J Am Chem Soc* 128, 14446–14447 (2006)

[94] Choi, B.-Y., Kahng, S.-J., Kim, S., Kim, H., Kim, H. W., Song, Y. J., Ihm, J., and Kuk, Y.: Conformational Molecular Switch of the Azobenzene Molecule: A Scanning Tunneling Microscopy Study. *Phys Rev Lett* 96, 156106 (2006)

[95] Henzl, J., Mehlhorn, M., Gawronski, H., Rieder, K.-H., and Morgenstern, K.: Reversible *cis–trans* Isomerization of a Single Azobenzene Molecule. *Angew Chem Int Ed* 45, 603–606 (2006)

[96] Venkataramani, S., Jana, U., Dommaschk, M., Sönnichsen, F. D., Tuczek, F., and Herges, R.: Magnetic Bistability of Molecules in Homogeneous Solution at Room Temperature. *Science* 331, 445–448 (2011)

[97] Whalley, A. C., Steigerwald, M. L., Guo, X., and Nuckolls, C.: Reversible Switching in Molecular Electronic Devices. *J Am Chem Soc* 129, 12590–12591 (2007)

[98] Kudernac, T., Katsonis, N., Browne, W. R., and Feringa, B. L.: Nanoelectronic switches: Light-induced switching of the conductance of molecular systems. *J Mater Chem* 19, 7168–7177 (2009)

[99] van der Molen, S. J., Liao, J., Kudernac, T., Agustsson, J. S., Bernard, L., Calame, M., van Wees, B. J., Feringa, B. L., and Schönenberger, C.: Light-Controlled Conductance Switching of Ordered Metal–Molecule–Metal Devices. *Nano Lett* 9, 76–80 (2009)

[100] Green, J. E., Choi, J. W., Boukai, A., Bunimovich, Y., Johnston-Halperin, E., DeIonno, E., Luo, Y., Sheriff, B. A., Xu, K., Shin, Y. S., Tseng, H.-R., Stoddart, J. F., and Heath, J. R.: A 160-kilobit molecular electronic memory patterned at 10^{11} bits per square centimetre. *Nature* 445, 414–417 (2007)

[101] Mathies, R. A., Brito Cruz, C. H., Pollard, W. T., and Shank, C. V.: Direct observation of the femtosecond excited-state cis-trans isomerization in bacteriorhodopsin. *Science* 240, 777–779 (1988)

[102] Palczewski, K., Kumasaka, T., Hori, T., Behnke, C. A., Motoshima, H., Fox, B. A., Trong, I. L., Teller, D. C., Okada, T., Stenkamp, R. E., Yamamoto, M., and Miyano, M.: Crystal Structure of Rhodopsin: A G Protein-Coupled Receptor. *Science* 289, 739–745 (2000)

[103] Gärtner, W.: Das Licht weise den Weg - oder: die Konformationsänderungen des Retinalchromophors im Sehpigment Rhodopsin nach Lichtanregung. *Angew Chem* 113, 3065–3069 (2001)

[104] Mercurio, G., McNellis, E. R., Martin, I., Hagen, S., Leyssner, F., Soubatch, S., Meyer, J., Wolf, M., Tegeder, P., Tautz, F. S., and Reuter, K.: Structure and Energetics of Azobenzene on Ag(111): Benchmarking Semiempirical Dispersion Correction Approaches. *Phys Rev Lett* 104, 036102 (2010)

[105] Liu, W., Filimonov, S. N., Carrasco, J., and Tkatchenko, A.: Molecular switches from benzene derivatives adsorbed on metal surfaces. *Nat Commun* 4, 2569 (2013)

[106] Mercurio, G., Maurer, R. J., Liu, W., Hagen, S., Leyssner, F., Tegeder, P., Meyer, J., Tkatchenko, A., Soubatch, S., Reuter, K., and Tautz, F. S.: Quantification of finite-temperature effects on adsorption geometries of π-conjugated molecules: Azobenzene/Ag(111). *Phys Rev B* 88, 035421 (2013)

[107] Cattaneo, P. and Persico, M.: An *abinitio* study of the photochemistry of azobenzene. *Phys Chem Chem Phys* 1, 4739–4743 (1999)

[108] Schultz, T., Quenneville, J., Levine, B., Toniolo, A., Martínez, T. J., Lochbrunner, S., Schmitt, M., Shaffer, J. P., Zgierski, M. Z., and Stolow, A.: Mechanism and Dynamics of Azobenzene Photoisomerization. *J Am Chem Soc* 125, 8098–8099 (2003)

[109] Füchsel, G., Klamroth, T., Dokić, J., and Saalfrank, P.: On the Electronic Structure of Neutral and Ionic Azobenzenes and Their Possible Role as Surface Mounted Molecular Switches. *J Phys Chem B* 110, 16337–16345 (2006)

[110] Comstock, M. J., Levy, N., Kirakosian, A., Cho, J., Lauterwasser, F., Harvey, J. H., Strubbe, D. A., Fréchet, J. M. J., Trauner, D., Louie,

S. G., and Crommie, M. F.: Reversible Photomechanical Switching of Individual Engineered Molecules at a Metallic Surface. *Phys Rev Lett* 99, 038301 (2007)

[111] Henningsen, N., Franke, K. J., Torrente, I. F., Schulze, G., Priewisch, B., Rück-Braun, K., Dokić, J., Klamroth, T., Saalfrank, P., and Pascual, J. I.: Inducing the Rotation of a Single Phenyl Ring with Tunneling Electrons. *J Phys Chem C* 111, 14843–14848 (2007)

[112] Alemani, M., Selvanathan, S., Ample, F., Peters, M. V., Rieder, K.-H., Moresco, F., Joachim, C., Hecht, S., and Grill, L.: Adsorption and Switching Properties of Azobenzene Derivatives on Different Noble Metal Surfaces: Au(111), Cu(111), and Au(100). *J Phys Chem C* 112, 10509–10514 (2008)

[113] Óvári, L., Schwarz, J., Peters, M. V., Hecht, S., Wolf, M., and Tegeder, P.: Reversible isomerization of an azobenzene derivative adsorbed on Au(1 1 1): Analysis using vibrational spectroscopy. *Int J Mass Spectrom* 277, 223–228 (2008)

[114] Bronner, C., Schulze, G., Franke, K. J., Pascual, J. I., and Tegeder, P.: Switching ability of nitro-spiropyran on Au(111): electronic structure changes as a sensitive probe during a ring-opening reaction. *J Phys: Condens Matter* 23, 484005 (2011)

[115] Bronner, C., Schulze, M., Hagen, S., and Tegeder, P.: The influence of the electronic structure of adsorbate–substrate complexes on photoisomerization ability. *New J Phys* 14, 043023 (2012)

[116] Hagen, S., Leyssner, F., Nandi, D., Wolf, M., and Tegeder, P.: Reversible switching of tetra-*tert*-butyl-azobenzene on a Au(1 1 1) surface induced by light and thermal activation. *Chem Phys Lett* 444, 85–90 (2007)

[117] Bazarnik, M., Henzl, J., Czajka, R., and Morgenstern, K.: Light driven reactions of single physisorbed azobenzenes. *Chem Commun* 47, 7764–7766 (2011)

[118] Schulze, G., Franke, K. J., and Pascual, J. I.: Induction of a Photostationary Ring-Opening–Ring-Closing State of Spiropyran Monolayers on the Semimetallic Bi(110) Surface. *Phys Rev Lett* 109, 026102 (2012)

[119] Pechenezhskiy, I. V., Cho, J., Nguyen, G. D., Berbil-Bautista, L. J., Giles, B. L., Poulsen, D. A., Fréchet, J. M. J., and Crommie, M. F.: Self-Assembly and Photomechanical Switching of an Azobenzene Derivative

on GaAs(110): Scanning Tunneling Microscopy Study. *J Phys Chem C* 116, 1052–1055 (2012)

[120] Maurer, R. J. and Reuter, K.: Bistability Loss as a Key Feature in Azobenzene (Non-)Switching on Metal Surfaces. *Angew Chem Int Ed* 51, 12009 (2012)

[121] Karcher, M., Rüdt, C., Elsäßer, C., and Fumagalli, P.: Switching of nonfunctionalized spiropyran thin films on single crystalline MgO(100). *J Appl Phys* 102, 084904 (2007)

[122] Óvári, L., Luo, Y., Leyssner, F., Haag, R., Wolf, M., and Tegeder, P.: Adsorption and switching properties of a *N*-benzylideneaniline based molecular switch on a Au(111) surface. *J Chem Phys* 133, 044707 (2010)

[123] Frisch, J., Herder, M., Herrmann, P., Heimel, G., Hecht, S., and Koch, N.: Photoinduced reversible changes in the electronic structure of photochromic diarylethene films. *Appl Phys A* 113, 1–4 (2013)

[124] Kobatake, S., Takami, S., Muto, H., Ishikawa, T., and Irie, M.: Rapid and reversible shape changes of molecular crystals on photoirradiation. *Nature* 446, 778–781 (2007)

[125] Koshima, H., Ojima, N., and Uchimoto, H.: Mechanical Motion of Azobenzene Crystals upon Photoirradiation. *J Am Chem Soc* 131, 6890–6891 (2009)

[126] Pace, G., Ferri, V., Grave, C., Elbing, M., von Hänisch, C., Zharnikov, M., Mayor, M., Rampi, M. A., and Samorì, P.: Cooperative light-induced molecular movements of highly ordered azobenzene self-assembled monolayers. *P Natl Acad Sci USA* 104, 9937–9942 (2007)

[127] Wagner, S., Leyssner, F., Kördel, C., Zarwell, S., Schmidt, R., Weinelt, M., Rück-Braun, K., Wolf, M., and Tegeder, P.: Reversible photoisomerization of an azobenzene-functionalized self-assembled monolayer probed by sum-frequency generation vibrational spectroscopy. *Phys Chem Chem Phys* 11, 6242–6248 (2009)

[128] Gahl, C., Schmidt, R., Brete, D., McNellis, E. R., Freyer, W., Carley, R., Reuter, K., and Weinelt, M.: Structure and Excitonic Coupling in Self-Assembled Monolayers of Azobenzene-Functionalized Alkanethiols. *J Am Chem Soc* 132, 1831–1838 (2010)

[129] de Villeneuve, C. H., Michalik, F., Chazalviel, J. N., Rück-Braun, K., and Allongue, P.: Quantitative IR Readout of Fulgimide Monolayer Switching on Si(111) Surfaces. *Adv Mater* 25, 416–421 (2013)

[130] Safiei, A., Henzl, J., and Morgenstern, K.: Isomerization of an Azobenzene Derivative on a Thin Insulating Layer by Inelastically Tunneling Electrons. *Phys Rev Lett* 104, 216102 (2010)

[131] Mohn, F., Repp, J., Gross, L., Meyer, G., Dyer, M. S., and Persson, M.: Reversible Bond Formation in a Gold-Atom–Organic-Molecule Complex as a Molecular Switch. *Phys Rev Lett* 105, 266102 (2010)

[132] Henzl, J., Puschnig, P., Ambrosch-Draxl, C., Schaate, A., Ufer, B., Behrens, P., and Morgenstern, K.: Photoisomerization for a molecular switch in contact with a surface. *Phys Rev B* 85, 035410 (2012)

[133] Jung, T. A., Schlittler, R. R., and Gimzewski, J. K.: Conformational identification of individual adsorbed molecules with the STM. *Nature* 386, 696–698 (1997)

[134] Moresco, F., Meyer, G., Rieder, K.-H., Tang, H., Gourdon, A., and Joachim, C.: Conformational Changes of Single Molecules Induced by Scanning Tunneling Microscopy Manipulation: A Route to Molecular Switching. *Phys Rev Lett* 86, 672 (2001)

[135] Kuntze, J., Berndt, R., Jiang, P., Tang, H., Gourdon, A., and Joachim, C.: Conformations of a molecular wire adsorbed on a metal surface. *Phys Rev B* 65, 233405 (2002)

[136] McNellis, E. R., Mercurio, G., Hagen, S., Leyssner, F., Meyer, J., Soubatch, S., Wolf, M., Reuter, K., Tegeder, P., and Tautz, F. S.: Bulky spacer groups – A valid strategy to control the coupling of functional molecules to surfaces? *Chem Phys Lett* 499, 247–249 (2010)

[137] McNellis, E. R., Bronner, C., Meyer, J., Weinelt, M., Tegeder, P., and Reuter, K.: Azobenzene *versus* 3,3',5,5'-tetra-*tert*-butyl-azobenzene (TBA) at Au(111): characterizing the role of spacer groups. *Phys Chem Chem Phys* 12, 6404–6412 (2010)

[138] Zhou, X. L., Zhu, X. Y., and White, J. M.: Photodissociation of intraadsorbate bonds at adsorbate-metal interfaces. *Acc Chem Res* 23, 327–332 (1990)

[139] Hagen, S., Kate, P., Leyssner, F., Nandi, D., Wolf, M., and Tegeder, P.: Excitation mechanism in the photoisomerization of a surface-bound azobenzene derivative: Role of the metallic substrate. *J Chem Phys* 129, 164102 (2008)

[140] Mukherjee, S., Libisch, F., Large, N., Neumann, O., Brown, L. V., Cheng, J., Lassiter, J. B., Carter, E. A., Nordlander, P., and Halas, N. J.: Hot Electrons Do the Impossible: Plasmon-Induced Dissociation of H_2 on Au. *Nano Lett* 13, 240–247 (2013)

[141] Tegeder, P.: Optically and thermally induced molecular switching processes at metal surfaces. *J Phys: Condens Matter* 24, 394001 (2012)

[142] Fauster, T.: Two-photon photoemission. *Prog Surf Sci* 46, 177–186 (1994)

[143] Petek, H. and Ogawa, S.: Femtosecond time-resolved two-photon photoemission studies of electron dynamics in metals. *Prog Surf Sci* 56, 239–310 (1997)

[144] Weinelt, M.: Time-resolved two-photon photoemission from metal surfaces. *J Phys: Condens Matter* 14, R1099 (2002)

[145] Zhu, X.-Y.: Electronic structure and electron dynamics at molecule–metal interfaces: implications for molecule-based electronics. *Surf Sci Rep* 56, 1–83 (2004)

[146] Güdde, J., Berthold, W., and Höfer, U.: Dynamics of Electronic Transfer Processes at Metal/Insulator Interfaces. *Chem Rev* 106, 4261–4280 (2006)

[147] Hagen, S.: *Isomerization behavior of photochromic molecules in direct contact with noble metal surfaces.* Ph.D. thesis, Freie Universität Berlin (2009)

[148] Gahl, C.: *Elektronentransfer- und Solvatisierungsdynamik in Eis adsorbiert auf Metalloberflächen.* Ph.D. thesis, Freie Universität Berlin (2004)

[149] Stähler, A. J.: *Freezing Hot Electrons: Electron Transfer Dynamics at* D_2O *and* NH_3*–Metal Interfaces.* Ph.D. thesis, Freie Universität Berlin (2007)

[150] Kirchmann, P. S.: *Ultrafast Electron Dynamics in Low-Dimensional Materials.* Ph.D. thesis, Freie Universität Berlin (2008)

[151] Fork, R. L., Martinez, O. E., and Gordon, J. P.: Negative dispersion using pairs of prisms. *Opt Lett* 9, 150–152 (1984)

[152] Talirz, L., Söde, H., Cai, J., Ruffieux, P., Blankenburg, S., Jafaar, R., Berger, R., Feng, X., Müllen, K., Passerone, D., Fasel, R., and Pignedoli, C. A.: Termini of Bottom-Up Fabricated Graphene Nanoribbons. *J Am Chem Soc* 135, 2060–2063 (2013)

[153] van der Lit, J., Boneschanscher, M. P., Vanmaekelbergh, D., Ijäs, M., Uppstu, A., Ervasti, M., Harju, A., Liljeroth, P., and Swart, I.: Suppression of electron–vibron coupling in graphene nanoribbons contacted via a single atom. *Nat Commun* 4, 2023 (2013)

[154] Martins, T. B., Miwa, R. H., da Silva, A. J. R., and Fazzio, A.: Electronic and Transport Properties of Boron-Doped Graphene Nanoribbons. *Phys Rev Lett* 98, 196803 (2007)

[155] Biel, B., Blase, X., Triozon, F., and Roche, S.: Anomalous Doping Effects on Charge Transport in Graphene Nanoribbons. *Phys Rev Lett* 102, 096803 (2009)

[156] Lherbier, A., Blase, X., Niquet, Y.-M., Triozon, F., and Roche, S.: Charge Transport in Chemically Doped 2D Graphene. *Phys Rev Lett* 101, 036808 (2008)

[157] Narita, A., Feng, X., Hernandez, Y., Jensen, S. A., Bonn, M., Yang, H., Verzhbitskiy, I. A., Casiraghi, C., Hansen, M. R., Koch, A. H. R., Fytas, G., Ivasenko, O., Li, B., Mali, K. S., Balandina, T., Mahesh, S., De Feyter, S., and Müllen, K.: Synthesis of structurally well-defined and liquid-phase-processable graphene nanoribbons. *Nat Chem* 6, 126–132 (2014)

[158] Björk, J., Hanke, F., and Stafström, S.: Mechanisms of Halogen-Based Covalent Self-Assembly on Metal Surfaces. *J Am Chem Soc* 135, 5768–5775 (2013)

[159] Treier, M., Pignedoli, C. A., Laino, T., Rieger, R., Müllen, K., Passerone, D., and Fasel, R.: Surface-assisted cyclodehydrogenation provides a synthetic route towards easily processable and chemically tailored nanographenes. *Nat Chem* 3, 61–67 (2011)

[160] Linden, S., Zhong, D., Timmer, A., Aghdassi, N., Franke, J. H., Zhang, H., Feng, X., Müllen, K., Fuchs, H., Chi, L., and Zacharias, H.: Electronic Structure of Spatially Aligned Graphene Nanoribbons on Au(788). *Phys Rev Lett* 108, 216801 (2012)

[161] Björk, J., Stafström, S., and Hanke, F.: Zipping Up: Cooperativity Drives the Synthesis of Graphene Nanoribbons. *J Am Chem Soc* 133, 14884–14887 (2011)

[162] Blankenburg, S., Cai, J., Ruffieux, P., Jaafar, R., Passerone, D., Feng, X., Müllen, K., Fasel, R., and Pignedoli, C. A.: Intraribbon Heterojunction Formation in Ultranarrow Graphene Nanoribbons. *ACS Nano* 6, 2020–2025 (2012)

[163] Ruffieux, P., Cai, J., Plumb, N. C., Patthey, L., Prezzi, D., Ferretti, A., Molinari, E., Feng, X., Müllen, K., Pignedoli, C. A., and Fasel, R.: Electronic Structure of Atomically Precise Graphene Nanoribbons. *ACS Nano* 6, 6930–6935 (2012)

[164] Liang, L. and Meunier, V.: Electronic structure of assembled graphene nanoribbons: Substrate and many-body effects. *Phys Rev B* 86, 195404 (2012)

[165] Costa Girão, E., Liang, L., Cruz-Silva, E., Gomes Souza Filho, A., and Meunier, V.: Emergence of Atypical Properties in Assembled Graphene Nanoribbons. *Phys Rev Lett* 107, 135501 (2011)

[166] Hagen, S., Luo, Y., Haag, R., Wolf, M., and Tegeder, P.: Electronic structure and electron dynamics at an organic molecule/metal interface: interface states of tetra-*tert*-butyl-imine/Au(111). *New J Phys* 12, 125022 (2010)

[167] Berthold, W., Höfer, U., Feulner, P., and Menzel, D.: Influence of Xe adlayer morphology and electronic structure on image-potential state lifetimes of Ru(0001). *Chem Phys* 251, 123–132 (2000)

[168] Lindstrom, C. D., Quinn, D., and Zhu, X.-Y.: Using image resonances to probe molecular conduction at the *n*-heptane/Au(111) interface. *J Chem Phys* 122, 124714 (2005)

[169] Hotzel, A.: Electron dynamics of image potential states in weakly bound adsorbate layers: A short review. *Prog Surf Sci* 82, 336–354 (2007)

[170] Strader, M. L., Garrett-Roe, S., Szymanski, P., Shipman, S. T., Johns, J. E., Yang, A., Muller, E., and Harris, C. B.: The Ultrafast Dynamics of Image Potential State Electrons at the Dimethylsulfoxide/Ag(111) Interface. *J Phys Chem C* 112, 6880–6886 (2008)

[171] Nobis, D., Potenz, M., Niesner, D., and Fauster, T.: Image-potential states of graphene on noble-metal surfaces. *Phys Rev B* 88, 195435 (2013)

[172] Bronner, C., Priewisch, B., Rück-Braun, K., and Tegeder, P.: Photoisomerization of an Azobenzene on the Bi(111) Surface. *J Phys Chem C* 117, 27031–27038 (2013)

[173] Chen, B.: *in preparation.* Ph.D. thesis, Freie Universität Berlin

[174] Bronner, C., Chen, B., Ahmadi, G., Heinrich, B. W., Franke, K. J., and Tegeder, P.: Photoinduced covalent coupling of surface-bound molecular building blocks. *in preparation*

[175] Tegeder, P., Hagen, S., Leyssner, F., Peters, M. V., Hecht, S., Klamroth, T., Saalfrank, P., and Wolf, M.: Electronic structure of the molecular switch tetra-*tert*-butyl-azobenzene adsorbed on Ag(111). *Appl Phys A* 88, 465–472 (2007)

[176] Xi, M., Yang, M. X., Jo, S. K., Bent, B. E., and Stevens, P.: Benzene adsorption on Cu(111): Formation of a stable bilayer. *J Chem Phys* 101, 9122 (1994)

[177] Wu, M. C., Truong, C. M., and Goodman, D. W.: Interactions of ammonia with a nickel oxide (100) surface studied by high-resolution electron energy loss spectroscopy and temperature programmed desorption spectroscopy. *J Phys Chem* 97, 4182–4186 (1993)

[178] Zou, Y., Kilian, L., Schöll, A., Schmidt, T., Fink, R., and Umbach, E.: Chemical bonding of PTCDA on Ag surfaces and the formation of interface states. *Surf Sci* 600, 1240–1251 (2006)

[179] Cheng, C. C., Lucas, S. R., Gutleben, H., Choyke, W. J., and Yates, J. T., Jr.: Atomic hydrogen-driven halogen extraction from silicon(100): Eley-Rideal surface kinetics. *J Am Chem Soc* 114, 1249–1252 (1992)

[180] Cohen, S. M., Hukka, T. I., Yang, Y. L., and D'Evelyn, M. P.: Hydrogen-halogen chemistry on semiconductor surfaces. *Thin Solid Films* 225, 155–159 (1993)

[181] McEllistrem, M., Buehler, E. J., Itchkawitz, B. S., and Boland, J. J.: Abstraction of chemisorbed bromine from the Si(111) surface by incident hydrogen atoms. *J Chem Phys* 108, 7384 (1998)

[182] Szulczewski, G. J. and White, J. M.: Thermal and photon-stimulated reactions of iodobenzene on Ag(111). *Surf Sci* 399, 305–315 (1998)

[183] Zhou, X.-L. and White, J. M.: Photon- and electron-induced chemistry of chlorobenzene on Ag(111). *J Chem Phys* 92, 5612 (1990)

[184] Sault, A. G., Madix, R. J., and Campbell, C. T.: Adsorption of oxygen and hydrogen on Au(110)-(1 × 2). *Surf Sci* 169, 347–356 (1986)

[185] Okada, M., Nakamura, M., Moritani, K., and Kasai, T.: Dissociative adsorption of hydrogen on thin Au films grown on Ir{111}. *Surf Sci* 523, 218–230 (2003)

[186] Ferrin, P., Kandoi, S., Nilekar, A. U., and Mavrikakis, M.: Hydrogen adsorption, absorption and diffusion on and in transition metal surfaces: A DFT study. *Surf Sci* 606, 679–689 (2012)

[187] Lee, J. Y., Maeng, J. Y., Kim, A., Cho, Y. E., and Kim, S.: Kinetics of H_2 (D_2) desorption from a Ge(100)-2×1:H (D) surface studied using scanning tunneling microscopy and temperature programmed desorption. *J Chem Phys* 118, 1929 (2003)

[188] Bronner, C., Utecht, M., Haase, A., Saalfrank, P., Klamroth, T., and Tegeder, P.: Electronic structure changes during the surface-assisted formation of a graphene nanoribbon. *J Chem Phys* 140, 024701 (2014)

[189] Leyssner, F.: *Analysis of Functional Organic Molecules at Noble Metal Surfaces by Means of Vibrational Spectroscopies.* Ph.D. thesis, Freie Universität Berlin (2011)

[190] Stremlau, S.: *in preparation.* Ph.D. thesis, Freie Universität Berlin

[191] Bronner, C., Leyssner, F., Stremlau, S., Utecht, M., Saalfrank, P., Klamroth, T., and Tegeder, P.: Electronic structure of a subnanometer wide bottom-up fabricated graphene nanoribbon: End states, band gap, and dispersion. *Phys Rev B* 86, 085444 (2012)

[192] Utecht, M.: *in preparation.* Ph.D. thesis, Universität Potsdam

[193] Adamo, C. and Barone, V.: Toward reliable density functional methods without adjustable parameters: The PBE0 model. *J Chem Phys* 110, 6158 (1999)

[194] Yanai, T., Tew, D. P., and Handy, N. C.: A new hybrid exchange–correlation functional using the Coulomb-attenuating method (CAM-B3LYP). *Chem Phys Lett* 393, 51–57 (2004)

[195] Wang, G.: Density functional study on the increment of carrier mobility in armchair graphene nanoribbons induced by Stone–Wales defects. *Phys Chem Chem Phys* 13, 11939–11945 (2011)

[196] Fauster, T., Reuß, C., Shumay, I. L., and Weinelt, M.: Femtosecond two-photon photoemission studies of image-potential states. *Chem Phys* 251, 111–121 (2000)

[197] Dose, V., Altmann, W., Goldmann, A., Kolac, U., and Rogozik, J.: Image-Potential States Observed by Inverse Photoemission. *Phys Rev Lett* 52, 1919 (1984)

[198] Rohleder, M., Duncker, K., Berthold, W., Güdde, J., and Höfer, U.: Momentum-resolved dynamics of Ar/Cu(1 0 0) interface states probed by time-resolved two-photon photoemission. *New J Phys* 7, 103 (2005)

[199] Rohleder, M., Berthold, W., Güdde, J., and Höfer, U.: Time-Resolved Two-Photon Photoemission of Buried Interface States in Ar/Cu(100). *Phys Rev Lett* 94, 017401 (2005)

[200] Muntwiler, M., Lindstrom, C. D., and Zhu, X.-Y.: Delocalized electron resonance at the alkanethiolate self-assembled monolayer/Au(111) interface. *J Chem Phys* 124, 081104 (2006)

[201] Palmberg, P. W.: Physical adsorption of xenon on Pd(100). *Surf Sci* 25, 598–608 (1971)

[202] Nieuwenhuys, B. E., Bouwman, R., and Sachtler, W. M. H.: The changes in work function of group Ib and VIII metals on xenon adsorption, determined by field electron and photoelectron emission. *Thin Solid Films* 21, 51–58 (1974)

[203] Wolf, M., Knoesel, E., and Hertel, T.: Ultrafast dynamics of electrons in image-potential states on clean and Xe-covered Cu(111). *Phys Rev B* 54, R5295 (1996)

[204] Koch, M.: *Growth and Characterization of Single Molecular Wires on Metal Surfaces.* Ph.D. thesis, Freie Universität Berlin (2013)

[205] Zhou, X.-L., Zhu, X.-Y., and White, J. M.: Photochemistry at adsorbate/metal interfaces. *Surf Sci Rep* 13, 73–220 (1991)

[206] Hasselbrink, E.: Mechanisms in photochemistry on metal surfaces. *Appl Surf Sci* 79, 34–40 (1994)

[207] Bald, I., Langer, J., Tegeder, P., and Ingólfsson, O.: From isolated molecules through clusters and condensates to the building blocks of life. *Int J Mass Spectrom* 277, 4–25 (2008)

[208] Hla, S.-W., Bartels, L., Meyer, G., and Rieder, K.-H.: Inducing All Steps of a Chemical Reaction with the Scanning Tunneling Microscope Tip: Towards Single Molecule Engineering. *Phys Rev Lett* 85, 2777 (2000)

[209] Bronner, C., Stremlau, S., Gille, M., Brauße, F., Haase, A., Hecht, S., and Tegeder, P.: Aligning the Band Gap of Graphene Nanoribbons by Monomer Doping. *Angew Chem Int Ed* 52, 4422–4425 (2013)

[210] Gille, M.: *Graphen und Graphenstreifen Bottom-up: Chemische Syntheseansätze für defektfreies und gezielt modifiziertes ein- und zweidimensionales Graphen.* Ph.D. thesis, Humboldt-Universität zu Berlin (2012)

[211] Monti, S., Orlandi, G., and Palmieri, P.: Features of the photochemically active state surfaces of azobenzene. *Chem Phys* 71, 87–99 (1982)

[212] Tamai, N. and Miyasaka, H.: Ultrafast Dynamics of Photochromic Systems. *Chem Rev* 100, 1875–1890 (2000)

[213] Cembran, A., Bernardi, F., Garavelli, M., Gagliardi, L., and Orlandi, G.: On the Mechanism of the cis–trans Isomerization in the Lowest Electronic States of Azobenzene: S_0, S_1, and T_1. *J Am Chem Soc* 126, 3234–3243 (2004)

[214] Hartley, G. S.: The *Cis*-form of Azobenzene. *Nature* 140, 281 (1937)

[215] Talaty, E. R. and Fargo, J. C.: Thermal *cis–trans*-Isomerization of Substituted Azobenzenes: a Correction of the Literature. *Chem Commun* 65 (1967)

[216] Brown, E. V. and Granneman, G. R.: Cis-trans isomerism in the pyridyl analogs of azobenzene. Kinetic and molecular orbital analysis. *J Am Chem Soc* 97, 621–627 (1975)

[217] Andersson, J.-Å., Petterson, R., and Tegnér, L.: Flash photolysis experiments in the vapour phase at elevated temperatures I: spectra of azobenzene and the kinetics of its thermal *cis-trans* isomerization. *J Photochem* 20, 17–32 (1982)

[218] Schulze, F.-W., Petrick, H.-J., Cammenga, H. K., and Klinge, H.: Thermodynamic Properties of the Structural Analogues Benzo[c]cinnoline, Trans-azobenzene, and Cis-azobenzene. *Zeitschrift für Physikalische Chemie* 107, 1–19 (1977)

[219] Bortolus, P. and Monti, S.: Cis-Trans Photoisomerization of Azobenzene. Solvent and Triplet Donor Effects. *J Phys Chem* 83, 648–652 (1979)

[220] Zimmerman, G., Chow, L.-Y., and Paik, U.-J.: The Photochemical Isomerization of Azobenzene. *J Am Chem Soc* 80, 3528–3531 (1958)

[221] Henningsen, N., Rurali, R., Franke, K. J., Fernández-Torrente, I., and Pascual, J. I.: *Trans* to *cis* isomerization of an azobenzene derivative on a Cu(100) surface. *Appl Phys A* 93, 241–246 (2008)

[222] Henningsen, N., Rurali, R., Limbach, C., Drost, R., Pascual, J. I., and Franke, K. J.: Site-Dependent Coordination Bonding in Self-Assembled Metal–Organic Networks. *J Phys Chem Lett* 2, 55–61 (2011)

[223] Bronner, C. and Tegeder, P.: Unoccupied electronic band structure of the semi-metallic Bi(111) surface probed with two-photon photoemission. *Phys Rev B* 87, 035123 (2013)

[224] Bronner, C. and Tegeder, P.: Relaxation Dynamics of Photo-Excited Charge Carriers at the Bi(111) Surface. *Phys Rev B* in press (2014)

[225] Celii, F. G., Whitmore, P. M., and Janda, K. C.: UV Laser-Induced Photochemistry of $Fe(CO)_5$ on Single Crystal Surfaces in Ultrahigh Vacuum. *J Phys Chem* 92, 1604–1612 (1988)

[226] Grassian, V. H. and Pimentel, G. C.: Photochemical reactions of *cis*- and *trans*-1,2-dichloroethene adsorbed on Pd(111) and Pt(111). *J Chem Phys* 88, 4484 (1988)

[227] Mödl, A., Domen, K., and Chuang, T. J.: Laser-induced CH_2 and C_2H_4 formation and desorption from CH_2I_2 adsorbed on Al surfaces. *Chem Phys Lett* 154, 187–192 (1989)

[228] Domen, K. and Chuang, T. J.: Laser induced photodissociation and desorption. II. CH_2I_2 adsorbed on Ag. *J Chem Phys* 90, 3332 (1989)

[229] Knoesel, E., Hotzel, A., Hertel, T., Wolf, M., and Ertl, G.: Dynamics of photoexcited electrons in metals studied with time-resolved two-photon photoemission. *Surf Sci* 368, 76–81 (1996)

[230] Aeschlimann, M., Bauer, M., and Pawlik, S.: Competing nonradiative channels for hot electron induced surface photochemistry. *Chem Phys* 205, 127–141 (1996)

[231] Ogawa, S., Nagano, H., and Petek, H.: Hot-electron dynamics at Cu(100), Cu(110), and Cu(111) surfaces: Comparison of experiment with Fermi-liquid theory. *Phys Rev B* 55, 10869 (1997)

[232] Marsh, E. P., Gilton, T. L., Meier, W., Schneider, M. R., and Cowin, J. P.: Electron-transfermediated and direct surface photochemistry: CH_3Cl on Ni(111). *Phys Rev Lett* 61, 2725 (1988)

[233] Cho, C. C., Collings, B. A., Hammer, R. E., Polanyi, J. C., Stanners, C. D., Wang, J. H., and Xu, G. Q.: Photoinduced charge-transfer dissociation of hydrogen chloride on silver(111). *J Phys Chem* 93, 7761–7762 (1989)

[234] Wolf, M., Hasselbrink, E., Ertl, G., Zhu, X.-Y., and White, J. M.: Excitation mechanism in the photodissociation of dioxygen adsorbed on Pd(111). *Surf Sci Lett* 248, L235–L239 (1991)

[235] Thompson, T. L. and Yates, J. T., Jr.: Surface Science Studies of the Photoactivation of TiO_2—New Photochemical Processes. *Chem Rev* 106, 4428–4453 (2006)

[236] Lindstrom, C. D. and Zhu, X.-Y.: Photoinduced Electron Transfer at Molecule–Metal Interfaces. *Chem Rev* 106, 4281–4300 (2006)

[237] Priewisch, B.: *Photoschaltbare Aminosäuren: Synthese, photochrome Eigenschaften und Einbau in peptidische Grb2-SH2 Antagonisten.* Ph.D. thesis, Technische Universität Berlin (2006)

[238] Muntwiler, M. and Zhu, X.-Y.: Image-potential states on the metallic (111) surface of bismuth. *New J Phys* 10, 113018 (2008)

[239] Mazalova, V., Soldatov, A., Krüger, A., and Kuch, W.: Theoretical study of the local atomic and electronic structure of dimetacyano azobenzene molecules on Bi (111) substrate. *J Phys: Conf Ser* 430, 012036 (2013)

[240] Comstock, M. J., Levy, N., Cho, J., Berbil-Bautista, L., Crommie, M. F., Poulsen, D. A., and Fréchet, J. M. J.: Measuring reversible photomechanical switching rates for a molecule at a surface. *Appl Phys Lett* 92, 123107 (2008)

[241] Wolf, M. and Tegeder, P.: Reversible molecular switching at a metal surface: A case study of tetra-*tert*-butyl-azobenzene on Au(1 1 1). *Surf Sci* 603, 1506–1517 (2009)

[242] Palmberg, P. W.: *Handbook of Auger Electron Spectroscopy.* Physics Electronics Industries (1972)

[243] Lüth, H.: *Surfaces and Interfaces of Solid Materials.* Springer, 3 edn. (1995)

[244] Wegkamp, D., Meyer, M., Richter, C., Wolf, M., and Stähler, J.: Photoinduced work function modifications and their effect on photoelectron spectroscopy. *Appl Phys Lett* 103, 151603 (2013)

[245] Hagen, S., Kate, P., Peters, M. V., Hecht, S., Wolf, M., and Tegeder, P.: Kinetic analysis of the photochemically and thermally induced isomerization of an azobenzene derivative on Au(111) probed by two-photon photoemission. *Appl Phys A* 93, 253–260 (2008)

[246] Mielke, J., Leyssner, F., Koch, M., Meyer, S., Luo, Y., Selvanathan, S., Haag, R., Tegeder, P., and Grill, L.: Imine Derivatives on Au(111): Evidence for "Inverted Thermal Isomerization. *ACS Nano* 5, 2090–2097 (2011)

[247] Weigelt, S., Busse, C., Petersen, L., Rauls, E., Hammer, B., Gothelf, K. V., Besenbacher, F., and Linderoth, T. R.: Chiral switching by spontaneous conformational change in adsorbed organic molecules. *Nat Mater* 5, 112–117 (2006)